Chapter 10

An Improved Optical Tweezers Assay for Measuring the Force Generation of Single Kinesin Molecules

Matthew P. Nicholas, Lu Rao, and Arne Gennerich

Abstract

Numerous microtubule-associated molecular motors, including several kinesins and cytoplasmic dynein, produce opposing forces that regulate spindle and chromosome positioning during mitosis. The motility and force generation of these motors are therefore critical to normal cell division, and dysfunction of these processes may contribute to human disease. Optical tweezers provide a powerful method for studying the nanometer motility and piconewton force generation of single motor proteins in vitro. Using kinesin-1 as a prototype, we present a set of step-by-step, optimized protocols for expressing a kinesin construct (K560-GFP) in *Escherichia coli*, purifying it, and studying its force generation in an optical tweezers microscope. We also provide detailed instructions on proper alignment and calibration of an optical trapping microscope. These methods provide a foundation for a variety of similar experiments.

Key words Optical tweezers, Optical trapping, Optical trap alignment and calibration, Molecular motors, Kinesin, K560, Microtubules, Pyranose oxidase, Single-molecule assays, Force measurement, *Escherichia coli*, Protein purification

1 Introduction

Cytoskeletal filaments and their associated molecular motor proteins generate a multitude of forces that orchestrate the complex process of mitosis. While actin and myosin II drive the actual division of cells (the separation of the cytoplasm of the original cell into two new cells), it is primarily microtubules (MTs) and their associated motor proteins, cytoplasmic dynein and kinesins (composed of several distinct subfamilies) [1, 2], that govern the intricate rearrangements of the mitotic spindle preceding cytokinesis [3].

Numerous MT-associated motors exert forces on the MT mitotic spindle [4–8]. For example, during anaphase B, cytoplasmic dynein attached to the cell cortex walks toward the minus ends of astral MTs, pulling the spindle poles away from each other and toward the cell periphery [9]. The tetrameric, bipolar kinesin-5 (also called Eg5 or Kif11) likewise drives the spindle poles apart by

David J. Sharp (ed.), *Mitosis: Methods and Protocols*, Methods in Molecular Biology, vol. 1136,
DOI 10.1007/978-1-4939-0329-0_10,

simultaneously moving toward the plus ends of antiparallel interpolar MTs in the spindle midzone [10] (thereby sliding the oppositely oriented MTs away from one another). Interestingly, however, dynein appears to antagonize the function of kinesin-5 [11–13]. Kinesin-14 family proteins (e.g., HSET, Ncd)—which are homodimeric/unipolar, but nonetheless cross-link and slide antiparallel MTs—oppose the forces produced by kinesin-5 [14–17]. The kinesin-14 motor domain is near the C-terminus, and this motor walks in the opposite direction of most of its N-terminal kinesin relatives [1, 18, 19]. Thus, it pulls oppositely oriented MTs at the spindle midzone closer together as it walks toward the MT minus end.

During all of these processes, the MTs themselves are highly dynamic, regulated in part by members of the microtubule-destabilizing kinesin-13 family [20–22]. In addition, separate motors exert forces directly on chromosomes. The plus-end-directed kinesin-4 and kinesin-10 (the so-called chromokinesins) attach to chromosomes and carry them away from the spindle poles [1].

Despite growing knowledge, we are only beginning to understand how forces in mitosis are generated and regulated. As discussed, numerous different molecules are involved. In vitro single-molecule studies have proved useful in deciphering the functions of the various constituent proteins in isolation [13, 16, 23–25]. Among these techniques, optical trapping (also called optical tweezers; *see* refs. 26, 27 for excellent reviews) is particularly informative, because it can measure and exert forces on the piconewton (pN)-scale characteristic of molecular motors [28–32].

The basis for conventional optical trapping is the transfer of momentum from photons in a focused laser beam to a small dielectric particle. In the simple ray-optics picture (*see* **Note 1** for a more complete description), this occurs due to refraction of light by a microsphere ("bead") placed in a highly focused, near-infrared laser beam with a Gaussian intensity profile [26]. Refracted photons experience a change in momentum—i.e., a force—associated with their altered direction of propagation. Due to momentum conservation (or, alternatively, Newton's third law), the microsphere experiences an equal and opposite change in momentum (force) in the opposite direction as that experienced by the refracted photons. Near the laser focus, the geometry of the system (namely, the gradient of laser intensity surrounding the focus) causes the net force on the microsphere to pull it toward the center of the focus ("trap center") whenever it is displaced, thus "trapping" the particle in three dimensions. Conveniently, for small displacements, the microsphere position can be tracked with extremely high precision (a few nanometers or better), and the force exerted on it is linear with this displacement [26]. This is analogous to the force $F = -k\Delta x$ predicted by Hooke's law for an ideal spring extended a distance Δx, where the constant k is referred to as the

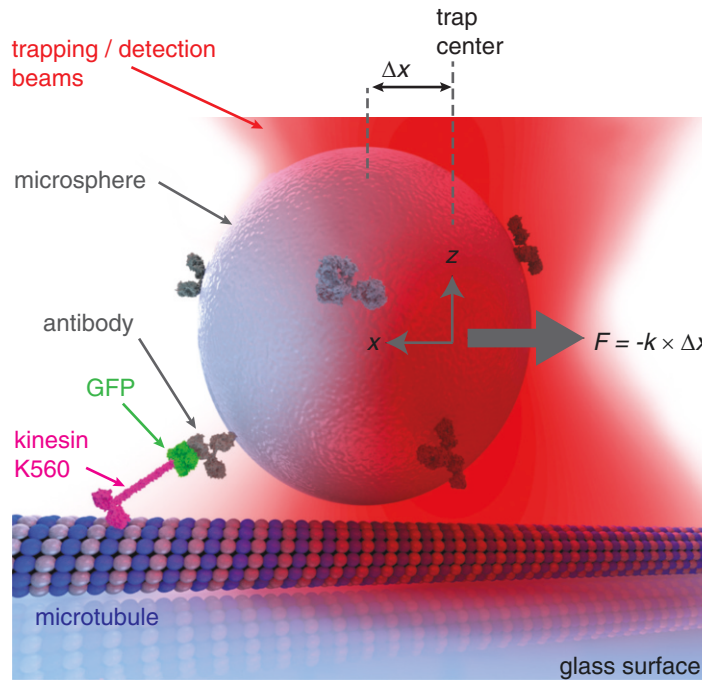

Fig. 1 Optical tweezers assay for kinesin motility and force production (not to scale). A polystyrene microsphere covalently bound to anti-GFP antibodies binds a single kinesin K560-GFP dimer, and is trapped by a near-infrared optical trapping beam focused via a high numerical aperture microscope objective lens. The trap holds the microsphere directly above a MT that is covalently linked to the glass surface of the cover slip. When the kinesin binds to and moves along the MT in the presence of ATP, it pulls the attached microsphere with it. The trap resists this motion, exerting a force $F = -k \times \Delta x$ on the microsphere-motor complex, where k is the trap stiffness (force per displacement) and Δx is the distance from the trapping beam longitudinal (z) axis ("trap center") to the center of the microsphere. The detection beam—which overlaps the trapping beam, but does not contribute to trapping—is used to measure Δx via back focal plane interferometry. This figure was prepared with VMD [164] (using PDB entries 3KIN, 1GFL, and 1IGT) and the Persistence of Vision Raytracer (POV-Ray www.povray.org)

"spring constant" or "stiffness" (for optical traps, k is directly proportional to the laser intensity, but also depends on the diameter of the microsphere [33–35]). Therefore, by linking motor proteins to optically trapped microspheres, one can measure both the motility and force produced by these mechanoenzymes as they move along their cytoskeletal filaments and thereby displace the trapped bead from the trap center (Fig. 1). In fact, even some endogenous biological particles (e.g., endosomes) can be optically trapped, so that the technique can be applied in vivo [36–38] (though calibration and interpretation of results are more complicated).

Although optical trapping is still mainly a tool of specialists, its popularity and application have grown significantly since its first application to motor proteins [39], and it is feasible for nonexperts to build and use simple optical tweezers microscopes in their laboratories (some commercial options are also available [40]). While establishing microsphere trapping is relatively straightforward, accurately and precisely calibrating the instrument for force measurement presents some challenges. Although there is rich literature on technical aspects of optical trapping (*see*, e.g., [26, 27] and references therein), our own experience with building and calibrating such an instrument convinced us of the importance of a comprehensive, up-to-date resource addressing the many "hands-on" details and subtleties involved. Our goal is to help bridge the gap between "qualitative" optical trapping and research-quality force measurements.

In addition to details on instrumentation, we provide a simple system using optimized biochemical conditions, with which to establish a basic optical tweezers assay. Not long after its discovery over 25 years ago [41], kinesin-1 (also known as conventional kinesin) was the first molecular motor studied by optical trapping [39], and it has since become perhaps the best-studied MT-associated motor. As such, it serves as a well-characterized, predictable standard for establishing optical tweezers assays that measure the dynamic behavior of molecular motors. Here, we provide methods for isolating recombinant kinesin-1 and studying its motility and force production in vitro as it walks processively toward the plus ends of MTs. These optimized protocols provide a basis for a host of similar experiments.

Below, we describe the recombinant expression in *Escherichia coli* (*E. coli*) of a GFP- and polyhistidine-tagged construct (herein referred to as K560-GFP, or simply K560) containing the first 560 amino acids of human kinesin-1 [42] (*see* **Note 2**). We then provide methods for isolating functional kinesin motors to high purity by sequential steps of cell lysis, centrifugation, nickel-nitrilotriacetic acid (Ni-NTA), agarose affinity column purification (via the K560 polyhistidine-tag), and MT pulldown with ATP-induced release. These procedures yield functional K560 protein sufficient for a number of single-molecule experiments, including optical tweezers assays.

Next, we describe how to measure the movement and force generation of single K560 molecules as they walk along MTs in vitro. This includes methods for (1) preparing optical trapping beads (polystyrene microspheres) with covalently bound anti-GFP antibodies (*see* **Note 3**), (2) attaching K560-GFP to these beads, and (3) measuring K560 motility and force production as it pulls against the opposing load applied by an optical tweezers. We provide the pertinent details of the design and calibration of a combined optical trapping and total internal reflection fluorescence (TIRF) microscope capable of measuring nanometer- and

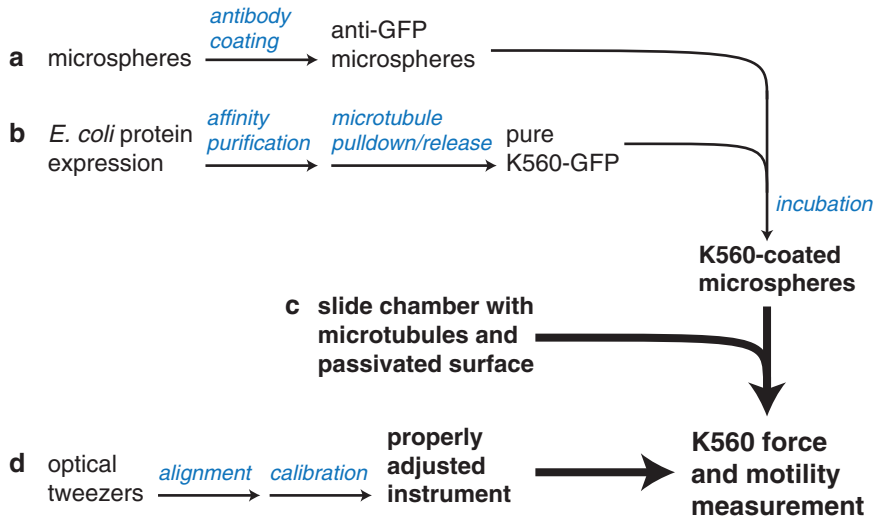

Fig. 2 Protocol summary. Each pathway (**a**–**d**) summarizes the major steps in preparing reagents and instrumentation for the final assay: (**a**, **b**) purifying kinesin and attaching it to optical trapping microspheres bound to antibodies; (**c**) preparation of a slide chamber with immobilized, Cy3-labeled MTs (*see* Chap. 9, this issue); (**d**) aligning and calibrating the optical tweezers instrument. These tools are combined to precisely measure force production and motility of single kinesin molecules

piconewton-scale displacements and forces. Figure 2 summarizes how the various procedures come together to enable measurements of force production by single kinesins.

In addition to the procedures and accompanying figures, we have made extensive use of notes to draw attention to important details and underlying principles. The reader is encouraged to consult this section thoroughly before performing the protocols. We also wish to direct the reader to our accompanying protocol for slide chamber preparation and MT fluorescence labeling, polymerization, and surface immobilization (*see* Chap. 9). The techniques in that protocol have wide applicability, but were specifically designed for use with the optical trapping methods presented here.

By implementing the methods described, researchers will be able to design and carry out a variety of assays for studying forces produced by MT-associated molecular motors.

2 Materials

2.1 Transformation of E. coli *and Expression of the K560-GFP Construct*

1. LB medium: suspend Difco™ LB Broth, Lennox (BD Diagnostic System, Cat. No. DF0402-07-0), in ddH_2O to 20 g/L. Autoclave and store at room temperature.
2. Carbenicillin (100 mg/mL): dissolve carbenicillin disodium (Sigma) in ddH_2O to 100 mg/mL. Sterilize by filtration

through a sterile 0.22 μm Millex® GS filter unit (Millipore). Store at −20 °C in the dark. The working concentration is 100 μg/mL in this protocol.

3. LB/carbenicillin agar plates: suspend Difco™ LB Agar, Lennox (BD Diagnostic System, Cat. No. DF0402-17-0), in ddH_2O to 35 g/L; then autoclave the solution. When the solution cools to ~55 °C, add carbenicillin. Mix well and pour into the plates. After solidification, store the plates at 4 °C.
4. BL21(DE3) competent *E. coli* cells for protein expression (New England Biolabs).
5. Isopropyl β-D-1-thiogalactopyranoside (IPTG) (1 M): dissolve appropriate amount of IPTG (Sigma) in ddH_2O to 1 M; then filter to sterilize. Store at −20 °C.
6. Plasmid DNA: K560-GFP-6×His (pET17b) (gift from the laboratory of R. Vale, University of California, San Francisco).

2.2 Ni-NTA Agarose-Based Protein Purification

For cell pellet from 1 L *E. coli* culture

1. Phenylmethanesulfonyl fluoride (PMSF) (100 mM): dissolve PMSF (Sigma) in isopropanol to 100 mM, and store at −20 °C (*see* **Note 4**).
2. β-mercaptoethanol (βME) (Sigma) (*see* **Note 5**).
3. Mg^{2+}-adenosine 5′-triphosphate (Mg-ATP) (100 mM, pH ~7): dissolve ATP disodium salt (Sigma) in ddH_2O with equimolar $MgSO_4$, and use NaOH to adjust the pH to ~7 (*see* **Note 6**). Store at −20 °C in aliquots.
4. Imidazole (2 M, pH ~8): suspend imidazole (Sigma) in ddH_2O, and then adjust pH to ~8 with HCl. Store at −20 °C.
5. Lysozyme (50 mg/mL): dissolve lyophilized egg-white lysozyme powder (Sigma) in ddH_2O at room temperature to 50 mg/mL, and then keep on ice until use. Prepare fresh solution for each purification (*see* **Note 7**).
6. Lysis buffer (10 mL): 50 mM Tris, 300 mM NaCl, 5 mM $MgCl_2$, and 0.2 M sucrose, pH ~7.5.
7. Resin wash buffer (10 mL): 50 mM Tris, 300 mM NaCl, 5 mM $MgCl_2$, 0.2 M sucrose, and 10 mM imidazole, pH ~7.5.
8. Wash buffer (30 mL): 50 mM Tris, 300 mM NaCl, 5 mM $MgCl_2$, 0.2 M sucrose, and 20 mM imidazole, pH ~7.5.
9. Elution buffer (10 mL): 50 mM Tris, 300 mM NaCl, 5 mM $MgCl_2$, 0.2 M sucrose, and 250 mM imidazole, pH ~8.
10. Storage buffer (30 mL): 80 mM PIPES, 2 mM $MgCl_2$, 1 mM EGTA, and 0.2 M sucrose, pH ~7.
11. Nickel-nitrilotriacetic acid (Ni-NTA) agarose for purification of 6×His-tagged proteins by gravity-flow chromatography (Qiagen).

12. Poly-prep chromatography column (0.8 × 4 cm, BioRad).
13. Econo-Pac® 10DG Desalting Prepacked Gravity Flow Columns (BioRad).
14. Coomassie protein assay reagent (Thermo Scientific, based on Coomassie blue G-250).
15. 10 % SDS-PAGE gel (Amersham ECL™ or similar).
16. SDS running buffer: 25 mM Tris, 192 mM glycine, and 0.1 % SDS (pH 8.3).
17. Ultrasonic homogenizer (Fisher Scientific, model F550 Sonic Dismembrator).

2.3 MT Binding-and-Release Purification of K560

1. BRB80 buffer: 80 mM PIPES (Sigma P6757), 2 mM $MgCl_2$, and 1 mM EGTA, pH ~7.
2. Bovine brain tubulin (10 mg/mL): dissolve one vial of 1 mg lyophilized powder (Cytoskeleton) in 100 μL BRB80 buffer (final concentration 10 mg/mL). Aliquot and flash freeze. Store aliquots at −80 °C (*see* **Note 8**).
3. Paclitaxel (Taxol) (2 mM): dissolve one vial of lyophilized powder (0.2 μmol per vial, Cytoskeleton, Inc.) in 100 μL anhydrous DMSO. Store at −20 °C. The working concentration is 10–20 μM.
4. Mg^{2+}-guanosine 5′-triphosphate (Mg-GTP) (25 mM): dissolve GTP sodium salt (Sigma) with equimolar Mg^{2+} in ddH_2O. Aliquot and store at −80 °C.
5. Adenylylimidodiphosphate (AMP-PNP) (100 mM): dissolve AMP-PNP in ddH_2O to 100 mM and store at −80 °C (*see* **Note 9**).
6. Mg-ATP (100 mM): *see* Subheading 2.2, **step 3**.
7. Dithiothreitol (DTT) (1 M): dissolve DTT in ddH_2O and store at −20 °C. The working concentration is 1 mM.
8. Release buffer: 80 mM PIPES, 2 mM $MgCl_2$, 1 mM EGTA, and 300 mM KCl, pH ~7.
9. Glycerol cushion: 80 mM PIPES, 2 mM $MgCl_2$, 1 mM EGTA, and 60 % glycerol (v/v).
10. Sucrose (2 M): dissolve sucrose in the release buffer to 2 M.
11. Beckman Coulter Optima™ TLX Ultracentrifuge (120,000 maximum rpm).
12. Beckman TLA-120.1 fixed angle rotor (8 × 34 mm, 0.5-mL tube).

2.4 Coating Microspheres with Anti-GFP Antibodies

1. Tabletop centrifuge (e.g., Eppendorf 5430R) cooled to 4 °C with rotor for 1.5-mL microcentrifuge tubes.
2. Low-power bath sonicator (e.g., Branson B-3).

3. Carboxyl-modified polystyrene microspheres: ~1 μm diameter (*see* **Note 10**), and 100 mg/mL suspension (Bangs Laboratories). Store at 4 °C.
4. Activation buffer: 100 mM NaCl and 10 mM MES (2-(*N*-morpholino)ethanesulfonic acid). Adjust to pH 6.0 with NaOH.
5. Coupling buffer (100 mM sodium phosphate buffer): combine 77.4 mL 1 M Na_2HPO_4, 22.6 mL 1 M NaH_2PO_4, and 900 mL ddH_2O. Adjust to pH 7.4 with concentrated NaOH.
6. PBS rinse solution: 137 mM NaCl, 2.7 mM KCl, 4.3 mM Na_2HPO_4, and 1.47 mM KH_2PO_4. Adjust to pH 7.4 with concentrated KOH.
7. Quenching solution (30 mM hydroxylamine hydrochloride ($NH_2OH•HCl$) in PBS): dissolve 0.42 g $NH_2OH•HCl$ in 200 mL PBS rinse solution, and adjust to pH 8.0 with concentrated NaOH.
8. Water-soluble carbodiimide coupling reagent, 1-ethyl-3-(3-dimethylaminopropyl)carbodiimide, hydrochloride (EDAC, Life Technologies), and *N*-hydroxysuccinimidal stabilizing reagent, *N*-hydroxysulfosuccinimide, sodium salt (NHSS, Life Technologies). Store both reagents desiccated (or under argon) at −20 °C (*see* **Note 11**).
9. EDAC quencher: 14.3 M βME. Store at room temperature.
10. 100 mg/mL BSA solution. Store at −20 °C.
11. Anti-GFP antibody stock solution (1–4 mg/mL). Store at −20 °C.

2.5 Pyranose Oxidase/Catalase (POC) Oxygen Scavenger Preparation

1. Pyranose oxidase from *Coriolus* species, 250 U (Sigma Cat. No. P4234; *see* **Note 12** and Swoboda et al. [43] regarding additional steps for experiments involving double-stranded DNA). Store at −20 °C.
2. Catalase (Sigma, Cat. No. C40), store at 4 °C.
3. Tabletop centrifuge (e.g., Eppendorf 5430R) cooled to 4 °C with rotor for 1.5-mL microcentrifuge tubes.
4. Ultrafree Centrifugal Filters (Durapore PVDF 0.1 μm, Cat. No. UFC30VV00).
5. POC storage buffer: 40 mM Tris, 30 % (v/v) glycerol, and 5 mg/mL BSA, pH 7.4.

2.6 Optical Tweezers Setup, Alignment, and Calibration

1. Force-fluorescence microscope.
2. Immersion oil Type A (Nikon).
3. Slide chambers.
4. Trapping beads.

5. 25 mg/mL bovine β-casein (*see* Chap. 9 for preparation instructions).
6. TetraSpeck™ microspheres, 0.1 μm diameter (Life Technologies, Cat. No. T7279).
7. Analysis software. Typically, this software is custom written. However, published software packages are available [44–47], some of which provide libraries that can be used in other programs. Analysis methods to be implemented are described in Subheading 3.8.
8. *Optional*: magnification calibration standard (e.g., MRS-4.1, Geller MicroÅnalytical Laboratory, Inc.).

2.7 Sample Preparation for Optical Tweezers Assay

1. Slide chamber containing surface-immobilized, Cy3-labeled MTs. We suggest using the methods presented in Nicholas et al. (Chap. 9), but if another method is preferred, it can be substituted.
2. BRB80 buffer (*see* Subheading 2.3).
3. 25 mg/mL bovine β-casein (*see* Subheading 2.6).
4. Purified K560, store at −80 °C.
5. 10 mM paclitaxel (Sigma) in DMSO.
6. 100 mM ATP (*see* Subheading 2.2).
7. 1 M DTT (*see* Subheading 2.3).
8. Pyranose 2-oxidase/catalase (POC, *see* Subheading 3.5).
9. 1 M glucose (Fisher), aliquot in ~5 μL volumes and store at −80 °C.
10. Anti-GFP antibody-coated trapping beads (*see* Subheading 3.4).
11. Low-power bath sonicator.
12. Pieces of filter paper cut into strips ~2 in. long and 0.5 in. wide.
13. Vacuum grease (*see* **Note 13**) and cotton-tipped applicator.

2.8 Optical Tweezers Measurement of Motility and Force Generation

1. Force-fluorescence microscope and calibration software.
2. Immersion oil Type A (Nikon).
3. Slide chamber prepared according to Subheading 3.9.

2.9 Force-Fluorescence Microscope Instrumentation

Decisions regarding instrument design depend on many factors, including the desired precision, requirements for optical tweezers force feedback and beam steering, available space and budget, and the number of required fluorescence channels. As a result, instruments vary widely among laboratories, and we will therefore not attempt to give detailed instructions for the design and construction of the optical tweezers/TIRF fluorescence microscope. See, for example, Lee et al. [48] for a hands-on procedure for

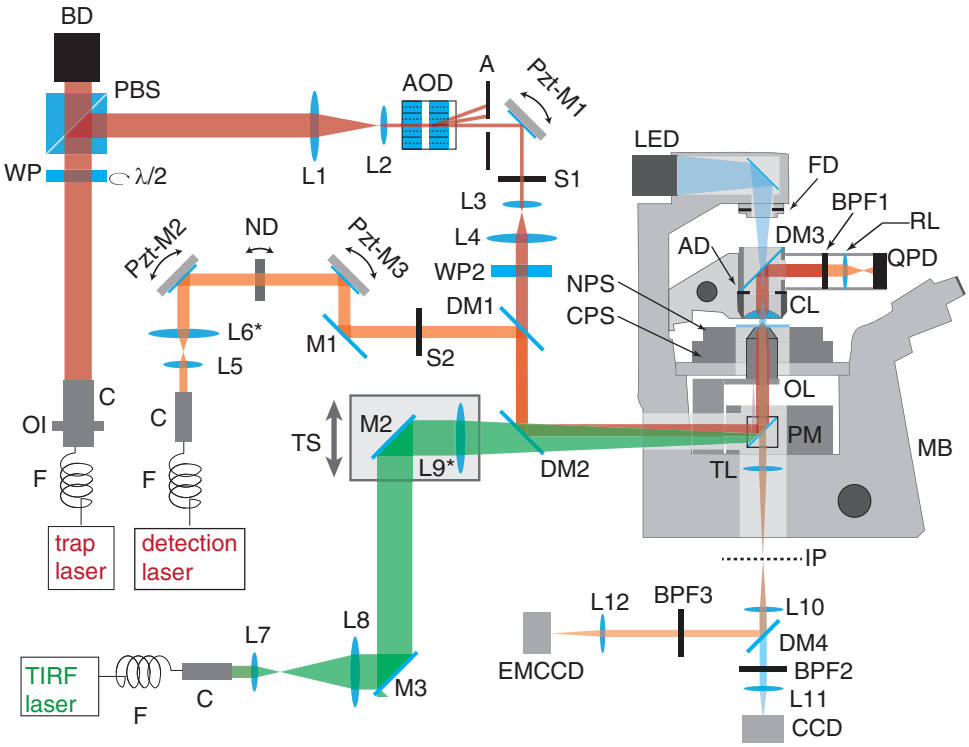

Fig. 3 Force-fluorescence microscope (see text for description). *A* aperture; *AD* aperture diaphragm; *AOD* acousto-optic deflector; *BD* beam dump; *BPF* band-pass filter; *C* beam collimator; *CCD* charge-coupled device (for bright-field detection); *CL* condenser/collection lens; *CPS* coarse-positioning stage; *DM* dichroic mirror; *EMCCD* electron-multiplying CCD (for fluorescence detection); *F* single-mode, polarization-maintaining optical fiber; *FD* field diaphragm; *IP* image plane; *L* lens; *L** lens mounted on a translation stage for fine focus adjustment; *LED* light-emitting diode; *M* mirror; *MB* microscope body; *ND* neutral density filter; *NPS* nanopositioning stage; *OI* optical isolator; *OL* objective lens; *PBS* polarizing beam splitter; *PM* polychroic mirror; *Pzt-M* piezo-driven mirror mount; *QPD* quadrant photodiode; *RL* relay lens; *S* shutter; *TL* tube lens; *TS* translation stage; *WP* half-wave plate

building a simple optical trap on an inverted fluorescence microscope, Selvin et al. [49] for a protocol for constructing a simple TIRF microscope, and Neuman and Block [26] and van Mameren et al. [50] for excellent discussions of many relevant design considerations for optical tweezers. Instead, we will outline a simplified version of the force-fluorescence microscope in our laboratory and make note of some practically important design and construction details common to all such microscopes. For the protocol instructions, we assume the optical tweezers setup in Fig. 3 and refer to components according to the labels therein.

The illumination pathways consist of beams for trapping, back focal plane detection (*see* **Note 14**), bright-field imaging, and TIRF microscopy. All optics should have antireflection coatings for the appropriate laser wavelengths. The *trapping laser* (1,064 nm)

passes through a combined collimator and optical isolator (OI, to prevent back-reflection into the laser resonator via the glass fiber) and a variable beam splitter consisting of a computer-controlled wave plate (WP) and polarizing beam splitter (PBS), allowing precise control of the transmitted laser power (and therefore the trapping spring constant, *k*). The beam then passes through a two-channel acousto-optic deflector (AOD), the (1, 1)-order diffracted beam is selected using an aperture (A), and the beam is re-expanded to fill the rear entrance pupil of the microscope objective lens (OL). The "pivot point" within the AOD is conjugate telecentric to the back focal plane of the microscope objective, so that rotations of the diffracted beam originating from the AOD plane produce translations of the focus in the sample (front focal plane of the objective). The computer-controlled, piezo-electric-driven mirror mount following the AOD (Pzt-M1) is positioned such that when it rotates, it mostly translates the beam in the back aperture of the objective. Together, this mirror and the AOD allow precise control of the position and angle of the trapping beam as it enters the objective lens (note that this simplified diagram omits additional lenses required to achieve the aforementioned AOD and Pzt-M1 optical mappings). The trap is turned on and off by means of a simple mechanical shutter (S1). The half-wave plate (WP2) positioned directly before the microscope allows rotation of the laser beam polarization (*see* **Note 15**).

After beam expansion, the *detection beam* (830 nm) overlaps the trapping beam as it enters the microscope. Two beam steering mirrors (Pzt-M2 and Pzt-M3) work as a pair to precisely control the detection beam alignment. A neutral density filter (ND) on a computer-controlled, motorized mount allows switching of the detection beam from low power (~40 μW, normal operation for detection) to higher power (~3 mW, for trapping and visualization during alignment). Like the trapping beam, the detection beam is also shuttered (S2).

The *TIRF laser* (532 nm, for Cy3 excitation) is expanded in order to illuminate the entire visible sample plane and focused by lens L9* (f = 500 mm) onto the back focal plane of the objective. M2 and L9* are mounted on a translation stage that allows the laser focus to be moved laterally (off-axis) in the rear aperture of the objective, thereby adjusting the angle of the beam exiting the objective for total internal reflection at the cover slip surface.

The *LED* (470 nm) provides bright-field illumination. The detection pathways consist of bright-field and fluorescence imaging (using a CCD and EMCCD, respectively) and back focal plane detection of the trapped bead position relative to the detection beam (using a quadrant photodiode, QPD). The *bright-field and fluorescence images* are separated using an appropriate dichroic mirror (DM4) and filtered with band-pass filters at 470 and 580 nm, respectively (primarily to block reflected laser light from the

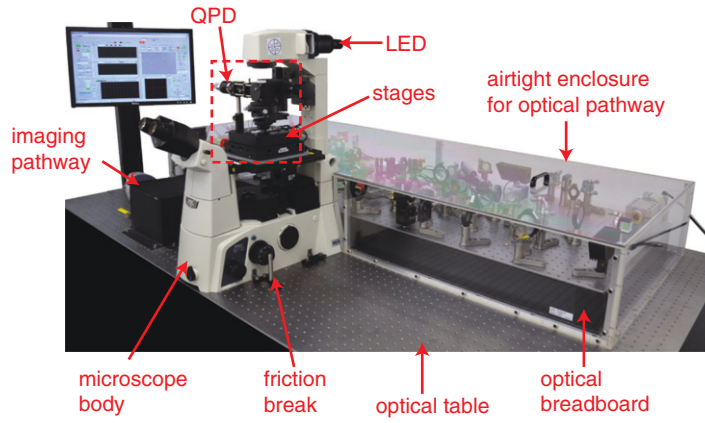

Fig. 4 Force-fluorescence trapping microscope. Note the optical pathway elevated on an optical breadboard and enclosed in an airtight box. The friction break [165] consists of an optical post or other rigid element bolted firmly to the table and pressed against the microscope fine-focus knob to prevent drift of the objective over time. The region demarcated by the red dashed line (back focal plane imaging arm) is shown in greater detail in Fig. 12. Refer also to Fig. 3

trapping beam). The images are then relayed onto the appropriate detectors and can be viewed simultaneously in the control software. Magnification should be chosen so that the effective pixel size of both imaging systems (physical pixel size divided by magnification) is close to equal. This allows the images to be easily registered and overlaid with minimal image processing.

The *back focal plane detection* arm collects the trapping and detection beams, filters out the trapping beam, and uses a relay lens (RL) to image the back focal plane of the condenser lens (CL) onto a QPD. The voltage signals from each quadrant are low-pass filtered at the Nyquist frequency (half the data acquisition frequency used by the software) to prevent aliasing.

Note that the polychroic mirror (PM) is a custom-designed element, which simultaneously reflects all laser beams, while transmitting the bright-field and fluorescence images (in our instrument, this mirror allows for simultaneous imaging of two fluorescence channels in addition to the one shown here).

Components of interest:

1. Foundational components: thermally and acoustically isolated microscope room (acoustic noise criteria, NC30 or 45; vibration criteria, VC-D or VC-E; temperature stability, ±0.2 °C or better), vibration isolation table (Technical Manufacturing Corp., 24 in. thick, Part No. 784-37397-01), and optical pathway enclosure (Fig. 4) with optical breadboard (Newport Corp., Part No. RG-26-4-ML) (*see* **Note 16**).

2. Inverted microscope body with illumination pillar (Nikon model Eclipse Ti-U). For stability, the rubber feet on the base of the microscope are removed, and the body is firmly bolted to the optical table using right-angle steel brackets.
3. 100× oil-immersion, high-numerical aperture (NA), apochromatic microscope objective lens (*see* **Note 17**), NA 1.49 (Nikon, model CFI Apo TIRF 100× Oil).
4. High-NA oil condenser lens, NA 1.4 (Nikon, model HNA-Oil).
5. Coarse-positioning stage (Physik Instrumente, Part No. M-686.D64; *see* **Note 18**).
6. Nanopositioning stage (Physik Instrumente, Part No. P-517.3CD).
7. 1,064-nm trapping laser: linearly polarized, diode-pumped CW Ytterbium laser with 10-W maximum output (IPG Photonics, Part No. YLR-10-1064-LP; *see* **Note 19**) with polarization-maintaining, single-mode optical fiber output and combined beam collimator/expander/optical isolator (Part No. ISO-1080-100).
8. 830-nm detection laser with polarization-maintaining, single-mode optical fiber and beam collimator (Qioptiq, Part No. iFLEX-P-10-830-0.7-50-NP).
9. Shutters and shutter controllers (Thorlabs, Part Nos. SH05 and SC10, respectively).
10. Picomotor™ piezo-controlled mirror mounts (New Focus/Newport Corp., model 8821; *see* **Note 20**).
11. High-capacity beam dump for trapping laser (Thorlabs, Part No. BT510).
12. Acousto-optic deflector (IntraAction Corp., Part No. DTD-274HD6; *see* **Note 21**).
13. Quadrant photodiode (QPD) and power supply (Electro-Optical Systems, Inc., Part Nos. S-078-QUAD-E4/1MHZ and PS1, respectively) with 1 MHz bandwidth and near-maximal output (~0.55 A/W) at 830 nm.
14. Two dual-channel low-pass filters (Stanford Research Systems, Inc., SR640), one channel for each QPD quadrant signal (*see* **Note 22**).
15. Digital acquisition board (National Instruments, Part No. 6281).
16. 532-nm laser for Cy3 TIRF excitation (MeshTel/INTELITE, Inc., Part No. GM32-100GSA-P10) with polarization-maintaining, single-mode optical fiber and integrated collimator (Qioptiq).
17. Achromatic doublet lens with antireflection coating for visible wavelengths, for TIRF illumination ($f = 500$ mm; diameter = 50.8 mm; Newport Corp., Part No PAC091AR.14).

18. kineMATIX fiber manipulators (Qioptiq) for laser collimator alignment (*see* **Note 23**).
19. Polychroic mirror (Chroma Technologies, custom Part No. zt488/532/633/830/1064rpc; *see* **Note 24**).
20. Dichroic mirrors designed for laser beam combination (Chroma Technologies or Semrock, Inc.; *see* **Note 25**).
21. Piezo-driven rotation stage (Newport Corp, Part No. AG-PR100) for half-wave plate rotation.
22. LED (Thorlabs, Part No. M470L2) for bright-field imaging.
23. CCD for bright-field imaging (The Imaging Source, Part No. DMx 31BU03).
24. EMCCD for MT visualization (Andor Technology, model Luca S 658; *see* **Note 26**).
25. Trap control and analysis software (programmed in-house using a combination of National Instruments LabView and MathWorks MATLAB; *see* **Note 27**).

3 Methods

3.1 Transformation of BL21(DE3) Competent E. coli Cells and Expression of the K560 Construct

This protocol describes *E. coli*-based expression of K560-GFP [42]. **Steps 1–7** describe BL21(DE3) competent *E. coli* cell transformation with the K560-GFP plasmid, and subsequent steps describe cell growth for protein expression.

1. Take out two plates per transformation from 4 °C storage, and set them on the bench for 0.5 h to allow them to rise to room temperature. Place plates upside-down to prevent condensation of water on the agar, and label them.
2. Thaw one vial (50 μL) of *E. coli* competent BL21(DE3) cells on ice for 10 min (*see* **Note 28**).
3. Add 1–5 μL plasmid DNA (≥1 ng) into the tube; gently flick the solution 4–5 times to mix cells and plasmid (do not vortex).
4. Incubate on ice for 30 min (do not mix) (*see* **Note 29**).
5. Heat shock the cells at 42 °C in water bath for exactly 10 s; do not mix (*see* **Note 30**).
6. Put the tube on ice for 5 min (do not mix).
7. Spread 2 μL cells with 98 μL LB on one plate evenly, and the rest onto another plate. Seal the plates with Parafilm and incubate them at 37 °C overnight. Colonies should appear after 12 h.
8. Pick a single colony and inoculate it in 5 mL LB/carbenicillin in a test tube. Shake vigorously at 37 °C overnight.
9. Check the optical density of the overnight culture at wavelength of 595 nm (OD_{595}). Inoculate an appropriate amount

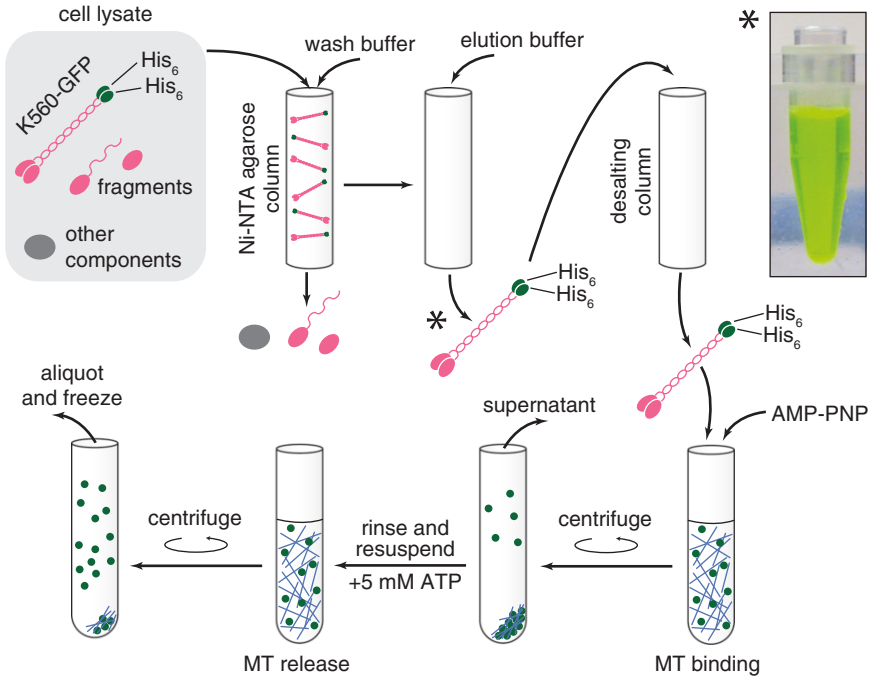

Fig. 5 K560 purification. The full-length motor is first purified from other proteins and incomplete fragments by nickel-nitrilotriacetic acid (Ni-NTA) chromatography, isolating only those proteins with the polyhistidine (His_6) tag (marked by the *asterisk*; note the inset photograph showing the elution with intense *green color* due to GFP). Next, His_6-containing fragments (degradation products) and motors incompetent to bind MTs are removed by MT binding and sedimentation in the presence of AMP-PNP. Motors unable to release MTs in response to saturating concentrations of ATP are then removed, and the purified, functional K560 is aliquotted, flash-frozen in liquid nitrogen, and stored

into 50 mL LB/carbenicillin such that the starting $OD_{595} \approx 0.1$. Incubate culture at 37 °C for ~2–3 h with vigorous shaking. OD_{595} should reach ~0.6–1.

10. Inoculate the 50-mL culture into 1 L LB/carbenicillin for ~2–3 h until OD_{595} reaches ~0.8–1 (*see* **Note 31**).
11. Cool culture on ice until temperature is <20 °C. Reserve 10 μL for gel. Add IPTG to final concentration of 0.1–0.2 mM. Shake vigorously overnight at 18 °C (*see* **Note 32**).
12. Harvest cell culture by centrifugation at 6,000 rpm (4,000 rcf) for 15 min at 4 °C. Discard the supernatant. Store the cell pellet in a 50-mL Falcon tube at −80 °C (*see* **Note 33**).

3.2 Ni-NTA Agarose-Based Protein Purification

This is the first step in purifying the K560-GFP construct expressed above. It utilizes the polyhistidine tag included in the construct and is based on methods given by Bornhorst and Falke [51] and Stock and Hackney [52] (*see* Fig. 5).

1. Chill all the buffers on ice; add βME (final 5 mM) and Mg-ATP (final 50 μM) to all the buffers right before purification. Add protease inhibitor PMSF into lysis buffer to 0.5–1 mM (*see* **Note 34**). Add dissolved lysozyme into lysis buffer to 1–2 mg/mL.
2. Keep the pellet at room temperature until it is almost completely melted. Add 10 mL lysis buffer to the pellet, and gently invert the tube several times until the solution is homogenous. Incubate on ice for 30 min. The solution will become viscous due to the release of DNA from the cells.
3. To lyse the cells, sonicate the solution at 35 % power for 20 cycles of 30 s pulsing with 2.5-min rests between pulses (*see* **Note 35**). Keep the container holding the solution in contact with ice all the time.
4. Supply the lysate with 10 mM imidazole and 0.5 mM PMSF after sonication.
5. Clear lysate by centrifugation at 30,000 rcf for 30 min at 4 °C.
6. Wash 2 mL Ni-NTA agarose with 10 mL resin wash buffer in a BioRad column, and transfer the agarose to a prechilled 50-mL Falcon tube.
7. Add cleared lysate (reserve 2 μL for SDS-PAGE gel analysis) to Ni-NTA agarose, and nutate the mixture at 4 °C for 1 h in the dark.
8. In a 4 °C cold room, pour the mixture into a BioRad column; reserve 2-μL flow-through for gel.
9. Wash the resin with 3 × 10 mL wash buffer; collect 2 μL from each wash fraction for gel.
10. When the solution is almost drained, cap the column tightly. Add 1 mL elution buffer, resuspend the resin, and incubate for 5 min. Elute 0.5 mL into a chilled 1.5-mL microcentrifuge tube. Hereafter each time add 0.5 mL elution buffer, incubate for 5 min, and then elute 0.5 mL.
11. Estimate eluted protein concentration on a 96-well plate. Basically, add 1–2 μL eluent from each fraction to 200 μL Coomassie blue reagent, mix well, and identify the wells with the most intense blue color.
12. Wash a BioRad desalting column with 2 × 10 mL storage buffer.
13. Combine fractions that are most concentrated (typically ~4–6 fractions), and load the solution onto the desalting column.
14. Allow the solution to sink into the desalting column, and discard the first 2-mL flow-through.
15. Each time add 0.5 mL storage buffer and collect 0.5 mL. Estimate protein concentration on the 96-well plate, and

combine concentrated fractions. Determine bulk protein concentration using Bradford assay (*see* **Note 36**). Run a SDS-PAGE gel to estimate purity and yield.

16. Aliquot and flash freeze the solution. Store at −80 °C. For further purification via MT binding and release, 100 μL aliquots are recommended.

3.3 MT Binding-and-Release Purification of K560

Ni-NTA agarose-based purification isolates all proteins with a polyhistidine tag and native proteins with intrinsic high affinity for Ni. Here, we further purify this fraction to isolate "full-length," functional (non-degraded/cleaved) kinesins (*see* **Note 36**). **Steps 1–7** describe how to polymerize tubulin to form MTs, while the subsequent steps describe kinesin purification via MT-mediated pulldown and nucleotide-induced release (Fig. 5).

1. Calculate the amount of tubulin needed. Three- to fourfold excess molar amount of tubulin over kinesin is recommended. For example, for 100 μL of 1 mg/mL kinesin solution, use 400 μg tubulin.
2. Add 0.4 μL of 100 mM Mg-GTP (1 mM) and 0.4 μL of 0.1 M DTT (1 mM) to 40 μL of 10 mg/mL tubulin. Incubate at 37 °C for 15 min.
3. Add 4 μL of 0.2 mM paclitaxel (final 20 μM paclitaxel and 10 % DMSO), and incubate at 37 °C for 15 min (*see* **Note 37**).
4. Add 3 μL of 2 mM paclitaxel (final 20 μM) and 0.3 μL of 1 M DTT (final 1 mM) to 300 μL glycerol cushion and to 300 μL BRB80 buffer. Pipette up and down gently to mix well. Transfer the glycerol cushion to a clean 0.5-mL TLA-120.1 tube. Lay the polymerized tubulin solution on top of the glycerol cushion.
5. Use TLA-120.1 rotor to spin the MTs through the glycerol cushion for 10 min at 80,000 rpm (227,000 rcf average; k-factor 18.3) at room temperature.
6. Rinse top of the solution with 100 μL of BRB80 buffer. Carefully take off the supernatant, and then wash the pellet with 100 μL of BRB80.
7. Gently resuspend the pellet in 40 μL of BRB80 to render ~10 mg/mL MTs.
8. Add 1 μL of 0.1 M AMP-PNP (final 1 mM) and 1 μL of 2 mM paclitaxel (final 20 μM) to 100 μL of motor solution. Incubate on ice in the dark for 5 min.
9. Warm the motor solution to room temperature; then add 40 μL of prepared MTs. Incubate at room temperature for 15 min in the dark (reserve 1 μL for gel).
10. Add DTT and paclitaxel to 300 μL glycerol cushion, 200 μL BRB80, and 100 μL release buffer (final 1 mM and 20 μM, respectively).

11. Add the glycerol cushion to TLA120.1 tube, carefully lay the mixture on top, and spin at 80,000 rpm (227,000 rcf average; k-factor 18.3) for 12 min at room temperature (reserve 1 μL of supernatant for gel).
12. Wash top of the cushion with 100 μL BRB80, remove supernatant, and then wash pellet with 100 μL BRB80 (be careful not to disturb the pellet).
13. Resuspend pellet in 100 μL release buffer with 5 mM Mg-ATP (reserve 1 μL for gel), and incubate at room temperature for 5 min.
14. Spin at 80,000 rpm (227,000 rcf average; k-factor 18.3) for 10 min at room temperature.
15. Transfer supernatant (which contains released kinesin) to a prechilled 1.5-mL microcentrifuge tube on ice, and add 33 μL prechilled 2 M sucrose (reserve 1 μL for gel).
16. Aliquot the solution into small tubes in 3 μL volumes (or appropriate amount for future experiments), flash freeze, and store at −80 °C.
17. Run a 10 % SDS-PAGE gel to determine the released fraction (*see* **Note 38**).

3.4 Coating Microspheres with Anti-GFP Antibodies

In this procedure, microspheres are coated with anti-GFP antibodies and BSA (Fig. 6). These coated microspheres will bind K560-GFP in the optical trapping assay. The protocol given here is similar to the one we reported previously [53]. *See* ref. [54] for a detailed discussion of the relevant chemistry.

1. Briefly vortex microsphere stock suspension to evenly distribute the microspheres. Pipette 100 μL of the microsphere stock into a 1.5-mL microcentrifuge tube. Add 900 μL activation buffer to the microspheres and mix well using the pipette.
2. Centrifuge at 1,200 rcf for 15 min at 4 °C. Carefully remove and discard the supernatant (do not remove any microspheres), and resuspend with 1 mL of activation buffer. Vortex and sonicate for 10–20 s in the low-power bath sonicator to ensure there is no aggregation (*see* **Note 39**).
3. Repeat **step 2** two more times. During the last centrifugation, obtain the EDAC and NHSS from the freezer. Allow them to equilibrate to room temperature before opening (*see* **Note 11**).
4. In a separate 1.5-mL microcentrifuge tube, weigh 5 mg of EDAC and 10 mg of NHSS and immediately add the 1 mL bead suspension to activate the beads. Mix well and sonicate for 10 s. Incubate for 30 min at room temperature while gently mixing on a rocking platform.

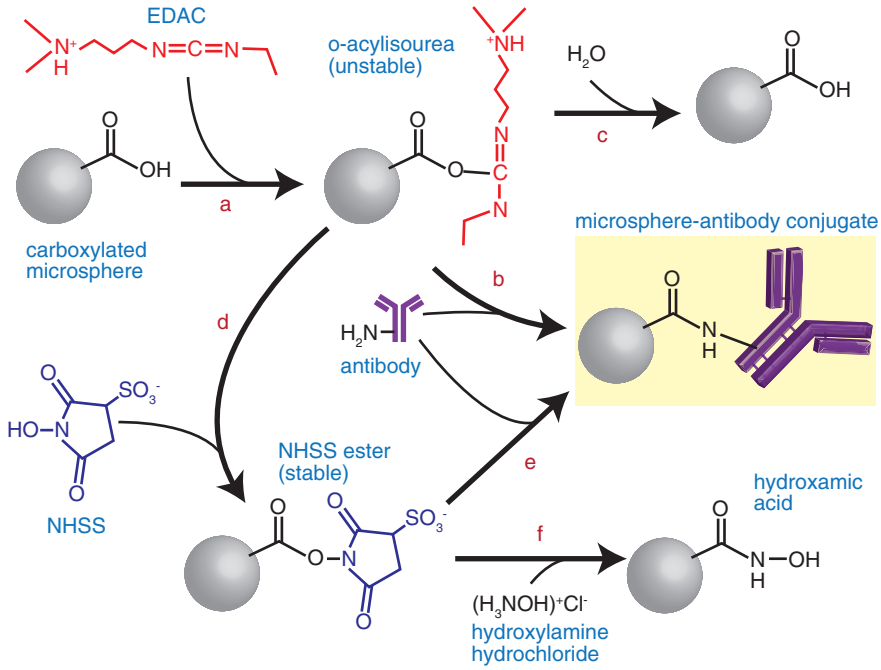

Fig. 6 Coupling antibodies to optical trapping microspheres. First, a microsphere bearing surface carboxyl groups reacts (**a**) with the carbodiimide EDAC (1-ethyl-3-(3-dimethylaminopropyl)carbodiimide) to form an unstable *O*-acylisourea intermediate. This short-lived species is reactive toward primary amines and thus capable of forming stable, covalent amide bonds with lysyl residues on the antibody surface (**b**) and yielding an isourea byproduct (not shown). However, this *O*-acylisourea is also readily and rapidly hydrolyzed, yielding the original carboxyl group (**c**). Adding NHSS (3-sulfo-*N*-hydroxysulfosuccinimide) to the reaction greatly enhances microsphere–antibody coupling efficiency by forming a relatively water-stable, but amine-reactive NHSS ester (**d**) that can likewise bind antibodies (**e**). BSA (not shown) is added with the antibody and also binds via its surface lysines, thus blocking the remainder of the microsphere surface. After antibodies and BSA are bound, any residual NHSS esters are removed by adding hydroxylamine (**f**), which reacts with the ester to form hydroxamic acid

5. *Optional*: add 1.4 μL of 14.3 M βME (20 mM final concentration) to quench the EDAC reaction (*see* **Notes 5** and **40**). Invert gently back and forth by hand for ~30 s.
6. Repeat **step 2** three times, using coupling buffer in place of activation buffer (*see* **Note 41**) and using 250 μL for the final resuspension. During the final centrifugation, thaw the BSA and antibody solutions and place them on ice.
7. In a separate tube, mix 55 μL of 100 mg/mL BSA with a volume of antibody corresponding to ~0.2–0.5 mg (~6 mg total protein). Add coupling buffer to bring the total volume to 500 μL. Mix well. Then add the microsphere mixture to the protein solution, mixing rapidly, but gently with the pipette (*see* **Note 42**). Sonicate briefly (3–5 s).
8. Allow the mixture to react for 2–4 h at room temperature (or overnight at 4 °C) with constant nutation.

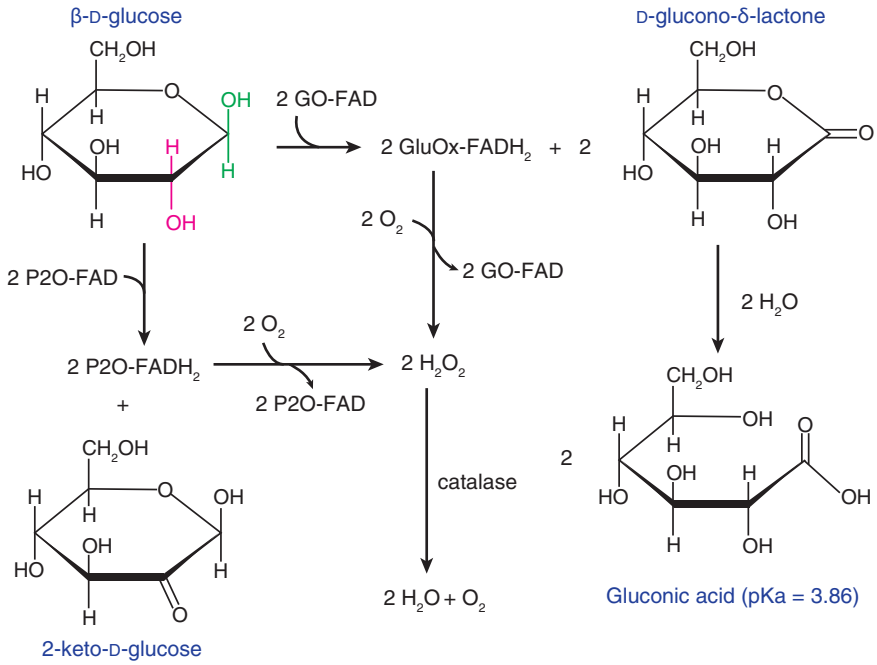

Fig. 7 Pyranose 2-oxidase (P2O) oxygen scavenging system, with comparison to glucose oxidase (GO). Both flavoenzymes contain flavin adenine dinucleotide (FAD) prosthetic groups that are reduced by glucose, thereby generating $FADH_2$ and removing two hydrogens from the sugar. Whereas GO removes hydrogens from the C1 position (*green*), P2O acts on C2 (*magenta*), yielding D-glucono-δ-lactone and 2-keto-D-glucose, respectively. Whereas 2-keto-D-glucose is stable, in the presence of water, D-glucono-δ-lactone hydrolyzes to gluconic acid, thereby acidifying the reaction solution. The reduced enzymes ($FADH_2$ forms) are oxidized by O_2, regenerating the original enzymes and producing H_2O_2, which is converted by catalase to H_2O and O_2. In the net reaction, for each O_2 removed, two glucose molecules are consumed, and for GO, two gluconic acid molecules are generated. Although β-D-glucose, the substrate for GO, is shown, P2O has no anomeric preference and can also catalyze the oxidation of α-D-glucose [43, 111]

9. Repeat **step 2** twice using PBS rinse solution in place of activation buffer. After the final centrifugation, resuspend in 1 mL of quenching solution.
10. Incubate in quenching solution for 30 min at room temperature (or overnight at 4 °C; *see* **Note 43**).
11. Repeat **step 2** three times using PBS rinse solution in place of activation buffer. After the final centrifugation, resuspend in 100 μL of PBS or assay buffer. Add 0.5 μL of 100 mg/mL BSA, mix, and store at 4 °C (*see* **Note 44**).

3.5 Pyranose Oxidase/Catalase (POC) Oxygen Scavenger Preparation

The procedure below yields a solution of approximately 600 U/mL pyranose oxidase and 18 kU/mL catalase, which work together to deplete oxygen from the sample chamber in the trapping assay (Figure 7 demonstrates the basis for oxygen removal and compares POC to the conventional system using glucose oxidase; *see* **Note 12**).

This is diluted 200× in the trapping assay, to yield 3 and 90 U/mL pyranose oxidase and catalase, respectively.

1. Remove catalase from refrigerator, invert bottle several times to suspend contents evenly, and transfer 75 μL to a 1.5-mL microcentrifuge tube on ice.
2. Centrifuge at 20,000 rcf for 5 min at 4 °C. Remove the supernatant (which contains antimicrobial thymol preservative), estimate its volume with the pipette, and discard. Resuspend the pellet in 200 μL ddH_2O.
3. Centrifuge again at 20,000 rcf for 5 min at 4 °C. Discard the supernatant. Resuspend the pellet in POC storage buffer in a volume equal to that of the supernatant removed in **step 2**. Keep on ice.
4. Remove the pyranose oxidase from the freezer and place the vial on ice. Add 350 μL of POC storage buffer to dissolve the pyranose oxidase. Pipette up and down gently, avoiding bubbles and dissolving all protein in the vial. The solution will have a bright yellow color owing to the flavin adenine dinucleotide (FAD) prosthetic group in the enzyme.
5. Transfer the pyranose oxidase solution to a clean 1.5-mL microcentrifuge tube, and add 22 μL of the catalase solution. Measure the volume with the pipette.
6. Using a sufficient volume of POC storage buffer to bring the POC solution to 415 μL total, rinse the pyranose oxidase vial, and add the rinse to the POC solution.
7. Spin filter the solution two times using the same centrifuge settings as above (split the solution between two different spin columns for the first centrifugation to avoid clogging the filter).
8. Aliquot in 3 μL volumes in the smallest plastic tubes available, snap freeze in liquid nitrogen, and store at −80 °C.

3.6 Optical Tweezers Setup

Here we describe the initial adjustments and calibrations necessary to perform quantitative experiments with the optical tweezers. These procedures need only be performed once during initial instrument setup, but it is good practice to check the adjustments periodically. The aims of these steps are to (a) align the axes of the AOD, CCD, and nanopositioning stage, (b) determine the AOD beam deflection in response to applied voltage, and (c) align the bright-field and fluorescence images. As a starting point, we assume that the trapping laser is coupled into the microscope and coarsely aligned along the optical axis and that TIRF imaging is established. The lateral position of the trapping beam focus should be recorded and displayed in real time on the CCD image as a point of reference (e.g., as a crosshair superimposed on the image).

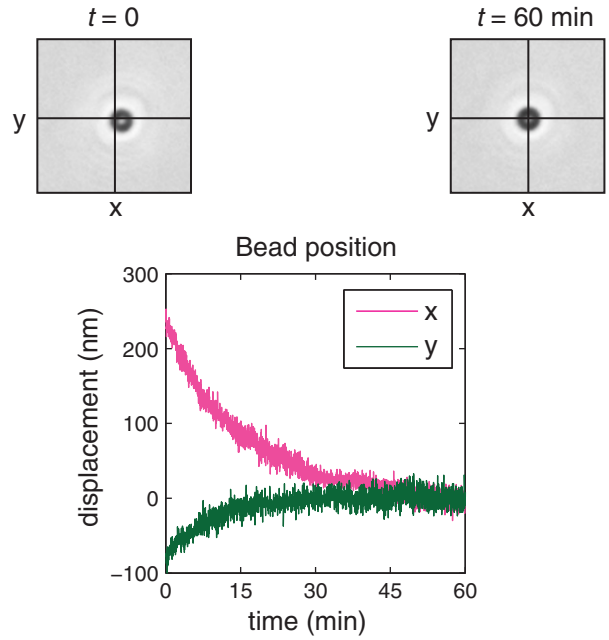

Fig. 8 Thermal equilibration of the optical tweezers laser pathway. When the optical trapping laser is initially powered on, the trap center is typically offset from its previous stable position (*left-hand image*; the cross to the *upper left* of the bead is the stable position to which the bead moves after the optical elements in the pathway expand due to heating by the trapping laser). The new position is typically very close (tens of nanometers) to the stable position during the preceding use of the instrument (*right-hand image*). The graph shows a representative example of microsphere movement over time as the optical pathway thermally equilibrates. The position traces were obtained by tracking the trapped microsphere in images acquired every second for 60 min, using a simple centroid-finding algorithm. The paths shown are followed fairly consistently each time the instrument is powered on before experiments. The instrument requires approximately 45–60 min to fully stabilize

Steps 1–4 describe the thermal equilibration of the instrument and initial focusing, as required whenever the instrument is used. For these adjustments, use a high trap power (~100 mW entering the back aperture of the objective) in order to reduce bead diffusion.

1. Turn on the trapping and detection lasers and all associated electronics, QPD last. Set the output power of the trapping laser to 100 % (or whichever setting exhibits the best power stability). Open shutters S1 and S2, and allow the trap to thermally equilibrate for at least 30–45 min (*see* Fig. 8 and **Note 45**).
2. Place a drop of immersion oil on the objective lens. Fix the slide chamber securely on the nanopositioning stage, cover slip side down, and raise the objective to contact the center of the cover slip. On the top of the slide chamber, apply approximately 0.2 mL of immersion oil, and lower the condenser to make contact with the oil (*see* **Note 46**).

3. Turn on the bright-field LED and observe the CCD image. Raise the objective until microspheres come into focus. Then use the fine focus to move the objective down until new beads stop coming into focus, and the visible beads appear white. These beads are diffusing into the cover slip surface, just slightly above the focal plane. Move the objective upward just until these beads appear dark.
4. Close the field diaphragm almost completely. Adjust the condenser height until the edges of the diaphragm come into sharp focus. This achieves Köhler illumination. Lock the condenser position and open the field diaphragm to just beyond the field of view.

The following steps align the CCD, nanopositioning stage, and AOD axes (see ***Note 47****).*

5. Prepare a slide chamber and flow in 15 μL of trapping beads diluted ~1:1,000 from stock in BRB80. Incubate for 15 min to allow the beads to bind the surface, and flow in 20 μL of 1 mg/mL casein in BRB80. Incubate 5 min, and flow in 15 μL of trapping beads diluted ~1:1,000 from stock in the 1 mg/mL casein solution. Seal the chamber ends with vacuum grease, and place the chamber on the microscope (follow **steps 2–4** above).
6. Focus on the stuck beads so they appear dark, and move one to the marked focal position of the trapping beam (this should be the center of the CCD field of view). Move the stage in a 3 μm × 3 μm grid pattern with 200-nm steps, centered at the trapping beam mark. Record an image with the CCD at each position (this process should be automated).
7. Create a minimum projection image for the stack of images acquired in the previous step (either in the trap software itself or using an analysis program such as NIH ImageJ 55, 56). This will form a dark square.
8. Draw a box around the square to determine the rotation of the CCD relative to the stage. Carefully rotate the CCD to correct this rotation.
9. Repeat **steps 6–8** until there is no observable rotation of the CCD relative to the stage.
10. Trap a bead, and move it close to the cover slip surface (~100 nm above the point of bead–cover slip contact, as judged by eye). Apply appropriate voltages to the AOD driver frequency modulation inputs to step the bead in a similar grid to that used in **step 6**, again recording images at each position.
11. Create a minimum projection image, as in **step 7**. Overlay this image with the final image formed after adjusting the CCD (**step 9**). Draw lines along the edges of each square to determine the angle of rotation θ (in radians) of the AOD axes relative to the stage axes (*see* **Note 48**). The sign of θ is positive if

the AOD is rotated *clockwise* relative to the stage and negative otherwise.

12. Apply a counterclockwise rotation transformation (in the software) to the voltages sent to the AOD, of the form

$$A_{x,r} = A_{x,0} + (A_x - A_{x,0})\cos(\theta) - (A_y - A_{y,0})\sin(\theta) \text{ and}$$
$$A_{r,y} = A_{y,0} + (A_y - A_{y,0})\cos(\theta) + (A_x - A_{x,0})\sin(\theta),$$

where A_x and A_y are the original voltages in the x and y directions, respectively, $A_{x,0}$ and $A_{y,0}$ are constant offsets (if any) applied when the beam is in its center position, and $A_{r,x}$ and $A_{r,y}$ are the corresponding voltages after rotation (*see* **Note 49**).

13. Recheck the rotation of the AOD axes relative to the stage, following **steps 10** and **11**, while applying the rotation in **step 12** to each point. If the rotation is corrected, the transformation in **step 12** should be applied henceforth to all beam steering by the AOD.

The following steps determine the distance moved by the trap in response to voltage applied to the AOD:

14. Determine the effective pixel size of the CCD. Using the same sample chamber as in the previous steps, move the bead by several known distances, saving an image at each position (*see* **Note 50**). Track the bead position, and determine the separation in pixels D_{px} between subsequent bead positions. Divide the known distance moved D_{nm} by D_{px} to find the effective pixel size in nanometers $P_{\text{nm}} = D_{\text{nm}}/D_{\text{px.}}$ Repeat this measurement several times and take the average. *Optional*: repeat the computation of P_{nm} using a magnification calibration standard such as the MRS-4.1. The answers from both methods should agree to within ~2 nm/pixel or less.

15. Trap a bead. Apply known voltages to the AOD driver frequency modulation inputs (while applying the rotation transformation determined above), in order to step the bead in various lines, saving an image at each position. Track the bead centroid position (in pixels) in each image, and plot the x and y pixel positions vs. the applied voltage. Fit a line to these data to determine the distances in pixels moved per volt applied (*see* **Note 51**), i.e., the line slopes $L_{x,\text{px}}$ and $L_{y,\text{px}}$ for x and y, respectively.

16. Calculate the conversion factor W needed to determine the voltage required to move the trapping beam by a given distance: $W_x = P_{\text{nm}} \times L_{x,\text{px}}$ (and identically for the y direction). For a desired displacement Δx, a voltage $A_x = \Delta x / W_x$ must be applied to the AOD. Save these conversion factors and apply them permanently in the trap control software.

The following steps align the CCD and EMCCD:

17. Prepare a slide chamber (using a clean, but non-silanized cover slip) with fluorescently labeled 100-nm TetraSpeck beads in 1 M

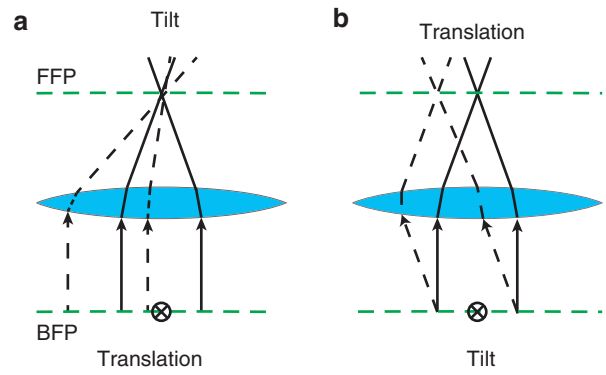

Fig. 9 Important optical relationships for focusing a collimated beam. BFP, back focal plane; FFP, front focal plane. Solid rays represent a beam perfectly aligned with and centered on the optical axis. (**a**) Pure translation of the beam in the back aperture leads to tilting of the beam as it focuses in the FFP, but does not change the position of the focus. This induces asymmetry in intensity pattern of the retroreflected beam. (**b**) Pure tilting of the beam in the BFP leads to translation of the focus in the FFP, essentially without affecting the beam angle as it approaches the FFP. This shifts the position of the intensity pattern of the retroreflected beam, with minimal effects on the intensity distribution

NaCl solution (this will cause the beads to stick to the glass surface) and place it on the microscope (follow **steps 2–4** above).

18. Bring the beads into sharp focus in the bright-field image, and move a bead to the center of the CCD image. Turn on the 532-nm laser and observe the fluorescence channel. Identify the fluorescent spot corresponding to the bead in the center of the CCD field of view, and carefully adjust the position of the image on the EMCCD (by moving the EMCCD itself and/or using the appropriate mirrors in the imaging pathway) so that the spot is also centered on the EMCCD.
19. Move to a region where there are several beads visible on both cameras. Overlay the CCD and EMMCD images in software, applying any scaling or translation necessary for the images of the beads to overlay perfectly. Rotate the EMCCD slightly, if necessary. Focus on the central region of the field of view, ignoring any slight misalignments in the peripheral regions.

3.7 Optical Tweezers Alignment

These procedures comprise a systematic, reproducible method for properly aligning the trapping and detection beams. This procedure is typically done once at the beginning of a series of experiments. After initial adjustment, for a trap that is in frequent use, adjustment on subsequent days typically requires only minute corrections, and in practice, the coarse adjustment can often be skipped. During these procedures it is useful to recall the simple optical diagrams in Fig. 9, which demonstrate the consequences of tilting vs. translating

the trapping beam entering the objective lens. Refer to Fig. 3 regarding the location of optical components in the pathway.

The following steps coarsely align the trapping and detection lasers:

1. Prepare a sample slide chamber as described in Nicholas et al. (Chap. 9), but using a clean cover slip (non-aminosilanized). Fill with 1 mg/mL of β-casein in BRB80, and incubate 1 min to block the cover slip surface. Dilute trapping beads ~1:1,000 in 30 μL of the 1 mg/mL β-casein solution. Flow the bead suspension into the chamber and seal it with vacuum grease.
2. Trap a bead. Raise the nanopositioning stage to bring the cover slip into contact with the bead, and continue raising it until the bead starts to be pushed out of the trap (the bead will start to appear white).
3. Turn off the LED and increase the exposure time on the CCD. Remove filter BPF2 in order to view the retro-reflected trapping beam on the CCD (Fig. 10; *see* **Note 52**). Adjust the focus, if needed, in order to view the cross shape clearly at the center of the beam.
4. Zoom in to the center of the pattern on the image display. If the focal spot is not already centered on the marked position of the trap center, move it there using the AOD, and save this position as the new AOD center position ($A_{x,0}$ and $A_{y,0}$ in Subheading 3.6, **step 12**).
5. Zoom out on the image display so that the whole pattern is visible, and observe whether it is symmetrical. It is useful to move the nanopositioning stage up and down while observing the pattern (Fig. 10b). If the pattern is not symmetrical, use mirror Pzt-M1 to correct this.
6. After **step 5**, the center position of the pattern may have shifted slightly. If so, repeat **steps 4** and **5** until the trapping beam pattern is centered and symmetrical (Fig. 10c). The step size of the movements will need to be decreased as the target position is approached.
7. Close shutter S1 to block the trapping beam. Open shutter S2 and move filter ND out of the path to increase the detection beam power.
8. Observe the center position and symmetry of the detection beam. Use mirrors Pzt-M2 and Pzt-M3 to correct the center position and symmetry of the pattern as done for the trapping beam. Begin by using mirror Pzt-M2 to adjust the symmetry of the pattern (important: *see* **Note 53**), and then use Pzt-M3 to center the pattern. Repeat this process iteratively until the detection beam is centered and symmetrical (Fig. 10d). The trapping and detection beams should now be fairly precisely overlapped (Fig. 10e).

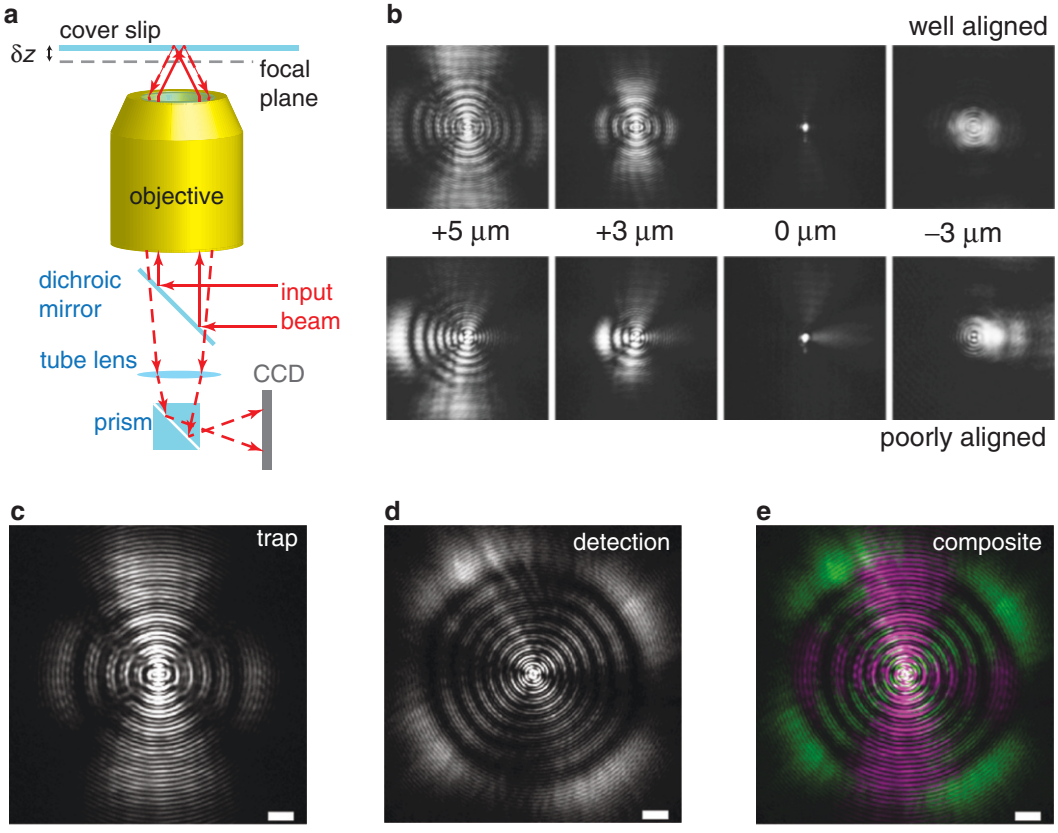

Fig. 10 Coarse alignment using the retroreflected trapping and detection beams. (**a**) Diagram of retroreflected beam detection. The input beam (trapping or detection, *solid rays* in the diagram) reflects off a dichroic mirror with high reflectivity at the laser wavelength and passes through the microscope objective lens to be focused on the cover slip. When the focused beam strikes the interface between the cover slip and the aqueous solution of the sample chamber, a small proportion of the intensity is reflected back into the objective, traveling a reverse path through the system (*dashed rays*). Despite the high reflectivity of the dichroic mirror, a small fraction of this light is transmitted to the imaging optics to form an intensity pattern on the CCD. The size and shape of the pattern depend on the distance δz between the glass–solution interface and the focal plane of the objective (δz is negative when the focal plane is below the interface). (**b**) Images of the retroreflected trapping beam intensity pattern for various values of δz (adjusted by moving the nanopositioning stage holding the slide chamber), for well-aligned (*top row*) and poorly aligned (*bottom row*) beams. The well-aligned beam passes directly through the center of the objective, parallel with the longitudinal axis of the lens (optical axis), forming a symmetrical pattern at each stage position. The poorly aligned beam, which may be displaced, tilted, or both relative to the well aligned beam, forms an asymmetrical pattern that changes (and may shift position in the image) depending on δz. Note that when $\delta z = 0$ (near perfect focusing on the glass–solution interface), both patterns look very similar, and it is only when the beams are "defocused" that the differences become apparent. After proper alignment of the (**c**) trapping beam and (**d**) detection beam, the two patterns appear much more symmetrical and are concentric with each other (**e**, composite image: detection beam pseudocolored *green*, and trapping beam *magenta*). Scale bars in (**c**–**e**) are 2.25 μm

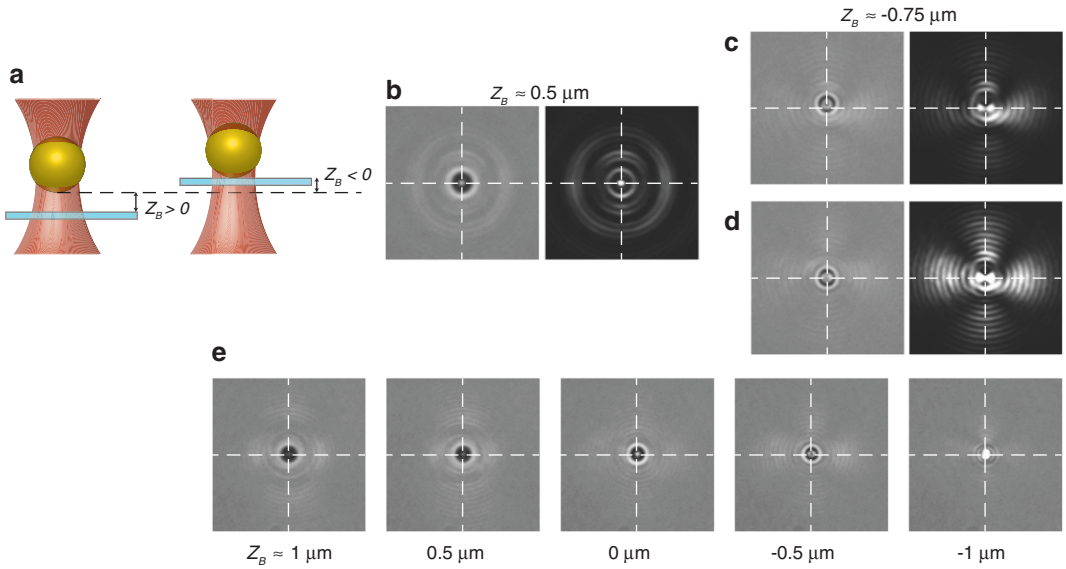

Fig. 11 Refinement of trapping beam alignment. (**a**) The trap holds the microsphere above the cover slip with a distance Z_B between the glass and the surface of the microsphere (*left*, not to scale; Z_B is measured as the axial stage position minus the height of the bottom surface of the bead at its normal trapped position). As the nanopositioning stage moves the cover slip upward, the magnitude of Z_B progressively decreases. Once the cover slip moves high enough, it displaces the bead axially from its equilibrium trapped position (*right*, at this point, Z_B is negative). (**b**) Following coarse adjustment using retroreflections, with $Z_B \approx 0.5$ µm, the microsphere is well centered, and the reflected laser light forms a fairly symmetrical concentric pattern around it (*left*). With the bright-field illumination turned off and the CCD gain increased, it is easier to view the reflected light (*right*). (**c**) After moving the stage upward ($Z_B \approx -0.75$ µm), the microsphere position deviates laterally (*left*) and the reflected light pattern is asymmetrical and off-center (*right*), indicating a slight misalignment of the laser beam. (**d**) After readjustment, the microsphere is centered (left) and the reflection pattern is more symmetrical and centered. (**e**) Following multiple rounds of minor adjustments, the microsphere remains well centered and the retroreflection symmetrical, over a wide range of stage displacements

The following steps refine the alignment of the trapping beam:

9. Close shutter S2. Turn the LED on and adjust the CCD exposure for bright-field imaging. Focus on the beads near the cover slip surface and trap one. Turn down the LED power until the laser back-reflection off the bead becomes visible (with the bead still visible in bright field, Fig. 11b). By turning the LED off momentarily, this back-reflection will appear clearer (Fig. 11b). If the preceding adjustment was done correctly, it will appear quite symmetrical (*see* **Note 54**).
10. Move the stage up (+*z* direction) slowly, approximately 0.75 µm past the position at which the bead begins to appear bright (Fig. 11a). The bead will likely be displaced radially (Fig. 11c), and the back-reflection will become asymmetrical, with intensity concentrated on one side of the bead.

11. Use mirror Pzt-M1 to adjust the beam so that the back-reflection becomes symmetrical again, and the bead returns to the trap center position (Fig. 11d). Adjust in small increments (*see* **Note 55**). It is useful to switch the LED off periodically to examine the back-reflection more carefully.
12. Move the nonpositioning stage upward by 50–100 nm, and repeat **step 11**. If no adjustment is needed, move an additional 50–100 nm upward.
13. Move the cover slip away from the bead so it is not in contact anymore, and observe the bead position (the adjustments using Pzt-M1 may have small unintended effects on the position). If it is no longer centered at the trap center marked on the CCD, move it back to the center using the AOD, and save the new center positions. Repeat this 2–3 times. When finished, the bead should remain centered with a symmetrical back-reflection, even when the stage presses against it and displaces it axially from the trap center (Fig. 11e).
14. Replace filter BPF2.

The following steps refine the alignment of the detection beam, using back focal plane (BFP) detection signals calculated from the QPD voltages. Figure 12 presents BFP detection and the associated equations for the QPD x and y normalized voltage signals:

15. Close shutters S1 and S2, and completely block the QPD from the light. Set the acquisition frequency for the QPD data to 3 kHz and the low-pass filter frequency to 1.5 kHz. For each preamplifier (preamp) gain setting on the low-pass filters, acquire a few seconds of data, take the average for each quadrant, and save these values in the software as offsets to be subtracted automatically from the corresponding quadrant when using the specified preamp gain (*see* **Note 56**).
16. Repeat **step 15** for 65,536-Hz sampling rate (and any other sampling rates to be used).
17. Open shutter S2, close shutter S1, and remove filter ND. Set the preamp gain on the filters to 0 dB. Trap a bead using the detection laser. If it is not aligned with the marked center position, adjust its position using mirror Pzt-M3. Alternate between trapping with the trapping beam and the detection mean during the adjustment. Adjust Pzt-M3 so that the bead stays in essentially the same position by eye when switching between the two lasers.

Steps 18 and **19** *can often be skipped if the instrument is already in fairly good alignment:*

18. Close both shutters S1 and S2. Adjust the QPD positioner and the QPD relay lens (RL) to positions near the center of their ranges. Move the cover slip well above the focal plane of the

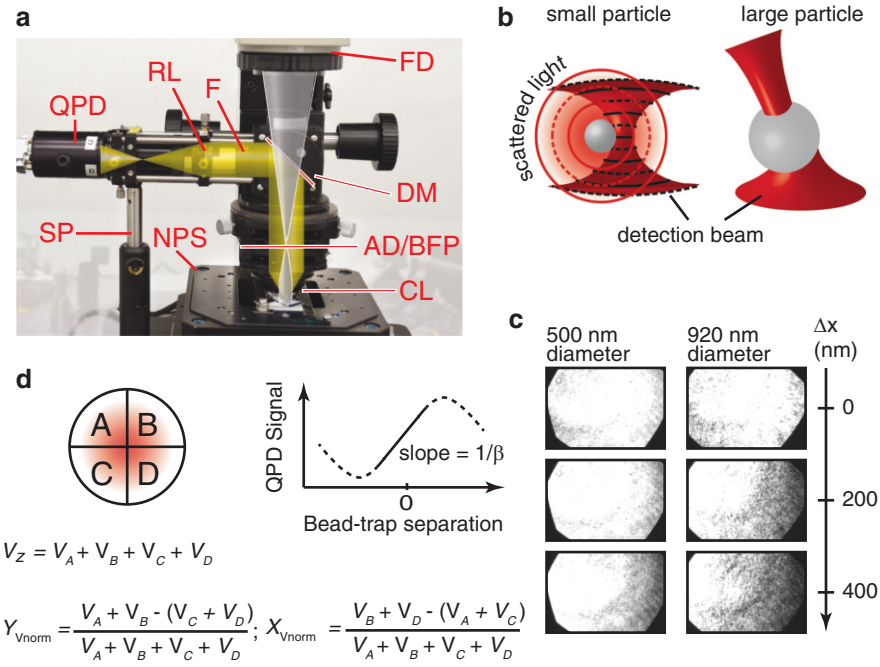

Fig. 12 Back focal plane detection of microsphere position. (**a**) Optical configuration for back focal plane detection. The bright-field illumination (*gray*, exiting the field diaphragm (FD) from above) and detection beam (*yellow*) propagate in opposite directions through the system. After exiting the objective lens on the inverted microscope, the detection beam enters the slide chamber fixed to the nanopositioning stage (NPS), interacts with the trapped microsphere, and is collected by the condenser lens (CL), which is confocal with the objective. The detection beam is then redirected toward the quadrant photodiode (QPD) detector by a short-pass dichroic mirror (DM) that reflects the 830-nm detection beam, but transmits the 470-nm bright-field illumination. The trapping beam, which follows the same path, is blocked by an 830-nm band-pass filter (F). The relay lens (RL) is positioned such that it images the aperture diaphragm/back focal plane (AD/BFP) of the condenser lens onto the QPD (in this case, the lens is placed three focal lengths from the AD/BFP and 1.5 focal lengths from the QPD, respectively, to achieve a magnification of ½). A support post (SP) with vibration-dampening foam on top helps stabilize the QPD detection arm and eliminate unwanted movements. (**b**) The nature of the interaction of the detection beam with the bead depends somewhat on its size. Very small (<1 μm) particles act as scattering point sources. In this case, the pattern in the back focal plane arises due to interference between the unscattered portion of the detection beam (which essentially propagates without interacting with the particle) and the light scattered by the particle (*left*, *solid* and *dashed lines* represent optical wave fronts). Larger particles may significantly alter the path of the detection beam via refraction of the light as it passes through the microsphere (*right*), causing the entire pattern in the back focal plane to shift. (**c**) Examples of the patterns observed by replacing the QPD with a CCD camera. The dark regions with sharp edges in each corner are images of the aperture diaphragm (located at the back focal plane of the condenser and visible here because it has been partially closed). The *left* and *right* columns correspond to 500- and 920-nm-diameter beads, respectively. Approximate bead–trap separations for each set of images are given on the right side. Note that the larger particle has a more pronounced effect on the overall beam position. (**d**) The voltage signals from the four quadrants of the QPD (labeled V_A, V_B, V_C, and V_D, respectively) are used to calculate response signals in three dimensions (normalized by the total voltage for the *x* and *y* directions). The response signals each have similar shapes and are linear with displacement near the center of the detection beam (solid black line, slope = $1/\beta$). In this region, the QPD response X_{Vnorm} can be directly converted to displacement $\Delta X = \beta_x X_{Vnorm}$ (and identically for ΔY)

objective, and open S1 so that the trapping beam scatters microspheres away from the optical axis (this minimizes fluctuations in the QPD signals).

19. Open shutter S2. Adjust lens RL so that both the *x* and *y* signals ($V_{\text{norm},x}$ and $V_{\text{norm},y}$, respectively) are zero. This centers the detection beam on the QPD.
20. Close shutter S1. Move the stage back downward so the beads come into focus and trap one with the detection laser. Adjust the position of the QPD so that $V_{\text{norm},x}$ and $V_{\text{norm},y}$ fluctuate around zero (often no adjustment is needed at this step).
21. Reinsert filter ND to reduce the power of the detection beam. Open shutter S1 and trap a bead within roughly 50–100 nm of the cover slip surface. Observe the normalized QPD signals and use mirror Pzt-M3 to center them at zero (*see* **Note 57**).
22. Using the AOD, sweep the trapped bead in a triangle-wave pattern along the *x* axis with amplitude ~1.2 μm peak-to-peak (i.e., ±600 nm) and a period of ~2 s (Fig. 13).
23. Observe the QPD response signals, focusing on the axis along which the bead is moving. The objective is to make this response symmetrical and centered about the origin (Fig. 13b, panel 4). For our instrument, this corresponds to a maximum deflection of ±0.4 V_{norm} in each channel (*see* **Note 58**). Start by using Pzt-M3 to move the overall signal in the direction required to center it about zero (Fig. 13b, panel 2). This will significantly perturb the symmetry of the response waveform, which is then reestablished using Pzt-M2 (Fig. 13b, panel 3), moving it in the same direction as Pzt-M3 (up, down, right, or left buttons, configured as described in **Note 53**). Repeat this process until the response waveform is symmetrical and centered at zero (Fig. 13b, panel 4).
24. Stop the sweeping of the bead, and re-zero both QPD signals using Pzt-M3.
25. Repeat steps **22**–**24** for the *y* axis. Adjustments to one axis may initially perturb the response in the other axis. Iterate between the two axes until the response in both axes is symmetrical and zero centered.
26. During the early rounds of iterating **steps 22**–**24** for the two axes, there may be considerable "crosstalk" between the *x* and *y* QPD signals (displacements in the signal of the non-sweeping axis correlated with the displacements in the sweeping axis). After multiple rounds of adjustment, the crosstalk should be negligible. If not, it may be symptomatic of an improperly rotated QPD (*see* Fig. 14 *and associated legend*). Correct this by sweeping the bead along one of the axes and carefully rotating the QPD around the optical axis until the crosstalk is minimized.

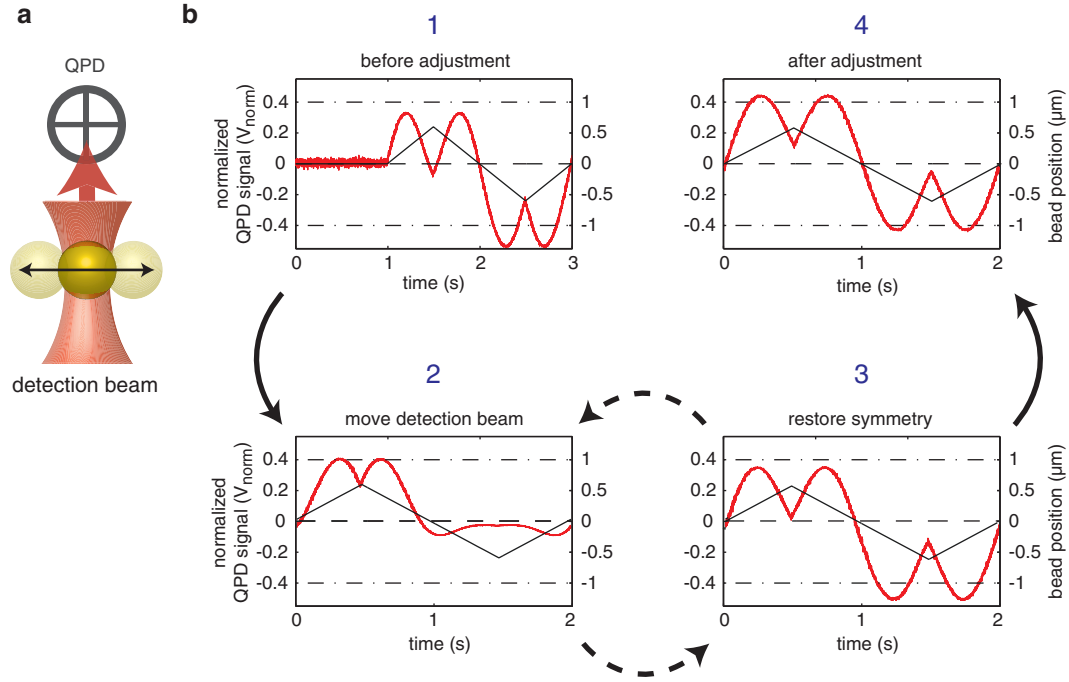

Fig. 13 Alignment of the trapping and detection beams by sweeping the trapping beam in a triangle-wave pattern. (**a**) A trapped bead is swept transversely across the detection beam (along either the *x* or *y* axis) by using the AOD to move the trap position in a triangle-wave pattern. This modulates the normalized QPD position signals, $X_{V\text{norm}}$ and $Y_{V\text{norm}}$. The objective of adjustment is to position the detection beam so that the response in each channel is symmetrical about the origin. (**b**) After coarse alignment of the trap and detection beams, the QPD position signal (*red* trace, V_{norm}) for each channel is very nearly zero. However, when the trap position is modulated in a triangle-wave pattern (*solid black line*), it is clear that the response is not symmetrical about the origin (but rather around another position, in this case one slightly negative), indicating the detection beam and trapping beam do not overlap (step 1, the *dashed lines* through 0 V_{norm} and ±0.4 V_{norm} can be used as landmarks to help guide the eye). The center position of the sweep pattern is moved toward the origin using mirror M1 (*see* Fig. 3), with the consequence that the symmetry of the response is lost (step 2). Adjusting M2 restores the symmetry, while reversing some of the movement toward the origin (step 3). However, the net result is that the response is symmetrical and that the center of the pattern is closer to the origin. Performing steps 2 and 3 repeatedly yields the desired response (step 4). This process is repeated iteratively for each channel, until both exhibit symmetrical responses centered at the origin

3.8 Optical Tweezers Calibration

BFP detection (Fig. 12) [57–61] measures the separation between the detection beam and a trapped bead to within nanometers at a rate of many kilohertz. If the spring constant for the trap is known, these displacements are converted easily into forces. Thus, two calibrations must be performed: one to characterize the QPD detector response to bead displacements ("position calibration") and another to determine the spring constant ("force calibration"). Both calibrations involve measurements of microsphere displacements, either known displacements induced by the experimenter or natural fluctuations due to Brownian motion. Several types of calibration should be done when the optical trap is initially

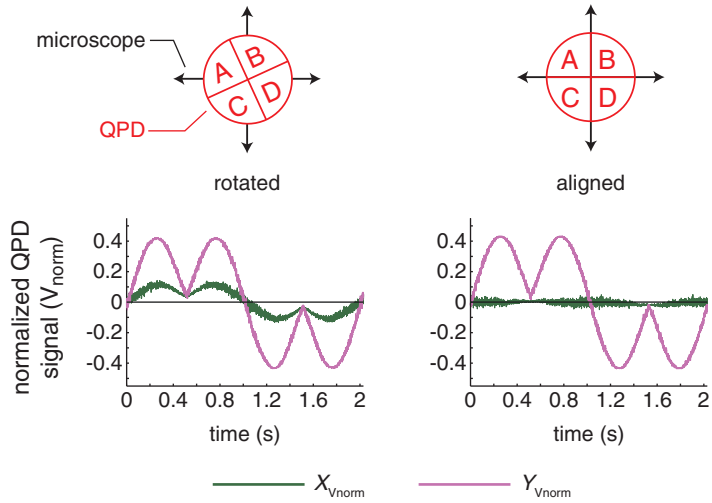

Fig. 14 Identification and correction of erroneous QPD rotation. After aligning the instrument as precisely as possible, when the trap sweeps a bead back and forth across the detection beam in the in one axis (*y* in this example), the QPD signal (X_{Vnorm}) for the non-sweeping axis exhibits substantial displacements if the QPD is rotated relative to the axes of the microscope (*left*). This example is exaggerated for clarity, and in practice, the "crosstalk" between channels is usually much subtler. Correcting the QPD rotation decreases excursion in the non-sweeping axis, and when the axes are aligned (*right*), the signal for the non-sweeping axis is virtually unaffected even by large displacements in the orthogonal direction. For counterclockwise (as judged when looking toward the face of the QPD detector) rotations relative to the microscope axes, *y* sweeping produces deflections of the same sign in X_{Vnorm} and Y_{Vnorm} (as shown in the figure), whereas *x* sweeping produces deflections of the opposite sign in X_{Vnorm} and Y_{Vnorm}. For clockwise rotations, the situation is reversed

constructed and checked for a reasonable degree of consistency before conducting experiments. Detailed, automated calibration analysis should also be integrated into the trap control software, since it can be very useful in assessing instrument performance during daily use and when diagnosing problems.

Because both force and position calibrations depend on the separation between the bead and the cover slip (see below), the first step is to determine the bead–cover slip distance. This is done by moving the nanopositioning stage in the axial (*z*) direction, finding the point of bead–cover slip contact (Fig. 15), and correcting the measured distance for the effective focal shift [62, 63] (Fig. 16).

For position calibration, the most straightforward method is to simply sweep the bead across the detection beam focus in known increments (Fig. 17), by either steering the trap or, with the nanopositioning stage, using a bead stuck to the cover slip

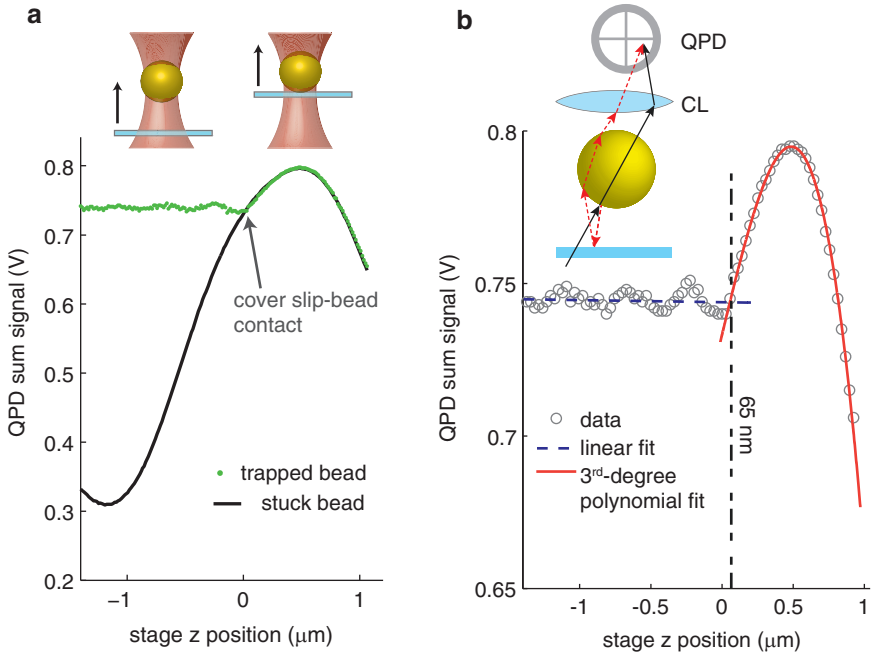

Fig. 15 Determination of bead–cover slip separation. (**a**) The stage is swept over a ±1,200 nm range in the axial (*z*) direction. First, a bead strongly stuck to the cover slip is carefully centered on the detection beam so that the *x* and *y* QPD signals are zero. Sweeping the bead through the trapping beam induces the characteristic response in the QPD sum signal (*solid black line*). If the same experiment is performed with a trapped bead (*green dots*), essentially no response is produced until the cover slip makes contact with the bead surface and pushes it out of the trap (at which point it follows the same trajectory and induces the same QPD signal as the stuck bead). Note that while the position (in nm) at which the contact point occurs depends on the distance between the cover slip and bead, the QPD voltage at which this happens depends on the position of the detection beam focus relative to the trapped bead (i.e., the trapping beam focus). In this example, the focus of the detection beam is slightly below the trapped bead, since the two curves overlap beyond the central voltage value for the stuck bead. (**b**) To find the bead–cover slip separation during an experiment, the position of the inflection point (where the sum signal for the trapped bead turns upward and follows the path of the signal for the stuck bead) is determined by finding the intersection of a line fit to the initial segment and a third-order polynomial fit to the peak, in this case 65 nm. Note that this value must be corrected to account for the focal shift (*see* Fig. 16), so that the true initial separation was actually ~0.82 × 65 = 53 nm. The periodic modulation observed in the sum signal as the cover slip comes very close to the bead is expected behavior and arises because the surfaces of the bead and cover slip essentially form a miniature Fabry–Pérot interferometer [62], as shown in the inset. Light backscattered/reflected from the bead (*red dashed rays*) reflects off the cover slip and interferes with forward-propagating (unscattered/forward-scattered) light (*solid black rays*) at the detector. The constructive/destructive nature of the interaction depends on the bead–cover slip distance and oscillates with a spatial frequency dependent on the wavelength of the detection beam

(*see* **Note 14**). In the central region (±~100 nm), the calculated QPD response signals ($X_{V\text{norm}}$ and $Y_{V\text{norm}}$) are linear with bead displacement and may be converted to physical positions by multiplying with the inverse slope: $x = X_{\text{nm}} = \beta_x X_{V\text{norm}}$ (*see also* Fig. 12). Beyond this central region, the response function is nonlinear, but the useful range can be extended to the entire region for which the

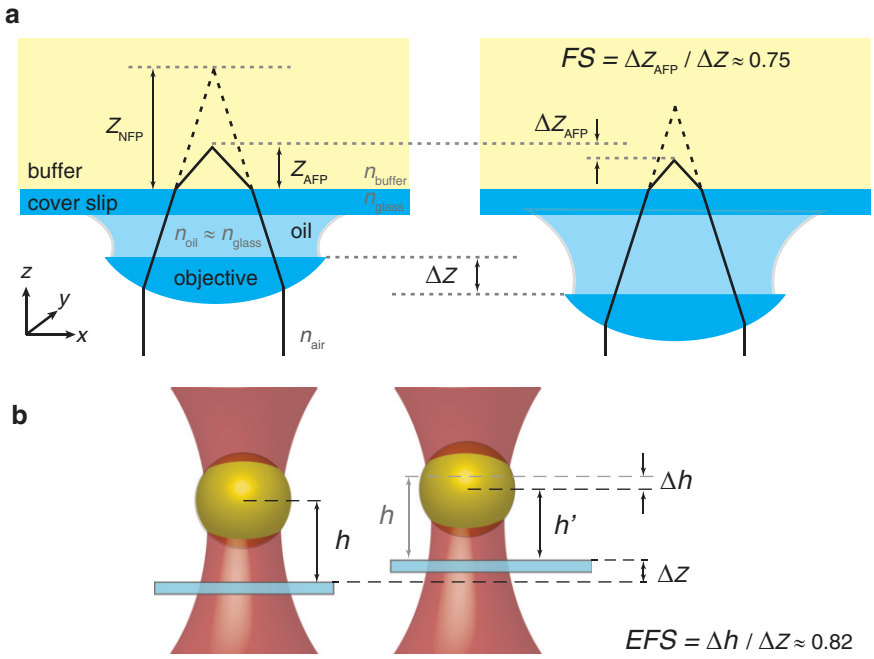

Fig. 16 The focal shift and its effects on bead–cover slip separation. (**a**) Ray diagram for a collimated beam focused by an oil immersion microscope objective. Although the indices of refraction are closely matched between the objective, immersion oil, and cover slip ($n_{oil} \approx n_{glass} \approx 1.51$), the refractive index of the sample buffer is significantly smaller ($n_{buffer} \approx n_{water} = 1.33$). This causes the rays to refract at the interface, bringing the actual focus position (Z_{AFP}, measured relative to the cover slip surface) closer to the objective than the nominal focus position (Z_{NFP}) expected if the refractive indices were equal (dashed rays). Z_{AFP} depends on the indices of refraction and on the distance the beam travels in each medium (glass/oil vs. buffer), which is determined by the separation between the cover slip and objective. A change ΔZ in this separation (due to movement of the objective or cover slip) induces a corresponding change ΔZ_{AFP} in the actual focus position, which is linear with ΔZ over several micrometers. The proportionality constant relating ΔZ_{AFP} to ΔZ is referred to as the focal shift, *FS* (which is defined differently by some authors, as the difference $[Z_{NFP} - Z_{AFP}]$). Using high-NA oil-immersion objectives and aqueous buffer, a full electromagnetic treatment of the problem gives $FS \approx 0.75$. (**b**) In optical tweezers, the figure of interest is not the focal shift per se, but rather the effective focal shift (*EFS*), defined analogously, though in reference to the trapped bead position, *h*, rather than to the focus itself. $EFS \approx 0.82$ is slightly greater than *FS* for aqueous solutions, but still significantly different from unity. This must be accounted for when moving the objective or the nanopositioning stage holding the cover slip in the axial direction. Moving the stage toward the trapped bead by 100 nm decreases the separation not by 100 nm, but rather by ~82 nm. Truly reducing the bead–cover slip separation by 100 nm requires moving the stage by ~122 nm instead

response function is single-valued by fitting it with a third-degree polynomial, rather than a line (Fig. 17; *see* **Note 59**). Some less direct methods employing spectral analysis (see below) or rapid sweeping of the AOD [64] have also been used (*see* **Note 60**).

Force calibration is usually done after position calibration, either by analyzing the Brownian motion of a trapped bead or by applying a known force to the bead and measuring how far it is displaced from the trap center as a result. The simplest method is

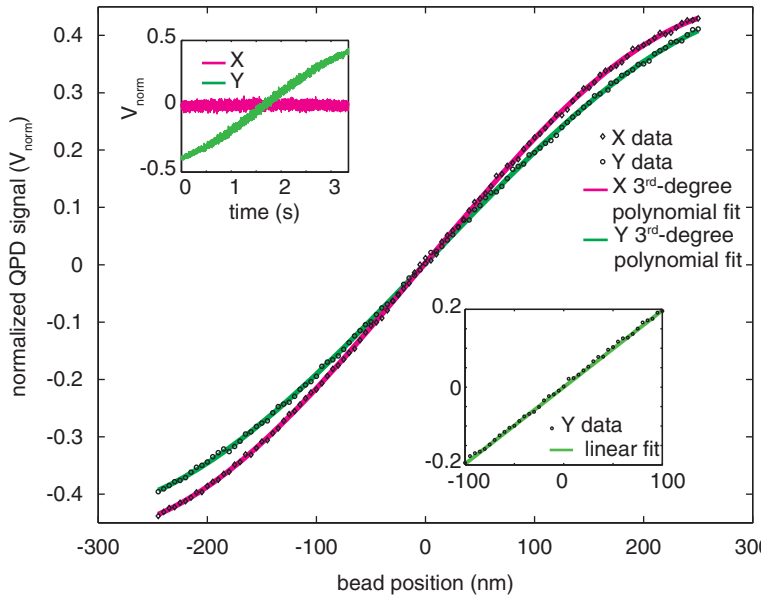

Fig. 17 QPD position calibration. The trap is used to step a bead across the detection beam separately in each axis by a known distance, in this case ±250 nm (the inset in the *upper left* shows the sweep in the *y* axis). For the central region (approximately ±100 nm), the response is linear (the *lower right inset* shows this region for the *y* axis), but exhibits curvature for larger displacements (*see* Fig. 13). At each step (every 5 nm in this example), many samples of the QPD response signal are recorded and averaged (weaker traps require more samples because the bead is less confined; in this example, with $k \approx 0.06$ pN/nm, 100 samples were averaged at each point). These values are then plotted against the position and fit with a third-degree polynomial. The coefficients from this fit are then used to determine the bead position from the QPD signal during experiments

equipartition analysis (Fig. 18a and c), in which the spring constant is calculated as $k_x = k_B T / \langle x^2 \rangle$ (and similarly for k_y) [26], where k_B is the Boltzmann constant, T is the absolute temperature (in Kelvin), and $\langle x^2 \rangle$ is the variance of the distribution of bead positions over time (*see* **Note 61**). The advantage of this method is that essentially no specific information about the system (e.g., bead size, solution viscosity, distance of the bead from the cover slip) is required, and it is very easy to compute k. However, the value of the variance is inflated by any drift or other artifacts (e.g., electronic noise) in the optics or detection system (since the variance depends on the square of the displacement, even if artifacts average to zero, they increase the computed value). Therefore, the equipartition method tends to underestimate k.

A related method for force calibration, also employing a statistical mechanical analysis of trapped microsphere fluctuations, directly computes the trapping potential $U(x)$ [65]. From the Boltzmann law, $P(x) = \exp(-U(x)/k_B T)/Z_p$ (*see* **Note 61** for

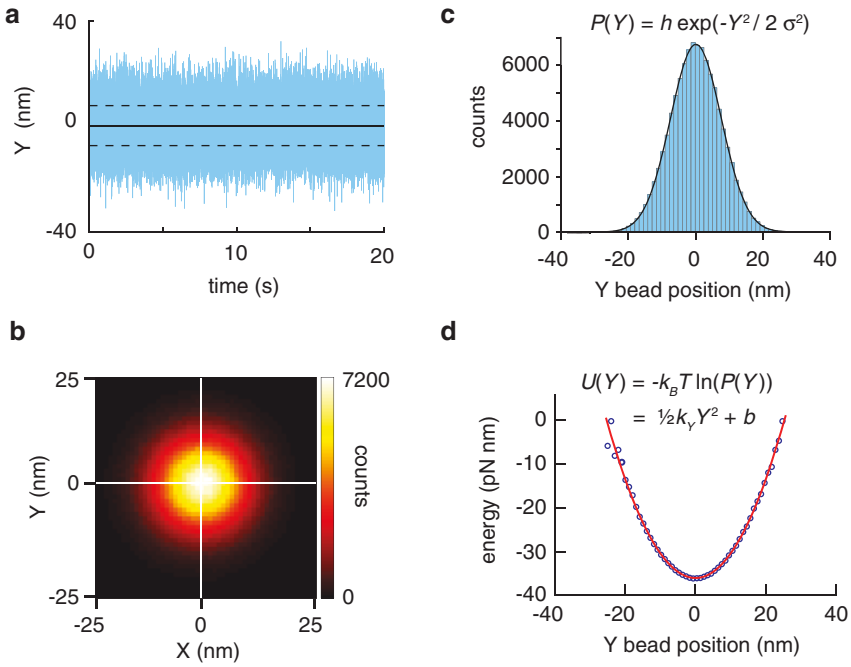

Fig. 18 Mapping of bead diffusion and determination of the trap spring constant. (**a**) *Y* position trace for a trapped bead over a period of 20 s (*dashed lines* are ±standard deviation, $\sigma = 7.6$ nm). The variance of the positions is $\sigma^2 = 57.4$ nm^2, which for a value of $k_B T = 4.116$ pN nm ($T = 25$ °C) yields $k_y = 0.072$ pN/nm by the equipartition method. (**b**) For the same experiment as in (**a**), plotting a two-dimensional histogram of bead positions provides a useful method for determining the shape of the trapping potential (limited to the central region in which the bead can diffuse) and identifying any irregularities or asymmetries. (**c**) The data from (**a**) are plotted in a histogram (50 equally spaced bins of ~1.3 nm width) and fit with a Gaussian function $P(Y)$, also yielding $\sigma = 7.6$ nm (agreement between σ calculated "blind" and by fitting shows that the data are Gaussian distributed and do not require fitting to determine σ). (**d**) Given the (non-normalized) probability distribution in (**c**), it is possible to calculate the potential $U(Y)$, which, assuming a harmonic potential, can be fit by the parabola $\frac{1}{2}k_y Y^2 + b$, where b is a constant. This procedure yields $k_y = 0.071$ pN/nm, in good agreement with the equipartition method. The good fit of the parabola to the calculated potential shows that the trap potential is indeed harmonic (like a Hookean spring) near the center

symbol definitions). We can compute the potential as $U(x) = -k_B T \ln(P(x)\ Z_p) = -k_B T \ln(P(x)) - k_B T \ln(Z_p)$, where the last term is a constant offset that is ignored. $P(x)\ Z_p$ is simply the (non-normalized) histogram of position fluctuations of the trapped microsphere (Fig. 18c). Assuming that $U(x) = \frac{1}{2}k_x x^2 + b$ (where b is a constant offset), this model can be fit to the potential calculated from the histogram in order to find k_x (Fig. 18d). This method has the added benefit of creating a map of the trapping potential, even if it is not in fact harmonic. However, only a fairly limited range near the trap center is mapped, and like the equipartition method, this analysis can be hindered by unwanted noise sources.

Spectral analysis offers a useful alternative to statistical analysis (Gittes and Schmidt [66] provide a very accessible introduction),

whereby the Fourier transform is used to evaluate the power spectral density $S(f)$ of the bead motion (*see* **Note 62**), where f is frequency. Considering the thermal motion of the bead in the trap as that of a damped harmonic oscillator driven by a (random) Langevin force [67], the power spectral density takes the form of a Lorentzian, $S_{xx}(f) = k_B T/[\pi^2\gamma\ (f_c^2 + f^2)]$, where γ is the hydrodynamic drag for the bead, and the "corner" or "roll-off" frequency is $f_c = k/2\pi\gamma$ (frequency at which the power spectral density reaches half the maximum value of $4\gamma k_B T/k^2$). Thus, by computing the power spectral density and fitting this function with a Lorentzian, the spring constant can be determined from the corner frequency found by the fit (Fig. 19a), i.e., $k = 2\pi\gamma f_c$ (*see* **Note 63**).

The power spectral density can also be used for position calibration. It can be shown [26, 58, 68] that the product $S_{xx}(f)\ f^2$ asymptotically approaches the limit $C = k_B T/\pi^2\gamma$ for $f >> f_c$ (Fig. 19c). Assuming a linear conversion β_x between detector response (V_{norm}) and displacement (nm), then $S_{xx}(f) = \beta_x^2 S_{VV}(f)$, and $\beta_x = S_{xx}(f)\ f^2/S_{VxVx}(f)\ f^2 = [k_B T/(\pi^2\gamma\ S_{VxVx}(f))]^{1/2}$ for $f >> f_c$. Alternatively, if β_x is known, this method can be used to determine γ, i.e., $\gamma = k_B T/(\pi^2\beta_x^2\ S_{VxVx}(f))$.

Force calibration via power spectral density analysis has the advantage that low-frequency drift and other noise sources are easily visible in the spectrum and can be disregarded during the fitting procedure. It is complicated, however, by the need to know γ. In bulk solution, for a sphere of diameter d, the drag coefficient is $\gamma = 3\pi d\eta$, where η is the viscosity of the solution. There is usually some degree of uncertainty in the bead diameter, and η depends on the composition of the solution and the temperature. More importantly, γ is strongly influenced by the proximity of the bead to the cover slip surface, according to Faxén's law (Fig. 19d) [67], $\gamma/\gamma_0 = \gamma_0/[1 - 9/16R + 1/8R^3 - 45/256R^4 - 1/16R^5]$. Here, γ_0 is the drag in bulk solution ($3\pi d\eta$), $R = d/(d + 2Z_B)$, and Z_B is the distance from the surface of the cover slip to the surface of the bead (*see* **Note 64**). The value used for γ must therefore be scaled according to the bead-surface separation. Our approach is to estimate γ from the power spectrum (Fig. 19c, and see above) and also by directly measuring the bead–cover slip separation (Figs. 15 and 16) and computing γ via Faxén's law. We then use these values as initial guesses in the Lorentzian fit to the power spectral density and fit with both γ and f_c as free parameters (Fig. 19a).

A more conceptually straightforward method for force calibration relies on Stokes's law for the viscous drag force exerted on a sphere subjected to continuous fluid flow. In this method, fluid flow past the trapped microsphere is created by moving the slide chamber with the nanopositioning stage. The drag force on the bead is $F_{drag} = \gamma v_{stage}$, where v_{stage} is the velocity at which the stage moves (Fig. 20a; *see* **Note 65**). This force displaces the bead by a distance $\gamma v_{stage}/k$ from the trap center. Thus, assuming v_{stage} and γ are known, k may be calculated directly from the observed

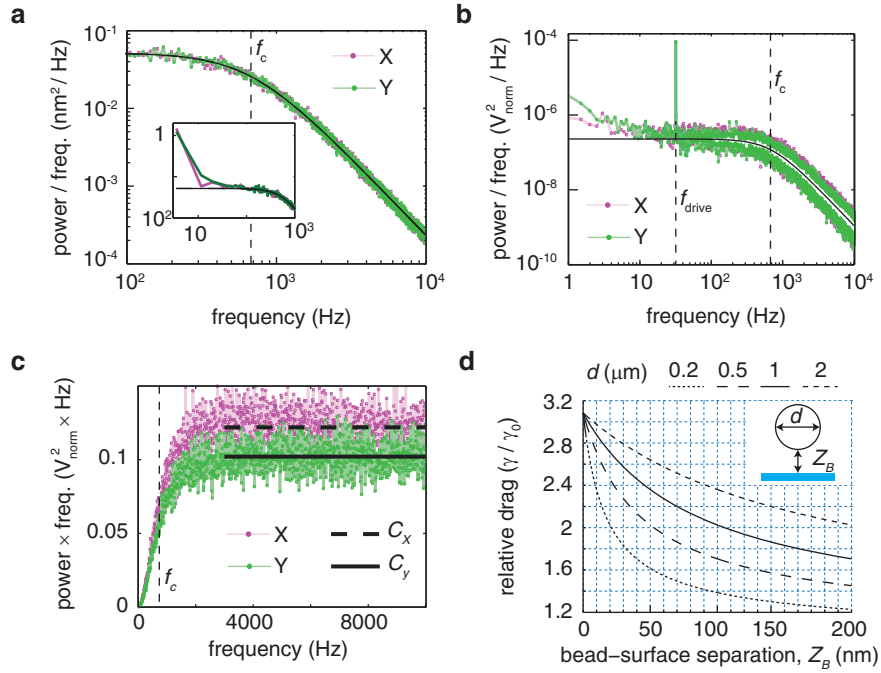

Fig. 19 Power spectrum analysis for optical trap calibration. For (**a**–**c**) the separation Z_B between the bead and cover slip is ~70 nm, and the sample rate for the data is 65,536 Hz (2^{16} Hz). (**a**) Log–log plot of the *x* and *y* power spectral densities for a trapped bead, with Lorentzian fit to the frequencies above 100 Hz (*x*, *dashed line*; *y*, *solid line*; note that the *x* power spectrum and dashed-line fit are only partially visible because they almost exactly overlap the *y* spectrum). The inset shows the entire spectrum, which exhibits non-Lorentzian character at very low frequencies (this is attributable to slow, long-term drift and is minimized by enclosing the optical pathway and otherwise stabilizing the instrument). The parameters extracted from the fit (for *x* and *y*, respectively) are corner frequencies (f_c) 683 and 685 Hz and effective drag coefficients $2.23 \times \gamma_{water}$ and $2.22 \times \gamma_{water}$, yielding spring constants $k_x = k_y = 0.074$ pN/nm (compared to $k_x = 0.074$ pN/nm and $k_y = 0.072$ pN/nm calculated by the equipartition method). (**b**) Power spectrum analysis for forced oscillations (sinusoidal nanopositioning stage movement at $f_{drive} = 32$ Hz) of the same bead as in (**a**). In this example, the stage oscillates in the *y* direction with 98 nm measured amplitude (*see* **Note 75**), giving rise to a sharp peak at f_{drive} only in the *y* channel (note that the spatial units here are V^2_{norm} rather than nm^2). The amplitude of this peak is used to calculate β (the V_{norm}-to-nm conversion factor for the linear region of the QPD response signal). A Lorentzian fit (*black line*) to the block-averaged *y* data above 100 Hz (*white trace*) yields $f_c = 696$ Hz, $\beta_y = 474$ nm/V_{norm}, $\gamma_y = 2.22 \times \gamma_{water}$, and $k_y = 0.073$ pN/nm, in very good agreement with the standard power spectrum analysis in (**a**) and with the AOD-based QPD calibration ($\beta_y = 478$ nm/V_{norm}; not shown). The *x* and *y* power spectra apparently overlap somewhat less than in (a); however, this is attributable to the small difference in β between the two channels ($\beta_x = 434$ nm/V_{norm}), rather than a difference in physical motion. (**c**) For frequencies much greater than f_c, the product of frequency squared times the power spectral density approaches a constant value C, such that $\gamma = k_B T/[C\ (\pi\ \beta)^2]$. Thus, if γ is known, C can be used to find β and vice versa. Given β from the AOD-based calibration of the QPD response, we use this phenomenon to generate an initial guess for γ in our Lorentzian fits of the power spectra in (**a**) and (**b**). The data shown here (from the same underlying position data as the power spectrum in (**a**)) give $C_x = 0.122 V^2_{norm}$ Hz and $C_y = 0.102 V^2_{norm}$ Hz, yielding $\gamma_x = 2.31 \times \gamma_{water}$ and $\gamma_y = 2.22 \times \gamma_{water}$, in relatively good agreement with the values used in the final fit. (**d**) The drag γ experienced by a sphere in close proximity to a surface is significantly larger than that experienced in bulk solution, γ_0, and is approximated by Faxén's law. The ratio γ/γ_0 is plotted for different bead diameters as a function of the bead-surface–cover slip surface separation, Z_B

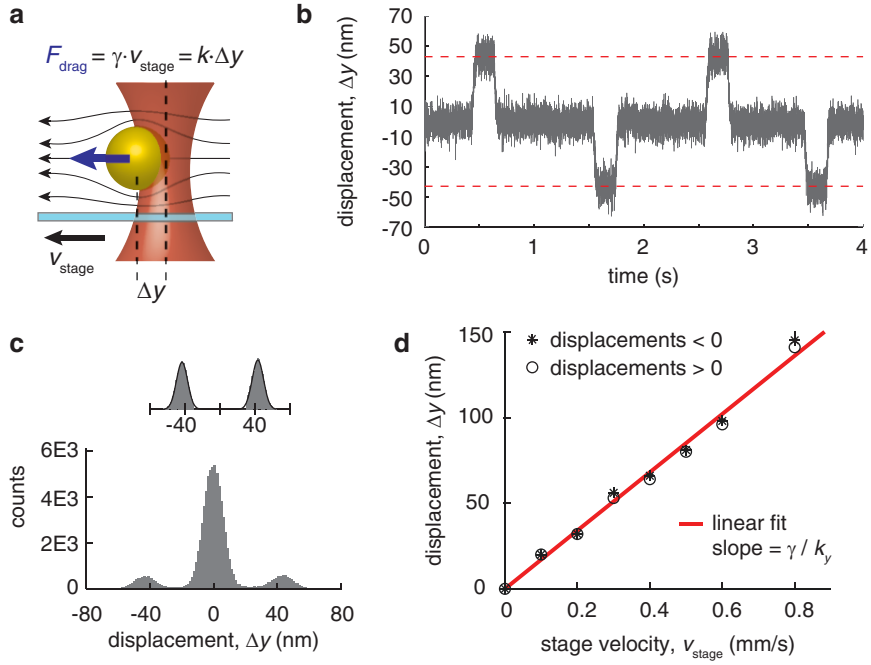

Fig. 20 Viscous drag determination of trap stiffness and mapping of trap potential. (**a**) With a bead in the trap, the stage is moved in the *y* direction at a constant velocity, v_{stage}. This pulls the solution in the chamber past the bead, thus inducing a viscous drag force γv_{stage} that pulls the bead away from the trap center and is balanced by the restoring force of the trap, $k_y \Delta y$. (**b**) Example data, showing bead displacements during constant-velocity stage movement, interspersed with periods of pausing. For this experiment, the 920-nm-diameter bead was approximately 500 nm above the cover slip, the stage velocity was 0.3 mm/s, and k_y was measured to be 0.076 pN/nm via equipartition and power spectrum, with $\gamma \approx 1.5\,\gamma_{water}$. The predicted Δy for these parameters is ~46 nm, in very good agreement with the 43 nm measured (*red dashed lines*; see (**c**)). (**c**) Measurement of Δy. The positions from the data in (**b**) are plotted in a histogram (100 equally spaced bins), with a major peak at 0 nm due to the pauses between movement. The inset shows fits to the two side peaks, with data from ±20 nm discarded, yielding means of ±43 nm. (**d**) Repeating these processes at many different velocities allows the mapping of the trapping potential in regions far from the center, in order to test the validity of trap linearity in these regions, and provides a more robust estimation for k_y as determined from the slope of a line fit to the data. During the course of the experiment, k_y was measured to be ~0.070 pN/nm on average (via equipartition and power spectrum), with $\gamma \approx 1.5\ \gamma_{water}$. The fit is consistent with a linear force–displacement relationship for displacements of at least 150 nm, and the calculated slope of 1.7×10^{-4} s yields $k_y = 0.068$ pN/nm, in reasonably good agreement with the standard methods

bead displacement. Moreover, the bead displacement should be linearly related to v_{stage}, with slope γ/k (Fig. 20d), allowing a more precise calculation of k than using a single value of v_{stage}. Any nonlinearity (e.g., at bead displacements more than 100–200 nm) indicates deviation from a harmonic potential. The ability of this technique to detect such nonlinearity and map the trapping potential over a wide range of displacements represents a major advantage compared to other techniques. However, similar to the power spectrum method, γ must be known precisely and is

likely to change as the stage is moved, since the cover slip surface is never perfectly perpendicular to the optical axis (*see* **Note 66**). Likewise, v_{stage} must be known to high precision, and measurements should only include data for which the stage has achieved a constant, steady velocity. This calibration method can also be cumbersome since it is relatively time-consuming, and multiple beads can often be accidentally caught in the trap as the stage moves over relatively long distances.

A "hybrid" method of calibration [63, 69] (Fig. 19b), combining the power spectrum and viscous drag analyses, allows simultaneous position and force calibration, without the need to know the drag coefficient (in fact, this method has been used to *measure* the drag coefficient and solution viscosity [63, 70]). During the data acquisition, the nanopositioning stage oscillates in a sinusoidal pattern with known amplitude and frequency, f_{drive}, adding a small (almost imperceptible) driven oscillation to the bead motion, in addition to the thermal "noise." This gives rise to an isolated "spike" in the power spectrum (Fig. 19b), the total power of which (i.e., area under the curve) is determined by β, the conversion factor used to convert the QPD response to distance in the linear region of the response (Fig. 12d). This feature is used to directly determine the position calibration, while a Lorentzian fit (as described above) is used to find f_c and γ in order to calculate k (theoretical details of this method are presented in detail in ref. 69). This method is of particular utility because it does not require an AOD or other beam steering device for position calibration and also does not require a separate detection beam. Note that the position calibration is only valid within the linear response range of the QPD. This method also takes somewhat longer than the aforementioned power spectral density analysis, since the x and y spring constants must be determined by separate experiments. Like the simple viscous drag calibration method, this hybrid method can in principle be used to map the trapping potential by using very large amplitude oscillations [69].

Below we give instructions for calibrating via each of the methods discussed, assuming a well-aligned instrument as the starting point. The vast majority of these steps should be automated.

The following steps determine the "height" Z_B of the trapped bead (bead–cover slip separation) and adjust it to the desired position for calibration and experiment, Z_{target}:

1. Set the QPD sampling rate to 3 kHz.
2. Trap a microsphere, and move the cover slip upward using the nanopositioning stage until the bead is clearly in contact (bead will appear white in the image and may also be displaced).
3. Move the nanopositioning stage downward by ~150 nm more than the desired Z_B.

4. Step the nanopositioning stage axially over a large range (at least $5Z_B$ in each direction around the current position) in 1–10-nm steps. At each position, record the average value of the QPD sum signal over 50–200 samples.
5. Plot the averaged sum signal vs. stage position. Fit a line to the data on the left side of the curve (stage positions before the inflection point; *see* Fig. 15b), and a third-degree polynomial to the data on the right side (stage positions after the inflection point; *see* **Note 67**).
6. Find the position (in nm) of the intersection of the fit line and polynomial. This is the nominal position of the bead-surface contact, Z_s. Due to the effective focal shift (Fig. 16b), this must be corrected to find the true $Z_B = \mathrm{EFS} \times Z_s$, where for an oil–water interface, $\mathrm{EFS} \approx 0.82$ [62, 63], i.e., $Z_B \approx 0.82 \times Z_s$.
7. If $Z_B \neq Z_{\mathrm{target}}$, move the stage by $(Z_{\mathrm{target}} - Z_B)/0.82$, and repeat **steps 1**–7 until the height of the bead is within the desired range of Z_{target}.

The following steps calibrate the position detection (Fig. 17):

8. Use the AOD to sweep a trapped bead across the detection beam focus in the x direction, with a range of ±250 nm (or whatever range over which the response signal $X_{V\mathrm{norm}}$ is single-valued) and a step size of 5 nm. At each position, record the average of 100–200 values of $X_{V\mathrm{norm}}$. Repeat for the y direction (Fig. 17, top left inset).
9. Fit a line to the central region of each curve (±~100 nm) and determine the slope (Fig. 17, lower right inset, and Fig. 12d). The inverse of this slope, β, can be used to quickly convert the QPD response signal to physical bead position: $X_{\mathrm{nm}} = \beta_x X_{V\mathrm{norm}}$ (and identically for y). This also serves as a useful check for comparison to β obtained by other calibration methods.
10. For each recorded curve, fit a third-degree polynomial of the form $p(x) = a_0 + a_1 x + a_2 x^2 + a_3 x^3$ (and identically for y) to the entire range. This considerably extends the useable detection range (*important*: *see* **Note 68**). To convert $X_{V\mathrm{norm}}$ to X_{nm}, compute the following:

$$M_1 = (a_0 - X_{V\mathrm{norm}})/(2a_3).$$

$$M_2 = a_2^3/(27a_3^3).$$

$$M_3 = (a_1 a_2)/(6a_3^2).$$

$$M_4 = a_1/(3a_3) - a_2^2/(9a_3^2).$$

$$M_5 = M_1 + M_2 - M_3.$$

$$M_6 = [(M_4^3 + M_5^2)^{1/2} - M_5]^{1/3}.$$

$$X_{\mathrm{nm}} = \mathrm{Re}\{M_4/2\, M_6 - a_2/3a_3 - M_6/2 + (3^{1/2})i/2(M_6 + M_4/M_6)\}.$$

where Re{…} indicates the real part of a complex number and i is the square root of –1.

The following steps calibrate the force via the equipartition method:

11. Set the QPD sampling rate to 65,536 kHz or higher (*see* **Note 69**).
12. Collect data for several seconds. Decimate the data by an appropriate amount so that each point is separated by at least $3\gamma/k$ (*see* **Note 70**).
13. *Optional*: subtract low-frequency drift from the position data (*see* **Note 71**).
14. Convert the raw QPD data into a time series of position data using the calibration procedures above (Fig. 18a). Compute the variance $\langle x^2 \rangle$ of these data in nm^2. *Optional*: plot the data in a histogram (Fig. 18c), fit a Gaussian function in order to determine the standard deviation, and square this quantity to find $\langle x^2 \rangle$. The two answers should agree very closely for a large data set.
15. Calculate $k_x = k_B T / \langle x^2 \rangle$, where $k_B T = 0.013807 \times (T_C + 273.15)$ pN nm; T_C is the magnitude of the temperature in °C. At 25 °C, $k_B T = 4.116$ pN nm.

The following steps describe force calibration by computing the trapping potential:

16. Complete **steps 11–13** above (including the optional part of **step 13**).
17. From the histogram $P(x)$, compute the potential $U(x) = -k_B T \ln(P(x))$, and fit this with the equation $U(x) = \frac{1}{2} k_x x^2 + b$, where b is an arbitrary constant (Fig. 18d). Use the value calculated for k_x via the equipartition method as an initial guess. Repeat for the y direction.
18. *Optional*: create a two-dimensional histogram of positions, and plot the data as an image (Fig. 18b). This image gives a reasonable measure of the symmetry and homogeneity of the trap potential (at least over the narrow region sampled).

The following steps describe force calibration via power spectral density analysis. Analysis steps given for the x direction are identical for the y direction:

19. Complete **steps 11–13** above.
20. Split the time series data into several series of equal length. Compute the one-sided power spectral density $S_{xx}(f)$ (in nm^2/Hz; Fig. 19a) for each series, and average the results to compute the final spectrum (*see* **Note 72**).
21. Use Faxén's law to estimate the drag coefficient, γ, based on the bead-surface separation:

    $R = d/(d + 2Z_B)$,

    $\gamma_0 = 3\pi d\eta$ (*see* **Note 73**),

$(\gamma/\gamma_0) = \gamma_0/[1 - 9/16R + 1/8R^3 - 45/256R^4 - 1/16R^5]$,

$\gamma = \gamma_0 \times (\gamma/\gamma_0)$.

22. *Optional*: estimate γ from the power spectrum itself. Compute $S_{xx}(f)\, f^2$ (in nm² Hz) and fit a flat line to the high-frequency region in which the curve approaches a constant value C_x (Fig. 19c). Then compute $\gamma = k_B T/[C_x \pi^2]$ (note that in Fig. 19c, the curve is calculated in V^2_{norm} Hz, and thus the conversion formula in the legend includes the conversion factor β).
23. Fit the equation $S_{xx}(f) = k_B T/[\pi^2 \gamma (f_c^2 + f^2)]$ to the power spectral density function (Fig 19a). Use the estimate of γ as an initial guess and $f_c = k/2\pi\gamma$ as the guess for f_c, using the value of k determined from the equipartition method (*important*: *see* **Note 74**). We typically fit the region from $f = 50$–100 Hz and above, excluding the region containing low-frequency drift (Fig. 19a).
24. Compute the spring constant $k_x = 2\pi\gamma f_c$. Check that the value for γ is reasonable given Z_B.

The following steps calibrate the trapping force using the "hybrid" method [69] combining viscous drag and power spectral density analysis:

25. With a trapped bead, oscillate the stage with a known amplitude A_{drive} (we use $A_{drive} = 100$ nm) in a sinusoidal pattern at $f_{drive} = 32$ Hz (*see* **Note 75**), with a QPD sampling frequency of 65,536 Hz.
26. Record the QPD response signals X_{Vnorm} and Y_{Vnorm}, and compute (and average) the power spectral density $S_{VxVx}(f)$ for each (in V^2_{norm}/Hz) similarly to **step 20** above (do not block average, as this would alter the height of the spike). Whereas the power spectral density for the axis orthogonal to stage oscillation is essentially unaffected, a clear spike at f_{drive} will be visible in the power spectral density for the axis parallel to the oscillation (Fig. 19b).
27. Estimate γ as done in **steps 21** and **22** above (in this case, C_x will be in V^2_{norm} Hz, and thus $\gamma = k_B T/[C_x (\pi \beta_x)^2]$; β_x can be estimated from previous calibrations).
28. Determine f_c and γ^{Vnorm} via fitting a Lorentzian to the power spectral density, as done in **step 23** (Fig. 19b). If the fitted region includes f_{drive}, remove the data constituting the spike when fitting the curve. Note that the unit of length for γ^{Vnorm} is V_{norm} rather than nanometers.
29. Compute the quantity $W_{th} = A^2_{drive}/[2 (1 + f_c^2/f^2_{drive})]$, the theoretical value of the power in the spike (area under the curve).

30. Compute the quantity $W_{ex} = [S_{VxVx}(f_{drive}) - S^{fit}{}_{VxVx}(f_{drive})]/t_{msr}$, the experimentally determined value for the power in the spike (*see* **Note 76**), where $S_{VxVx}(f_{drive})$ is the value of the computed power spectral density at f_{drive} (i.e., the absolute amplitude of the spike), $S^{fit}{}_{VxVx}(f_{drive})$ is the value of the fit at f_{drive} (i.e., the "thermal background" to which the spike is added), and t_{msr} is the measurement time for the data set from which the power spectral density was computed.
31. Compute $\beta_x = (W_{th}/W_{ex})^{1/2}$ and $\gamma = \gamma^{Vnorm}/\beta_x{}^2$. Check that both values are reasonable based on the alternate calibration methods and previous calibrations.
32. Compute $k_x = 2\pi\gamma f_c$.
33. Repeat the calibration for the *y* direction.

The following procedure uses the viscous drag method to calibrate the trapping force:

34. With a bead in the trap, move the stage at a known velocity v_{stage} over its entire range (±~50 μm). The periods of constant velocity will produce "steps" in the position trace for the bead (Fig. 20b). Move many times in both directions (positive and negative) along the given axis.
35. Repeat **step 34** for a number of different stage velocities, recording the data for each.
36. For each stage velocity, plot the position data in a histogram (Fig. 20c). Remove the central peak and fit a Gaussian (Fig. 20c, inset) to the two remaining peaks to determine their center positions (i.e., bead displacement for the given stage velocity).
37. Plot the bead displacement vs. the stage velocity, and fit a line to the data (the fit should be forced through the origin).
38. Estimate γ based on Z_B (**step 21** above) or one of the other calibration methods.
39. Divide γ by the slope of the line fit in **step 37** to determine k.
40. Observe any major deviations from the linear fit at large displacements. This indicates a nonlinear force–displacement relationship at these positions. Poor overlay of points acquired via sweeping in one direction vs. the other along the given axis may indicate an asymmetrical trapping potential.

The following steps establish the linearity of trap strength with laser power and provide a useful calibration for adjusting trap strength during experiments:

41. For a range of laser powers from ~2 to 60 mW (measured at the back aperture of the objective lens), measure the spring

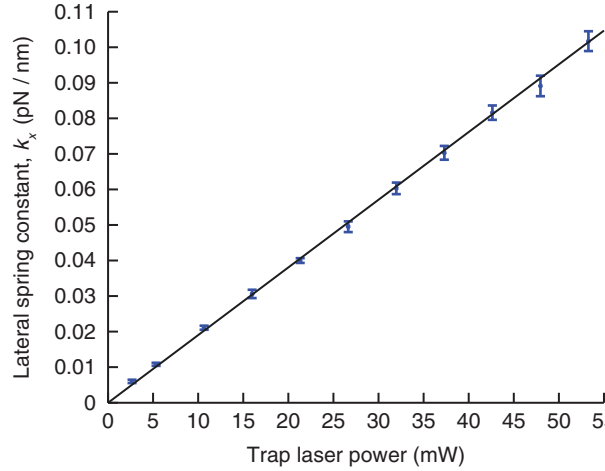

Fig. 21 Linear dependence of lateral trap stiffness (spring constant) on the trapping laser power demonstrated for the *x* dimension. Laser power was measured at the entrance pupil of the objective lens, using a weakly focusing lens to ensure complete collection of the entire beam. Each measurement of the spring constant was obtained as an average between the equipartition and power spectrum analyses. Each point represents the mean of five different measurements taken over several minutes (error bars are ± standard deviation), and the line is a least-squares fit (weighted by the inverse variance of each point) through the origin; slope = $(1.90 \pm 0.02) \times 10^3$ pN nm^{-1} mW^{-1}. Identical analysis for the *y* dimension (not shown) essentially overlaps with the data here, with the fit yielding an identical slope

constant at the bead–cover slip separation typically used for experiments.

42. Plot the spring constant vs. the input laser power, and check that the data are well described by a line (Fig. 21). This graph serves as a useful measure of trap performance and can be used to precisely adjust laser power for the desired spring constant in future experiments.

3.9 Sample Preparation for the Optical Tweezers Assay

The procedure below describes how to prepare a sample for measurement of K560 motion and force generation in the optical trap, starting with a slide chamber with immobilized Cy3-labeled MTs on the surface (*see* Chap. 9 for preparation instructions). Trapping microspheres are incubated with K560, which binds to the antibodies on the microsphere surfaces (Fig. 1). The beads are then introduced to the MT-containing, surface-passivated chamber in the presence of ATP. The slide chamber is then sealed and taken to the instrument. Final assay concentrations are as follows: 1 mM ATP, 10 μM paclitaxel (*see* **Note 77**), 1 mg/mL β-casein, 10 mM DTT, 3 U/mL pyranose oxidase, 90 U/mL catalase, and 22.5 mM glucose.

Prepare the following freshly at the beginning of a set of experiments:

1. "BRB/CS": 96 μL of BRB80 and 4 μL of 25 mg/mL β-casein. Keep on ice.
2. "POC/CS": thaw a POC aliquot freshly and mix 16 μL of β-casein, 2 μL of POC, and 2 μL of BRB80. Keep on ice (*see* **Note 78**).
3. "BRB/Tx": 350 μL of BRB80 and 0.5 μL of 10 mM paclitaxel. Keep at room temperature.
4. Motility mix: 141.5 μL of BRB/Tx, 4.5 μL of 1 M glucose, 2 μL of 100 mM ATP, and 2 μL of 1 M DTT. Keep on ice.
5. Trapping beads: dilute 1 μL trapping bead stock solution in 50 μL BRB80. Mix thoroughly and sonicate in the low-power bath sonicator for 5–10 s (never sonicate the main stock solution). Keep on ice. These trapping beads can be stored at 4 °C for days to months without significant loss of activity.

Do the following for each experiment:

6. Prepare a flow chamber by incubating fluorescence-labeled MTs in a glutaraldehyde-functionalized flow chamber (*see* Chap. 9).
7. During the MT incubation, prepare the K560 and trapping microspheres. Thaw an aliquot of K560 and pre-dilute it in BRB/CS as needed (typically 10,000–50,000×; *see* **Note 79**).
8. Mix 4 μL of pre-diluted motor with 4 μL of trapping beads and incubate for 10 min, so that the MT incubation in the slide chamber and motor-bead incubation end at the same time.
9. About 1 min before the end of the incubations, flush the flow chamber with 40 μL of casein blocking solution (*see* Chap. 9).
10. When the incubations end, add 2 μL of POC/CS to the motor-bead mixture, followed by 30 μL of motility mix. Pipette up and down gently to mix.
11. Immediately flow the entire assay solution into the flow chamber. Dry the ends with a Kimwipe, wiping away from the center of the chamber and taking care not to suck solution out of the chamber itself. Seal the chamber with vacuum grease as described by Nicholas et al. (Chap. 9).

3.10 Optical Tweezers Measurement of Motility and Force Generation

1. Turn on the optical tweezers microscope and follow the protocol in Subheadings 3.7 and 3.8 to align and calibrate it using a test slide.
2. Prepare a sealed sample chamber containing surface-bound MTs and K560 bound to trapping beads according to Subheading 3.9.
3. Mount the slide chamber on the microscope and adjust for Köhler illumination, as done during the alignment procedure.

4. Turn on the 532-nm fluorescence excitation laser, and observe the MTs on the EMCCD. This may require changing focus with the nanopositioning stage. Use the minimal excitation power that still permits visualizing the MTs (use EM gain on the camera).
5. Find an MT oriented perfectly along the *y* axis (use a vertical line drawn on the EMCCD display to check), preferably separated from other MTs by a few micrometers. Move the nanopositioner so that the MT is directly under the cross that marks the trap center on the display. Save the *xy* position of the nanopositioner in the software, and then move to a spot on the cover slip with no MTs. Turn the 532-nm laser and EMCCD imaging off.
6. Follow the steps in the calibration protocol (Subheading 3.8) to obtain a bead in the trap separated from the cover slip surface by ~50–70 nm (*see* **Note 80**), and measure the spring constant. For K560, an appropriate spring constant is approximately 0.05–0.07 pN/nm (adjust if necessary). Record the spring constant and polynomial coefficients determined for the QPD position response. Save the *z* height of the nanopositioner in the software. Set QPD data acquisition rate to 3 kHz and the low-pass filters to 1.5 kHz with 20 dB preamp gain.
7. Move the stage back to the *xy* position saved in **step 5**, keeping the *z* position the same as in **step 6**.
8. Observe the microsphere for 2–3 min as it diffuses in the trap above the MT (*see* **Note 81**). Watch both the *x* and *y* signals and the QPD sum signal (*z* signal) simultaneously. When a motor binds the MT, the fluctuations in all three signals will decrease. Often, the change in the *z* signal will be the most noticeable initially, though K560 moves fast enough in the presence of 1 mM ATP that there is usually no noticeable delay between binding and movement of active motors. If the bead moves, record the data and score it as a motile bead. If the bead does not move, score it as immotile (*see* **Note 79**), and trap a new bead.
9. Move the nanopositioner to a spot on the cover slip with no MTs, and repeat **steps 6–8** for at least ten beads. If the fraction of motile beads is significantly larger than 30 %, repeat the experiment using a higher motor dilution during the sample chamber preparation. This ensures that the motility observed is due to single molecules [71].
10. For each raw data set, convert the QPD responses to bead–trap separations (in nm) using the recorded polynomial coefficients. Next, to obtain the corresponding force data (in pN), multiply the position data by the spring constant ($F = -kx$). Figure 22 presents typical data obtained from this assay for K560.

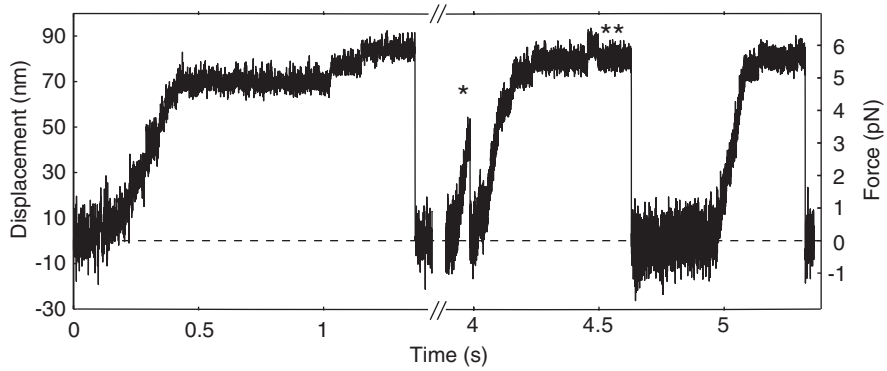

Fig. 22 K560 motility and force generation in the optical tweezers. The force/motion trace shows repeated force generation events in the trap in the *y* direction ($k_y = 0.07$ pN/nm). The motor repeatedly stalls at ~6 pN backward load. As it approaches stalling, the velocity slows considerably, and ~8-nm steps are clearly resolvable. Occasionally, the motor detaches from the MT before stalling (*asterisk*). Although the bead displacement is almost entirely monotonically increasing, the motor occasionally takes backward steps when it stalls (*double asterisk*)

4 Notes

1. The geometrical/ray-optics description offers an intuitive and reasonably accurate description of optical trapping for large particles, for which the microsphere can be considered to be essentially a ball lens that refracts the incident light. However, this model applies poorly to microspheres with diameters d much smaller than the wavelength λ of the trapping beam (note that this regime is defined by the wavelength of the laser *in the sample medium*; for a 1,064-nm laser trapping a particle in aqueous buffer, this corresponds to $\lambda/n_{\text{water}} = 1{,}064\text{ nm}/1.33 = 800$ nm). Electromagnetic scattering theory provides a better description for this case. In this formulation, the small dielectric particle in the trap is considered to be a point dipole (with a dipole moment induced by the electromagnetic field of the trapping beam) that scatters light according to Rayleigh scattering theory. In the electromagnetic field of the trapping beam (due to the intensity gradient imparted by focusing of the beam and its inherent Gaussian intensity profile), this dipole experiences a Lorentz force (called the gradient force) that draws it toward the trap center. This balances the net momentum transfer in the axial direction of the trap that results from Rayleigh scattering (since scattering is isotropic, net momentum is only transferred in the direction of beam propagation, which tends to push the particle out of the trap; this is called the scattering force). The net result is a stable trap in three dimensions (note: due to the scattering force, the position of the trapped bead is slightly shifted beyond the highest intensity of the laser focus).

While refractive models apply well to particles with $d >> \lambda$, and Rayleigh scattering/Lorentz force models describe trapping of particles $d << \lambda$, neither theory applies well to the situation typically encountered in single-molecule optical tweezers studies, in which $d \approx \lambda$ [72]. Over the last several years, a great deal of progress has been made in this area by employing the full Mie solution to Maxwell's equations (also called the Lorenz–Mie, Mie–Debye, or Lorenz–Mie–Debye solution, or Mie scattering), which fully describes the scattering of light by dielectric spheres of any size. This complex theory converges appropriately with the simpler Rayleigh scattering (for very small particles) and geometrical optics (for large particles) descriptions. Nieminen et al. provide an informative review [73] with useful references therein. For any such theory to be of practical use, it must also encompass the effects of nonideal optical aberrations on optical trapping [74], particularly the spherical aberration and astigmatism. Recently, Dutra et al. [75] extended the so-called MDSA (Mie–Debye spherical aberration) theory [76] to include these effects, finding good agreement with experimental results.

2. The kinesin-1 motor domain is N-terminal, so that the truncation in K560 occurs just after the first coiled-coil stalk. The second (truncated) coiled coil is not required for heavy chain dimerization, or to produce motion [42] or force (see, e.g., supplemental information of Gennerich et al. [31]). The polyhistidine (6×His) and GFP tags are on the C-terminus of the construct, immediately following amino acid 560.
3. In the optical trapping field, there continues to be some variability in the surface-coupling techniques used to attach molecular motors to microspheres. Techniques can be categorized broadly according to whether they employ specific vs. nonspecific and covalent vs. non-covalent binding strategies. We advocate the use of specific binding to a known structure on the motor (preferably the tail), if possible, so that there is a high degree of confidence regarding the orientation of the motor on the bead. For K560-GFP, the GFP tag on the tail provides a convenient and specific target for coupling to the bead via high-affinity anti-GFP antibodies. We link the antibodies to beads covalently to ensure strong association and block the remaining surface with covalently bound bovine serum albumin (BSA).
4. Alternatively, PMSF can be substituted by the combination of Pefabloc SC, leupeptin, and pepstatin (Roche), or the cOmplete ULTRA EDTA-free Tablet (Roche), which are less toxic and more effective in long-term protease inhibition.
5. βME is toxic and flammable and should only be opened in a fume hood.

6. Kinesin requires divalent metal cations in order to hydrolyze ATP. Mg^{2+} is the most effective [77]. When preparing the ATP solution, keep it on ice to limit ATP hydrolysis. For assays in which the ATP concentration is non-saturating and needs to be known with precision, the weight of the ATP powder weighed should be corrected for water and residual solvent content (found by examining the certificate of analysis from the supplier).
7. Lysozyme dissolves slowly at 4 °C; hence, it is best to dissolve it at room temperature and then keep the solution on ice. It is preferred to add the imidazole after the lysis by lysozyme, since imidazole inhibits lysozyme activity [78]. Alternatively, other highly specific, active lysozyme can be applied [79].
8. The vial should always be kept on ice, since the tubulin will polymerize at higher temperature.
9. AMP-PNP does not hydrolyze in aqueous solution. However, it becomes unstable at low pH.
10. Microspheres of different diameter can be substituted with only slight modifications to this protocol. It is important that the trapping beads be as perfectly spherical as possible and have a uniform and precise diameter, since irregularly shaped particles or deviations from the expected diameter may lead to errors in trap stiffness determination and prevent the microspheres from tumbling uniformly (therefore preventing certain portions of the surface area from contacting the MTs in the motor trapping assay).
11. EDAC and NHSS are hygroscopic and sensitive to hydrolysis. Avoid any contact of the stocks with moisture or humidity. If the powder forms clumps, it has absorbed water and should be replaced (if in doubt, always replace old stocks with fresh reagents to ensure reactivity). When opening vials, allow them to warm to room temperature in a desiccator beforehand, in order to avoid condensation of moisture from the air.
12. The POC "oxygen scavenging" system is used to eliminate molecular oxygen from solution. The problems caused by molecular oxygen, and our choice of POC to prevent them, warrant discussion. In this assay, the presence of O_2 leads the formation of a variety of reactive species, particularly singlet oxygen ($^1O_2$) and molecular oxygen in the first ($O_2(^1\Delta_g)$) or second ($O_2(^1\Sigma_g^+)$) excited states above the ground state ($O_2(^3\Sigma_g^-)$; *see* ref. 80 for a comprehensive review). These reactive oxygen species rapidly oxidize nearby molecules, leading to protein damage [81, 82] and loss of organic dye fluorescence (simultaneous photobleaching and physical destruction of fluorescently labeled MTs, and prevention of these phenomena by oxygen scavengers [83, 84], provide a dramatic demonstration of both effects). The initial formation of $^1O_2$ generally

occurs as a photochemical reaction in which a "sensitizer" molecule enters an excited triplet state and transfers its energy to $O_2(^3\Sigma_g^-)$, yielding $O_2(^1\Delta_g)$ directly, or $O_2(^1\Sigma_g^+)$, which rapidly converts to $O_2(^1\Delta_g)$ [80] (the $O_2(^3\Sigma_g^-)$ triplet ground state thus quenches the excited triplet state of the sensitizer). In single-molecule experiments, the sensitizer is usually an organic dye excited by a laser, but a vast range of other molecules can participate as well [85], and even polystyrene microspheres in optical trapping beams can act as sensitizers [86].

The typical approach for removing O_2 is to add an oxygen "scavenger" (an enzymatic system that consumes oxygen) while sealing the sample chamber to prevent additional O_2 from entering. The traditional oxygen scavenger system is glucose oxidase/catalase (GOC) in the presence of glucose, for both fluorescence [87–94] and optical trapping assays [31, 53, 95–100]. Glucose oxidase (β-D-glucose:oxygen-1-oxidoreductase, EC 1.1.3.4) [101–103] is a flavoenzyme that catalyzes the oxidation of glucose by O_2, yielding hydrogen peroxide (H_2O_2, which is removed by the catalase) and D-glucono-δ-lactone (which is converted to gluconic acid). The more recent protocatechuic acid (PCA)/protocatechuate-3,4-dioxygenase (PCD) [104, 105] employs a single-step reaction in which PCD catalyzes the cleavage of the PCA extradiol ring, incorporating one O_2 molecule and yielding a muconic acid. This system has several advantages, including that no reactive H_2O_2 is produced. However, both GOC and PCA/PCD produce acid, significantly lowering the pH of the assay solution [43, 90, 106] unless strong buffers are used. With GOC, we observe widespread casein precipitation over long periods (>1 h), correlated with increased acidity and directly attributable to the presence of glucose oxidase (casein itself is acidic and is highly insoluble near its isoelectric point of ~4.6 [107, 108]). This acidification also correlates, over shorter periods, with unwanted and nonspecific sticking of trapping microspheres to glass and cytoskeletal filaments. Swoboda et al. [43] recently introduced the pyranose oxidase/catalase (POC) system [109] to single-molecule fluorescence studies, replacing glucose oxidase with pyranose 2-oxidase (pyranose:oxygen-2-oxidoreductase, EC 1.1.3.10) [110–113], which yields a stable 2-keto-D-glucose that does not convert to an acid (*see* Fig. 7). This system behaves at least as well as PCA/PCD in single-molecule assays, without acidification [43]. We have not rigorously compared the performance of oxygen scavenging by POC vs. GOC in the optical trapping assay, but have observed no negative effects with POC, and qualitatively identical effects on fluorescence. Based on this and the extensive characterization by Swoboda et al. [43], we employ POC in all our current assays.

It should be noted that for relatively high-power trapping beams, photobleaching is likely caused by multiphoton excitation and subsequent dye ionization, rather than $^1O_2$ formation [114]. While elimination of $^1O_2$ is still important (e.g., to prevent damage to K560 motors), photobleaching in this setting is limited by addition of an antioxidant rather than an oxygen scavenger [114]. Antioxidants are also known to inhibit triplet-state-induced fluorophore blinking under anaerobic conditions ($O_2(^3\Sigma_g^-)$ is a triplet quencher, as mentioned above, so its absence enhances population of the fluorophore triplet state). DTT serves this purpose in our assay (in addition to its primary role in preventing unwanted protein disulfide bond formation). Other reducing agents such as βME and tris(2-carboxyethyl)phosphine (TCEP) may also be beneficial, though ascorbic acid and the vitamin E analog Trolox® (6-hydroxy-2,5,7,8-tetramethylchroman-2-carboxylic acid) exhibit superior performance in preventing blinking via triplet quenching [104].

13. Slide chamber ends are sealed to prevent evaporation, ensure an anaerobic environment, and provide physical closure of the chamber (assumed by the theory used for optical trap calibration employing periodic stage oscillation, Fig. 19b, although the theory can be modified for a chamber with open ends [69]). As noted in Nicholas et al. (Chap. 9), vacuum grease is highly preferred over nail polish or other organic solvent-based adhesives. Using these substances to seal the chamber can lead to protein precipitation and nonspecific binding of trapping beads to glass and MTs, even in the absence of attached motors.
14. In principle, back focal plane detection of the microsphere position can be done with the same beam used to do the trapping itself. However, this presents some limitations and challenges. The major limitation is that it is not possible to perform force-clamp (also called force-feedback) experiments in which a constant force is applied by steering the trapping beam in real time to maintain a constant bead–trap separation, since this would prevent detection of bead movement by the attached motor. This technique therefore requires a separate detection beam. In addition, the separate detection beam allows convenient in situ position calibration of the detection system by sweeping the trapped bead across the detection beam using the trap. This allows easy calibration for each trapped bead. If only one beam is available, this sweeping must be done instead via the nanopositioning stage, using a bead stuck to the cover slip. Not only is this more tedious, but the resulting calibration is likely to be less accurate (e.g., due to different proximity of the bead to the cover slip, variations in bead sizes, and imprecision in positioning the stuck bead relative to the

true trap center of the laser beam). This problem can be circumvented using a technique (discussed in the Methods section) that calibrates the detector by analyzing the response to oscillatory movement of the nanopositioning stage [69], but this technique confines the detection to the range in which the detector response is linear. Finally, the high-power lasers typically used for trapping generally have wavelengths >~850 nm. The poor absorption of light of these wavelengths by most silicon photodiodes can cause unwanted low-pass filtering of the position data (called "parasitic filtering") [115, 116] that complicates trap stiffness determination.

15. Although the geometry of the optical trap is radially symmetrical, the linear polarization of the laser introduces an inherent asymmetry that can lead to asymmetry in the trap spring constants [34, 117, 118]. The basis for this effect can be understood fairly simply in the ray-optics regime [119] by considering that the reflection and refraction of light at a dielectric interface (i.e., the Fresnel coefficients at the bead surface) depend on polarization. In practice, the asymmetry can be largely removed by using a quarter wave plate oriented at 45° to the laser polarization to produce circularly polarized light [34], and this effect is also minimized when $d \approx \lambda$ [34, 117]. It is important to understand, however, that it is not entirely straightforward to control the polarization in the focal plane of the objective. First, mechanical stress on any of the optical elements in the pathway can partially orient the otherwise amorphous structure of glass, thereby imparting a slight birefringence (the degree of which is usually spatially inhomogeneous) [120]. This effect, known as photoelasticity or stress birefringence, may be significant in a long pathway containing many lenses and mirrors, due to cumulative effects. Moreover, the dielectric layers on dichroic mirrors can be birefringent, in addition to enhancing or suppressing S vs. P polarization modes depending on the orientation relative to the incident beam [121–123]. Finally, simply focusing light through a high-NA objective can significantly alter the polarization state in the focal plane [122, 124, 125]. These effects can be compensated for in order to achieve the desired polarization in the sample [123, 126]. In practice, we have found that the slight asymmetry in our setup can be removed using the half-wave plate (WP2), by simply applying adjustments, checking the spring constant calibration, and choosing the wave plate orientation at which $k_x = k_y$ within reasonable precision.

16. Because the MTs along which the kinesin walks are attached to the cover slip, the trapping bead is (indirectly) mechanically coupled to the microscope and optical table during experiments. Even miniscule mechanical vibrations will therefore

affect the bead position and produce unwanted noise and artifacts in the trapping data. Therefore, trapping microscopes should be built in the most acoustically and vibrationally isolated environment available. Where possible, all components that generate vibrations (e.g., any equipment with a cooling fan) should be placed in a separate room, with laser beams and electrical signals transmitted via appropriate optical fibers and cables, respectively. In addition, the optical pathway the trapping beam follows should be as mechanically stable as possible, to prevent the trapping beam from drifting (and therefore moving the beam focus/trap center). Optical posts should be thick (we use 1-in.-diameter posts) and of fixed height (not adjustable). We also use an optical breadboard on top of our main table for the majority of our pathway, in order to limit the length of the posts needed to raise the input beams to the height of the microscope's rear port. Temperature fluctuations should also be minimized, since they will cause mechanical elements to expand and contract. Ideally, even the person working with the instrument should be isolated from it during experiments. On our instrument, we have two identical monitor displays and keyboards inside and outside the microscope room, so that after the initial setup, experiments can be conducted from outside.

Air currents within the room should be minimized. In our customized microscope room (approximately ±0.01 °C maximum fluctuations), we use a valance cooling system (essentially a system of chilled-water heat sinks along the perimeter of the room) to control the temperature without the need for air flow. Even in this environment, we have found that small air currents can lead to relatively substantial instabilities in the optical trap position (approximately ±15-nm drift over a few seconds), especially if a person is moving anywhere in the room. This is attributable to (a) beam scattering off any particulate matter moving through the air (i.e., dust) and (b) beam refraction due to air turbulence that causes local, dynamic fluctuations in air density and, therefore, the index of refraction. Both effects reduce the pointing stability of the trapping laser as it travels along the optical pathway leading to the microscope. These problems are minimized by building an acrylic glass (poly(methylmethacrylate), PMMA) airtight enclosure around the optical pathway (this enclosure also adds to thermal stability). In our experience, such an enclosure is absolutely necessary in order to obtain short- and long-term trap stability of better than ~10 nm (even better stability can be attained under these conditions by systematically eliminating sources of mechanical instability in the microscope body, e.g., by replacing the filter turret and objective nosepiece with solid blocks, or even replacing the entire commercial

microscope body completely). A more economical version of this enclosure can be made using a combination of optical posts and air-filled plastic packing material ("bubble wrap") as the walls. Other groups have improved stability further by replacing the atmosphere in the enclosure with helium gas (its index of refraction is very nearly that of vacuum, so that air density fluctuations have smaller effects) [127] or tracking cover slip fluctuations and correcting for them in real time using the nanopositioning stage [128, 129]. Controlling temperature fluctuations of the objective (which are caused in part by the incident laser and are therefore unavoidable) with a feedback control system can also significantly reduce long-term drift of the trap, especially in the axial direction [130].

17. To overcome the scattering force and trap the microsphere in the axial direction requires a tightly focused laser beam and therefore a microscope objective of high NA (this is also a requirement for the objective-based TIRF illumination). To obtain the steepest gradient (tightest focus), the incoming beam must take advantage of the entire NA, i.e., illuminate the entire rear entrance pupil of the lens. Since Gaussian beams have very low intensity toward the edges, it is common practice to "overfill" the objective (expand the input beam to be slightly larger than the entrance pupil). However, it should be noted that the marginal rays in high-NA illumination do not contribute to trapping, due to total internal reflection at the glass–buffer interface (the same phenomenon used for TIRF illumination), and therefore represent wasted energy. This energy (and the wasted energy blocked by the back aperture of the objective) can serve only to produce unwanted heating of the objective and slide chamber. Mahamdeh et al. [35] provide a detailed analysis that concludes that *under-filling* the objective to obtain an effective NA of ~1.25 leads to the most efficient use of laser power (lowest input power to achieve a given spring constant). This should be taken into account when designing the illumination pathway leading to the objective.
18. In principle, a computer-controlled coarse positioning stage is not required. However, most standard stages with manual micrometer-based positioning are highly unstable on the nanometer scale and thus undermine the stability of the entire instrument. We use the M-686.D64 stage because, although it has a very long range of movement that allows exploration of the entire sample chamber, it is highly mechanically stabile when not in motion.
19. To achieve practically useful spring constants requires only ~10–50 mW to enter the microscope objective. However, a much greater laser power is required due to losses in the optical fiber and in diffraction by the AOD. In addition, maximal

power output often decreases over the lifetime of a laser, so that having "reserve" power is desirable. The extra power can also be used to create additional, separately controlled traps.

20. Computer-controlled mirror mounts for beam positioning are more or less required since the optical pathway is enclosed in the isolation box. This also saves a tremendous amount of time during adjustment and allows precise mirror movements that are not possible by hand. It is important that the positioning system be stable when not in motion and also that it allows very small steps in positioning. The Picomotor™ system is ideal because it has excellent resolution and uses a piezo element to turn an adjustment knob that is otherwise stationary when no voltage is applied.
21. Depending on the application, electro-optic deflectors (EODs) may be preferable to AODs given their superior transmittance (which is also essentially independent of beam position), deflection-angle precision [131], and speed. EODs can be substituted for this protocol. Advantages of AODs over EODs are the larger deflection range, ease with which the power of the transmitted beam can be modulated, and the generally cheaper price.
22. High-quality electronic digital filters are expensive. Although they are very convenient, low-pass filtering can also be done in software (i.e., after data acquisition), if necessary. This is done by acquiring data at a sample rate well above the final desired one, low-pass filtering, and then decimating the data to the desired sample rate (no more than twice that of the filter frequency).
23. Particularly for the detection and trapping beams, stable mounting of the fiber output collimator is crucial. The kineMATIX manipulators are particularly convenient because they allow very precise adjustment in combination with highly stable locking of the final position. This also allows the removal of additional mirrors from the pathway that would otherwise be needed to adjust the beam angle and position.
24. The custom polychroic mirror, the spectrum of which is available from Chroma Technologies, will need to be fabricated on request, which can take a few months. For applications not requiring multiple fluorescence channels, a simpler mirror can be substituted. Using a polychroic mirror in the microscope body (PM in Fig. 3) removes the need to switch elements in the microscope filter turret (in fact, the filter turret can be completely removed and the mirror rigidly mounted for added stability). This allows simultaneous trapping and fluorescence imaging and prevents slight misalignments that occur due to the filter turret not returning to precisely the same position each time it is rotated.
25. When purchasing dichroic mirrors, it is crucial to check that the substrate on which the dielectric coating is applied be

designed for use with lasers. Dichroic mirrors for routine fluorescence microscopy have insufficiently flat surfaces for use with coherent laser light and will give rise to interference that significantly degrades the Gaussian beam profiles of reflected lasers. In addition, it is imperative that the dichroic mirrors be mounted with no stress or torque whatsoever on the glass (the resultant bending will also lead to interference effects that ruin the beam profile). This precludes the use of virtually all mechanical means of mounting and even the use of most glues (which contract as they dry). We apply 732 RTV multipurpose silicone sealant (Dow Corning) with a syringe in a small bead along the perimeter of the mirror (*not* on the optical surface, but along the edge). This holds the glass very securely to the mount without deformations, but remains pliable enough to be removed if necessary.

26. The Luca series EMCCDs are not ideal for single-molecule imaging, but are relatively cheap and provide a very wide field of view for MT visualization. For instruments intended for combined trapping and single-molecule imaging, a higher-quality detector will be needed (e.g., the Andor Technology iXon series EMCCD), either in addition to or in place of the Luca EMCCD.
27. We highly recommend custom-writing the software to control the instrument, as this is virtually the only way to integrate control of all components into a single user interface and affords the ability to alter/add capabilities as needed. We have found that this initial investment of time was well worth the enhanced efficiency of a customized program. While LabView offers rapid interface development and contains built-in support for controlling a wide array of cameras and other hardware, we find it to be somewhat cumbersome for data analysis (e.g., trap spring constant calculation) compared to MATLAB. However, the two programs can share data in real time.
28. It is not recommended to refreeze competent cells, which decreases the competent efficiency of the cells. If several transformations are to be performed, prechill several 2-mL microcentrifuge tubes on ice, and divide cells into tubes. 50 μL of cells can be used for several transformations.
29. If time is limited, this step can be omitted. However, expect twofold decrease in efficiency for every 10-min reduction in incubation time (*see* NEB website, http://www.neb.com).
30. Different competent cells require different heat shocking times—adjust accordingly. The 10-s heat shock time here is for BL21(DE3) competent *E. coli* cells from NEB.
31. Check OD_{595} frequently after 2-h growth. After the lag phase, *E. coli* replicates every 20 min, which can easily lead to an overgrown culture.

32. Long kinesin constructs such as K560 tend not to fold properly and form inclusion bodies at 37 °C induction temperature [52]. Stability of the GFP in the K560 construct also decreases dramatically above room temperature [52, 132]. Therefore, an induction temperature <20 °C is recommended for this expression.
33. With the GFP tag, the cell pellet should be bright green. It is recommended to subject the pellet to a cycle of freezing and thawing to assist cell lysis, even if cell harvest and protein purification are performed in the same day [133].
34. ATP, βME, and PMSF should be as fresh as possible, since at pH 7, ATP is prone to hydrolysis, βME can be oxidized and form disulfide bonds in solution when exposed to air, and PMSF has a short half-life (110 min) in water solution at 25 °C [134].
35. The settings given here are appropriate for the Fisher Scientific model F550. Other ultrasonic homogenizers may require different settings to achieve the same results.
36. This is the bulk protein concentration, which overestimates the real concentration of full length K560, since there are fractions of truncated protein and other contaminants. Detailed methods in determining protein concentration are described in [135].
37. 6–12 % DMSO enhances tubulin polymerization [136].
38. Especially after the first K560 purification, it is advisable to perform standard assays for single-molecule function in addition to optical trapping and to rule out protein aggregation, in order to ensure that the motor is "well behaved" and functions as expected. Brouhard [137] provides a very useful approach to quality control for motor proteins in single-molecule studies.
39. The purpose of rinsing the microspheres is to remove surfactants (included to prevent aggregation during storage), soluble polystyrene-carboxyl synthesis byproducts (which could react with cross-linkers), and any other contaminants present in the stock solution. MES activation buffer is used because it does not contain amines or carboxyls that would interfere with the reaction. The slightly acidic pH is chosen to increase the fraction of protonated carboxyl groups (i.e., –COOH rather than $–COO^-$) that will react with EDAC.
40. Quenching of the EDAC reaction is done to eliminate any free cross-linking reagents that could react with protein in subsequent steps. However, since (a) the microspheres are subsequently washed and (b) the reactive intermediates hydrolyze fairly quickly to regenerate the carboxyl groups on the microsphere surface, this quenching step can usually be omitted.

41. Coupling is done in a non-amine-containing buffer and at alkaline pH to promote deprotonation of the primary amines in lysine (i.e., $–NH_2$ rather than $–NH_3^+$; note that the pK_a for this amine is ~10).
42. The amount of total protein (BSA plus antibody) used here is significantly higher than the theoretical amount required to produce a monolayer on the microsphere surface (approximately 0.2 mg). However, we have found that at lower protein concentrations, the microspheres are more likely to aggregate due to multiple microspheres binding the same protein. This is also avoided by adding the beads to the protein, and not vice versa, because it effectively increases the ratio of protein-to-microsphere concentrations. If problems with aggregation occur, possible solutions are (a) to add a small amount of non-ionic surfactant and (b) to use a lower ionic strength coupling buffer (ions can shield the negative charge of the carboxylate ions on the microsphere surface, thereby minimizing ionic repulsion between the microspheres, and allowing attractive hydrophobic forces to dominate). The Bangs Laboratories website (www.bangslabs.com) has extensive technical notes on this subject.
43. The amine-containing quenching solution reacts with any remaining reactive groups on the microsphere surface. Because these groups are short-lived, this incubation can be shortened (or perhaps even skipped).
44. Microspheres retain GFP-binding activity for months when stored at 4 °C (never freeze the microspheres). Store in the smallest available tube to prevent evaporation over time, and wrap the mouth of the tube in Parafilm. When choosing the storage buffer, keep in mind that this buffer will enter the final assay in a roughly 1:20 dilution. For example, if studying enzymatic effects of phosphate in the final assay, PBS may be a poor choice. The protein-coated microspheres are stable over time in a variety of buffers.
45. It is important that the instrument be given sufficient time to equilibrate to a stable configuration. The instrument typically "settles" at a configuration very close to that of its previous use (Fig. 8), so that this "warm-up" period constitutes a type of self-alignment of the instrument. If adjustments are made as soon as the instrument is powered on, the system will continue to drift, thus misaligning the instrument again. The equilibration time will depend on the instrument, and an analysis similar to that shown in Fig. 8 is advisable.
46. Avoid bubbles, which will interfere with bright-field imaging and back focal plane detection. Spread the oil evenly in a thin pool approximately the diameter of the condenser. This helps prevent bubble formation when the condenser contacts the oil.

47. When building the instrument, take care to position all components carefully so that the microscope body and stages are aligned with the optical axis of the illumination pathway. In practice, it is difficult to align the stages with the pathway to better than about 1–2°. Since the stage rotation cannot be finely adjusted, we take the approach of using it as a reference to which the CCD and AOD are then aligned.
48. The most precise way to align the two sets of axes is to track the bead centroid in each image, thereby creating a grid of precise bead positions. Lines can then be fit to various regions of each grid to determine the exact degree of rotation between the two sets of axes. This procedure will also reveal any nonlinearity in the AOD or stage movements.
49. For small angles ($\theta < \sim 0.07$ rad, or ~4°), the approximations $\sin(\theta) \approx \theta$ and $\cos(\theta) \approx 1 - \theta^2/2$ may be used. This reduces computational requirements with essentially no effect on the calculated positions.
50. Use distances of ~2–10 μm, near the center of the field of view. Distances that are too small will be more affected by errors in bead localization, while very large distances that involve placing the bead far off-axis are more susceptible to errors arising from any aberrations in the imaging pathway (e.g., curvature of field).
51. The overall displacement of the bead is highly linear with voltage applied to the AOD, so that simply measuring the distances between pairs of points is theoretically acceptable. However, because AODs exhibit "wiggles" in their position response on the order of a several nanometers [131], fitting a line to the overall data is more reliable.
52. The aberrated "cross" shape of the retroreflected beam pattern on the CCD may be somewhat unexpected (e.g., as opposed to a small circular spot or concentric rings). The pattern arises as a consequence of the laser beam polarization and the combined effects of the high NA of the objective and the lower index of refraction of water than of oil, which lead to total internal reflection of the marginal rays at the glass/water interface. This causes a phase shift of the wave components undergoing total internal reflection, and as a result, the apparent reflection point is displaced, leading to the aberrated reflection pattern. Novotny et al. have analyzed this phenomenon in detail [138]. Note that the orientation of the pattern depends on the angle at which the beam is linearly polarized (and can thus be changed by rotating WP2).
53. The mirror farther from the microscope should be used to adjust the pattern symmetry, since the major effect of this mirror is to move the beam in the back aperture of the objective, thereby changing the angle of the output beam (Fig. 9a),

while tilting the nearer mirror has a greater effect on the angle of the input beam, and therefore the position of the focal spot (Fig. 9b). By using the mirrors in combination, any position/angle can be achieved, even if there are drifts in the overall system over time. On our instrument, we have the four controls for each mirror (up, down, right, left) configured so that adjustments to Pzt-M2 translate the beam in the *opposite* direction of the button pressed (e.g., pressing the down button shifts the beam in the $+y$ direction in the image). Conveniently, this means that the intensity within the pattern shifts in the *same* direction as the button pressed, so that when adjusting the pattern symmetry, one needs only to press the buttons in the direction in which intensity needs to be shifted to make the pattern symmetrical. Pzt-M3, which is used to adjust the focus position, is configured oppositely, so that the beam moves in the same direction as the button pressed. This opposite configuration of the two mirrors is convenient because it means that when aligning the detection beam position/symmetry, the adjustments for both mirrors are always made in the same direction (both for adjustments of using back-reflections and with the QPD signal, later in the protocol).

54. If after repeated attempts to adjust the back-reflection symmetry and position, the trapped bead position is not on the center position marked on the CCD, or the retroreflection from the bead does not appear symmetrical, it is likely that the marked position on the CCD is not truly on the optical axis. In practice, there is a range of positions for which the retroreflected beam pattern can look acceptable, but some will result in trapping at a different position in the x–y plane. If this occurs, experiment with centering the back-reflection at a different position (and readjusting the symmetry) and then trapping a bead and observing its position relative to the new center position. If the alignment is worse, move the back-reflection in the opposite direction. If it is better, move the back-reflection further and repeat. By iterating through this process, a position can be found such that the back-reflection center and trapped bead position coincide in the x–y plane. This position should then be saved as the new reference point for aligning the beam.
55. If the adjustments to Pzt-M1 are too large, the asymmetry will "flip" and the bead will be displaced from the trap center in the opposite direction. If this happens, move in smaller increments in the opposite direction.
56. All switching of filter frequencies and gains should be done automatically via RS-232 communication between the trap software and the low-pass filters. The purpose of this step is to account for offsets caused by the dark current of the photodiode

and/or voltage offsets introduced by other components. In practice, the offsets are different for each setting on the filters and also vary somewhat from day to day (presumably due to temperature changes at the QPD itself, which alter the dark currents). It is important to correct for these offsets mostly because the trap calibrations are not done at the same filter settings as data acquisition. Without subtracting the offsets, the normalized voltages calculated for the same bead displacements may be different during calibration vs. data acquisition, leading to subtle errors in position detection and/or spring constant measurement. Note that preamplifier gain should be used rather than output gain, because the filter adds some very low-voltage artifacts to the high-frequency components of the input signal. If the input signal is preamplified, these artifacts are negligible relative to the true signal, whereas if the amplification occurs at the output, they are not and will hinder power spectrum analysis during calibration.

57. Using the control configurations mentioned in **Note 53** for Pzt-M3, up/down = +/−y and right/left = +/−x.
58. In the optical trapping literature, the QPD response signals are often said to be in units of volts. While this is conceptually useful (e.g., when considering conversion of the QPD signal to nanometers), the x and y QPD signals are in fact normalized by the total QPD voltage and are therefore unitless. As a compromise, we refer to the units of the QPD signal in "normalized volts," V_{norm}.
59. The useful range of the QPD response function can be extended even further, for example, by taking into account the unavoidable crosstalk that occurs between the lateral and axial response functions when the bead is significantly displaced [139], or by limiting the effective NA of the objective for the detection beam [140], in order to create a larger focal spot. In addition, for experiments in which accurate two-dimensional position detection is needed over a wide range, the full two-dimensional detection area can be scanned and fit with a two-dimensional, fifth-degree polynomial [141]. This is generally unnecessary for experiments in which the motion is directed along an MT that is well aligned with one of the microscope axes.
60. Calibration in the axial direction is also possible [26, 60–62, 142, 143], but the QPD sum signal is not normalized, so laser power fluctuations cannot be easily distinguished from axial displacements. In this protocol, measurement of axial position is far less important than that of lateral position, especially since the bead-surface separation is adjusted with fairly good precision at the beginning of each experiment (*see* Fig. 15).

There is generally a trade-off between axial and lateral position detection sensitivity, depending on the effective NA of the condenser lens (adjustable using the aperture diaphragm): higher NA increases lateral position detection sensitivity, with the opposite effect for axial position detection [60, 61]. We generally use the maximum NA (aperture diaphragm fully open), though for very large or small beads, one should be aware that high NA of the detection system can produce unintended effects [61].

61. Assuming the trap behaves as a spring that applies force $F_x = -k_x x$, then the associated potential energy is $U(x) = \int k_x x dx = \frac{1}{2} k_x x^2$. The average value is $\langle U(x) \rangle = \langle \frac{1}{2} k_x x^2 \rangle = \frac{1}{2} k_x \langle x^2 \rangle$, where the brackets ("<…>") denote the average and $\langle x^2 \rangle$ is thus the variance of the distribution of bead positions over time. In classical statistical mechanics, the so-called equipartition theorem states that, for each degree of freedom for which an associated energy has quadratic dependence, the average of that associated energy at equilibrium is $\frac{1}{2} k_B T$ [144]. Thus, $\langle U(x) \rangle = \frac{1}{2} k_x \langle x^2 \rangle = \frac{1}{2} k_B T$, i.e., $k_x = k_B T / \langle x^2 \rangle$. It is worth noting, however, that the more generalized theorem [145] simply states that the energy is equally partitioned between the degrees of freedom. Boltzmann's law gives the probability of a particle having a particular energy/position: $P(x) = \exp(-U(x)/k_B T)/Z_p$, where Z_p is a normalization constant known as the "partition function." Computing $\langle U(x) \rangle = \int P(x) U(x) dx$ gives the associated average energy, which is only $\frac{1}{2} k_B T$ if $U(x)$ is quadratic in x, i.e., if the potential is harmonic. Thus, the equality $k_x = k_B T / \langle x^2 \rangle$ does not apply if the trap potential is not harmonic in the region in question.

62. In the literature, the power spectral density is often referred to simply as the "power spectrum." Although the two are related, they are not precisely the same: the power spectral *density* describes the power *per unit frequency* (units of displacement squared/Hz), while the power spectrum simply measures power (units of displacement squared). This simply amounts to a difference in scaling, but using the power spectrum instead of the power spectral density may lead to errors in the parameters extracted from fits. A good way to tell if the spectrum has been scaled properly is to check that the following is true (Parseval's theorem): the integral of the power spectral density (i.e., total power) should be equal to the variance of the original position data. Both MATLAB (via the function "pwelch") and LabView (via the "FFT Power Spectral Density" virtual instrument) have functions to directly calculate the appropriate quantity, and fast Fourier transform (FFT) functions that can also be used for explicit calculation. In either case, it is the single-sided (frequencies greater than zero) spectrum that

should be calculated, multiplied by 2 in order to maintain the total power in the original spectrum.

63. Note that larger k implies larger f_c. As a result, measurement of spring constants for traps with increasing stiffness requires increasing the bandwidth of the measured spectrum to include higher frequencies. Note also that f_c decreases for larger γ (larger bead size or greater solution viscosity), so that the bandwidth requirements also depend on the experimental conditions. Larger k and γ both decrease the overall amplitude of the power spectral density, though for constant k, the total area under the curve is constant (and equal to the variance in position data; *see* **Note 62**), since decreases in γ (thus reducing the amplitude) are balanced by corresponding increases in f_c (increasing the area under the curve).

64. The obvious approach to the problem of drag dependence on bead-surface distance is to simply move the bead far from the surface during calibration. However, refraction at the glass–water interface (Fig. 16) induces spherical aberration in the beam focus that increases progressively as the beam is focused deeper into the sample, thereby weakening the trap strength. Thus, the spring constant measured with the bead far above the surface is significantly different from that very close to the surface. The calibration must therefore be done at the same axial position as the experiment.

65. The method presented here moves the stage intermittently, but the same principle can be applied for sinusoidal or triangle-wave stage motion; see, e.g., Neuman and Block [26]. Another related method involves observing the response to "instantaneously" stepping the trap [26]. The bead will return to the trap center in an exponentially damped manner with time constant $\tau = \gamma / k$ (i.e., the trap pulls the bead toward the center with force proportional to k and is resisted by a force proportional to γ, which slows it down).

66. In principle, by measuring the bead-surface separation at the extrema of the stage motion, any tilt in the cover slip can be calculated and accounted for in the stage movement (i.e., moving not just in x or y but also in z), thereby maintaining a constant value during the calibration.

67. Determining the precise location of the inflection point can be somewhat arbitrary and can influence the final result of calculations. For the purpose of this protocol, the most important issue is reproducibility of the measurement (i.e., precision rather than accuracy). Since the width of the "peak" in the response signal is very consistent, we use this as our "landmark" when fitting the data. We first find the maximum in the response and fit the polynomial in a fixed region surrounding

it (chosen initially by trial and error in order to get the best fit for the region near the inflection point and then set as a fixed value for future fits). We then fit the line from the beginning of the data set until ~100 nm before the beginning of the region fit by the polynomial.

68. Although the range of position detection can be extended considerably beyond the region in which the QPD response signals are linear (*see* also **Note 59**), it is very important to realize that displacement may not be linear with applied force in regions far from the trap center. On the one hand, the optical trapping "potential energy well" is not infinitely wide, so that at large displacements/high forces, it must "flatten out" and allow the bead to escape. In this region, the spring constant is different from that at the trap center (and will eventually become negative [146–148]). Assuming the same spring constant at these positions will therefore yield a significant overestimate of the applied force. On the other hand, trap stiffness may initially *increase* as the bead is displaced [146–148], so that forces would be underestimated. These effects are generally more significant for beads of large diameter (>1 μm) [147, 148], but should be considered for any size microspheres when working far from the center of the trap. The range in which force is linear with displacement can be determined by mapping the potential of the optical trap, e.g., via the viscous drag force calibration method [146, 148] (Fig. 20d), or by using one strong trap (operating exclusively in its linear range) to calibrate a weaker one by displacing the two traps by known distances [147]. A related method employs the AOD to rapidly switch between two positions, effectively creating two separate traps [149], without the need for two separate beams. If the potential has not been fully mapped at large distances, then the spring constant should be adjusted such that the behavior of interest occurs only within the region in which the restoring force is linear with displacement. For the experiments described here, we avoid working at bead–trap separations >~160 nm, and even smaller separations are generally recommended.

    Interestingly, recent work [147, 150] (see in particular Farré et al. [150] for a detailed theoretical discussion, including extensive background on BFP detection) has demonstrated that while the QPD response signals are linear with position over only a relatively narrow range, they are linear with force over a much broader one. This is essentially a manifestation of the fact that the direction signals measured by the QPD amount to changes in photon momentum and therefore the force exerted on the bead [150, 151]. In principle, this relationship can be used to accurately measure force even at

large displacements and, combined with the aforementioned methods for extending the range of positional detection, could allow the trap to be used over a much wider range.

69. In principle, data collection for equipartition analysis can be done at the same time as that for power spectrum analysis (i.e., the same data set can be use for both methods). We use 65,536 Hz (2^{16} Hz) for the "hybrid" calibration method (because using a sampling rate that is a power of 2 ensures that the spike at $f_{drive} = 32$ Hz falls exactly on a single data point in the resulting spectrum [69]) and therefore use the same sample frequency for all calibration methods. However, if using data that have been low-pass filtered for equipartition analysis (as required for power spectrum analysis), it is very important that the data be sampled at a rate as high as possible (i.e., low-pass filters are set at high frequency). Otherwise, the filters remove a significant amount of power from the signal, thereby reducing the variance and artificially increasing the calculated spring constant. Wong and Halvorsen [152] provide a very detailed analysis of the effects of low-pass filtering/finite detection bandwidth on optical tweezers calibration.

70. $\tau = \gamma/k$ is the characteristic "autocorrelation time" for the trap [153]. At times equal to or shorter than this time scale, bead positions cannot be considered statistically independent (i.e., if the position at one time is known, the position a very short time afterward depends on the initial position and is not random). To obtain an accurate equilibrium measurement of $<x^2>$, data points must therefore be separated by a few τ. The number of data points to discard depends on the trap stiffness (the weaker the trap, the longer the time required between points) and can be predicted based on the input laser power and previous characterization of the expected spring constant (Fig. 21). In practice, discarding correlated values does not have a substantial effect on the computed variance.

71. Low-frequency fluctuations (e.g., due to thermomechanical fluctuations in the optical pathway) can increase the variance of the position data and thereby artificially decrease the calculated spring constant. If these fluctuations can be filtered out, the calculated spring constant will therefore be more accurate. The easiest method for doing this is to take a moving average with a fairly wide window (e.g., 0.2–0.5 s). For a signal without drift, this moving average will be essentially zero, whereas for a signal with slow drift, the resulting average will essentially plot this drift. By subtracting this signal from the original data, the drift can thus be removed. However, this method inevitably leads to inaccuracies (though this may be acceptable if the artifacts introduced are smaller than the original drift). Another method (with essentially the same underlying principle) is to

high-pass filter the data (e.g., at ~2 Hz), although this will likewise remove power from the signal, and some of this power may be due to true thermal motion of the bead. Wong and Halvorsen offer a more robust method (*see* Fig. 4 of ref. [152]), in which the data are high-pass filtered at several different cutoff frequencies, and the results are used to extrapolate the variance at 0 Hz cutoff frequency (i.e., no filter).

72. By the nature of the fast Fourier transform used to compute the power spectral density, the frequency resolution δf is inversely proportional to the measurement time, $\delta f = 1/t_{\mathrm{msr}}$. Therefore, dividing the original data set into more subsets will diminish the frequency resolution, but will simultaneously decrease the amplitude of the noise via averaging. This can also be done by block-averaging the final spectrum [26].

73. For water near room temperature, the viscosity η can be calculated to very good approximation [154], in units of pN s/nm^2, as $\eta = (AT_{\mathrm{r}}^{a} + BT_{\mathrm{r}}^{b} + CT_{\mathrm{r}}^{c} + DT_{\mathrm{r}}^{d}) \times 10^{-12}$, where $T_{\mathrm{r}} = (T_{\mathrm{c}} + 273.15)/300$ (T_c being the magnitude of the temperature in °C), and $A = 280.68$, $B = 511.45$, $C = 61.13$, $D = 45.90 \times 10^{-2}$, $a = -1.9$, $b = -7.7$, $c = -19.6$, and $d = -40.0$. For example, at 25 °C, $\eta = 8.9 \times 10^{-10}$ pN s/nm^2. Since the presence of 1 mg/mL casein contributes only minutely to the solution viscosity [155], we disregard this when making initial estimates.

74. Several experimental issues can lead to a non-Lorentzian power spectral density function in this calibration procedure [156], including aliasing and unintended frequency filtering by the QPD for near-infrared illumination [115, 157] (*see* also **Note 14**) and crosstalk between the QPD response signals. We have taken the approach of experimentally minimizing these artifacts. However, they are well understood theoretically and may be accounted for in the fitting procedure if necessary. Reference [46] provides a free software package to accomplish this. *See* also ref. [158] regarding rigorous parameter estimation from least-squares fitting of power spectra.

75. The motion must be as perfectly sinusoidal as possible (otherwise harmonics—i.e., additional spikes—will appear in the spectrum, and the theory will not be applicable). This precludes, for example, "stepping" the stage by repeated commands from the computer control software. Instead, as smooth a sinusoidal waveform as possible should be sent to the stage with a command to follow the pattern until a stop signal is sent. Wait for a few periods of oscillation before collecting data, so that any initial transients have subsided. The amplitude and frequency of oscillation must be confirmed by recording the stage movement and analyzing it (e.g., via power spectral density analysis of recorded position data) after the

oscillation has completed (rather than just assuming the commanded values). Typically, the actual amplitude is somewhat smaller than the commanded amplitude, and the stage motion lags the commanded movements (i.e., there is a phase lag). The latter is unimportant given the nature of the spectral analysis used to find the spring constant.

76. $[S_{VxVx}(f_{\text{drive}}) - S^{\text{fit}}{}_{VxVx}(f_{\text{drive}})]$ can be interpreted as the height of the spike, while $1/t_{\text{msr}}$, which is related to the separation between neighboring data points in the spectrum, is the width.

77. Many in vitro protocols use a higher paclitaxel concentration. We have found that MTs are stable using the concentrations given here. Paclitaxel is very poorly soluble in water [159] and can form asters and bundles similar in appearance to MTs [160, 161], which we observe often at higher concentrations. These structures can interfere with the optical trapping assay by diffusing into the trap and presumably also deplete the soluble fraction of paclitaxel available for MT binding. After more than ~3 h, paclitaxel-containing solutions should be made fresh from paclitaxel dissolved in DMSO.

78. POC/CS can be stored in the refrigerator at 4 °C overnight if it is not used during one set of experiments. For critical experiments, however, fresh POC should be used.

79. For processive motors such as K560, if 30 % of beads tested in the optical trapping assay exhibit motility, then there is a 95 % chance that any given bead has no more than one motor attached (this probability is derived under the assumption that the number of motors bound to each bead obeys Poissonian statistics) [71]. In fact, given the small likelihood of two motors bound to a microsphere being close enough to engage the MT simultaneously [31, 71, 162], the probability of motion arising from two or more motors under these conditions is well below 1 %. Thus, the condition of 30 % or fewer moving beads is generally regarded as the requirement to attribute observed motility to single molecules. The motor dilution required to achieve this condition varies from one purification to the next and is found by trial and error, starting with an educated guess based on past experience. It should be noted that, especially for a previously uncharacterized motor, it is not valid to assume processivity, and for a nonprocessive motor (by definition), *any* extended motility events must be due to two or more motors simultaneously engaging the MT. To distinguish between these two cases, the motor concentration is varied over several experiments in which the microsphere concentration is kept constant, and the motile fraction of beads is recorded. Plotting the motile fraction P vs. the relative motor-to-bead ratio C, one then attempts to fit the data with one of two Poissonian probability models, $P = 1 - \exp(-\lambda C)$

or $P = 1 - \exp(-\lambda C) - (-)\exp(-\lambda C)$, respectively, where λ is a fitting parameter that can be interpreted as the fraction of motors competent to bind microspheres and contribute to motility. If the data are more consistent with the first model, this suggests that the motor is processive, while if the latter model fits the data more closely, the motor is likely nonprocessive. See, for example, the supplement of ref. [31].

80. The MT has a diameter of 25 nm, whereas the antibody GFP-K560 complex extends a distance of ~20–40 nm from the bead surface [163]. Thus, a ~50–70-nm separation between the cover slip and the bead surface allows the bead to diffuse freely, while allowing interaction between the motor and the MT.
81. During the observation period, the stage z position can be adjusted in small (~10 nm) increments in order to promote binding to the microtubule. Once binding and movement are observed, the stage should be moved slowly back near the original position (the one at which the spring constant was measured).

Acknowledgments

We thank Joshua Shaevitz, Michael Diehl, Erik Schäffer, and Kenneth Jamison for helpful discussions on optical trapping, Marko Swoboda for helpful communications regarding the use of pyranose oxidase in the oxygen scavenging system, and Laura E.K. Nicholas for assistance with photography and figure illustration. The authors are supported by the National Institutes of Health grant R01GM098469. M.P.N. received support from the NIH-funded Medical Scientist Training and Molecular Biophysics Training programs (NIH grants T32GM007288 and T32GM008572, respectively) at the Albert Einstein College of Medicine.

References

1. Verhey KJ, Hammond JW (2009) Traffic control: regulation of kinesin motors. Nat Rev Mol Cell Biol 10:765–777
2. Vallee RB, Williams JC, Varma D et al (2004) Dynein: an ancient motor protein involved in multiple modes of transport. J Neurobiol 58:189–200
3. Johansen KM, Johansen J (2007) Cell and molecular biology of the spindle matrix. Int Rev Cytol 263:155–206
4. Civelekoglu-Scholey G, Scholey JM (2010) Mitotic force generators and chromosome segregation. Cell Mol Life Sci 67: 2231–2250
5. Gaglio T, Saredi A, Bingham JB et al (1996) Opposing motor activities are required for the organization of the mammalian mitotic spindle pole. J Cell Biol 135:399–414
6. Grill SW, Howard J, Schäffer E et al (2003) The distribution of active force generators controls mitotic spindle position. Science 301:518–521
7. Hoffman DB, Pearson CG, Yen TJ et al (2001) Microtubule-dependent changes in assembly of microtubule motor proteins and mitotic spindle checkpoint proteins at PtK1 kinetochores. Mol Biol Cell 12: 1995–2009

8. Winey M, Bloom K (2012) Mitotic spindle form and function. Genetics 190:1197–1224
9. Kiyomitsu T, Cheeseman IM (2012) Chromosome- and spindle-pole-derived signals generate an intrinsic code for spindle position and orientation. Nat Cell Biol 14:311–317
10. Kapitein LC, Peterman EJG, Kwok BH et al (2005) The bipolar mitotic kinesin Eg5 moves on both microtubules that it crosslinks. Nature 435:114–118
11. Ferenz NP, Paul R, Fagerstrom C et al (2009) Dynein antagonizes Eg5 by crosslinking and sliding antiparallel microtubules. Curr Biol 19:1833–1838
12. Florian S, Mayer TU (2012) The functional antagonism between Eg5 and dynein in spindle bipolarization is not compatible with a simple push-pull model. Cell Rep 1:408–416
13. Kapitein LC, Kwok BH, Weinger JS et al (2008) Microtubule cross-linking triggers the directional motility of kinesin-5. J Cell Biol 182:421–428
14. Oladipo A, Cowan A, Rodionov V (2007) Microtubule motor Ncd induces sliding of microtubules in vivo. Mol Biol Cell 18:3601–3606
15. Furuta K, Toyoshima YY (2008) Minus-end-directed motor Ncd exhibits processive movement that is enhanced by microtubule bundling in vitro. Curr Biol 18: 152–157
16. Fink G, Hajdo L, Skowronek K et al (2009) The mitotic kinesin-14 Ncd drives directional microtubule-microtubule sliding. Nat Cell Biol 11:717–723
17. Mountain V, Simerly C, Howard L et al (1999) The kinesin-related protein, HSET, opposes the activity of Eg5 and cross-links microtubules in the mammalian mitotic spindle. J Cell Biol 147:351–366
18. Szczęsna E, Kasprzak AA (2012) The C-terminus of kinesin-14 Ncd is a crucial component of the force generating mechanism. FEBS Lett 586:854–858
19. Wade RH, Kozielski F (2000) Structural links to kinesin directionality and movement. Nat Struct Mol Biol 7:456–460
20. Rogers GC, Rogers SL, Schwimmer TA et al (2004) Two mitotic kinesins cooperate to drive sister chromatid separation during anaphase. Nature 427:364–370
21. Mennella V, Rogers GC, Rogers SL et al (2005) Functionally distinct kinesin-13 family members cooperate to regulate microtubule dynamics during interphase. Nat Cell Biol 7:235–245
22. Moores CA, Milligan RA (2006) Lucky 13-microtubule depolymerisation by kinesin-13 motors. J Cell Sci 119:3905–3913
23. Ross JL, Wallace K, Shuman H et al (2006) Processive bidirectional motion of dynein-dynactin complexes in vitro. Nat Cell Biol 8:562–570
24. Dixit R, Ross JL, Goldman YE et al (2008) Differential regulation of dynein and kinesin motor proteins by tau. Science 319: 1086–1089
25. Hentrich C, Surrey T (2010) Microtubule organization by the antagonistic mitotic motors kinesin-5 and kinesin-14. J Cell Biol 189:465–480
26. Neuman KC, Block SM (2006) Optical trapping. Rev Sci Instrum 75:2787–2809
27. Verdeny I, Farré A, Mas SJ et al (2011) Optical trapping: a review of essential concepts. Opt Pur Apl 44:527–551
28. Svoboda K, Schmidt CF, Schnapp BJ et al (1993) Direct observation of kinesin stepping by optical trapping interferometry. Nature 365:721–727
29. Finer JT, Simmons RM, Spudich JA (1994) Single myosin molecule mechanics: piconewton forces and nanometre steps. Nature 368:113–119
30. Yin H, Wang MD, Svoboda K et al (1995) Transcription against an applied force. Science 270:1653–1657
31. Gennerich A, Carter AP, Reck-Peterson SL et al (2007) Force-induced bidirectional stepping of cytoplasmic dynein. Cell 131: 952–965
32. Mallik R, Carter BC, Lex SA et al (2004) Cytoplasmic dynein functions as a gear in response to load. Nature 427:649–652
33. Simmons RM, Finer JT, Chu S et al (1996) Quantitative measurements of force and displacement using an optical trap. Biophys J 70:1813–1822
34. Rohrbach A (2005) Stiffness of optical traps: quantitative agreement between experiment and electromagnetic theory. Phys Rev Lett 95:168102–168104
35. Mahamdeh M, Pérez Campos C, Schäffer E (2011) Under-filling trapping objectives optimizes the use of the available laser power in optical tweezers. Opt Express 19: 11759–11768
36. Ashkin A, Schütze K, Dziedzic JM et al (1990) Force generation of organelle transport measured in vivo by an infrared laser trap. Nature 348:346–348
37. Soppina V, Rai A, Ramaiya A et al (2009) Tug-of-war between dissimilar teams of

microtubule motors regulates transport and fission of endosomes. Proc Natl Acad Sci U S A 106:19381–19386
38. Gross SP (2003) Application of optical traps in vivo. Methods Enzymol 361:162–174
39. Block SM, Goldstein LS, Schnapp BJ (1990) Bead movement by single kinesin molecules studied with optical tweezers. Nature 348:348–352
40. Piggee C (2009) Optical tweezers: not just for physicists anymore. Anal Chem 81:16–19
41. Vale RD, Reese TS, Sheetz MP (1985) Identification of a novel force-generating protein, kinesin, involved in microtubule-based motility. Cell 42:39–50
42. Case RB, Pierce DW, Hom-Booher N et al (1997) The directional preference of kinesin motors is specified by an element outside of the motor catalytic domain. Cell 90:959–966
43. Swoboda M, Henig J, Cheng H-M et al (2012) Enzymatic oxygen scavenging for photostability without pH Drop in single-molecule experiments. ACS Nano 6:6364–6369
44. Tolić-Nørrelykke IM, Berg-Sørensen K, Flyvbjerg H (2004) MatLab program for precision calibration of optical tweezers. Comput Phys Commun 159:225–240
45. Hansen P, Tolicnorrelykke I, Flyvbjerg H et al (2006) tweezercalib 2.0: faster version of MatLab package for precise calibration of optical tweezers. Comput Phys Commun 174:518–520
46. Hansen P, Tolicnorrelykke I, Flyvbjerg H et al (2006) tweezercalib 2.1: Faster version of MatLab package for precise calibration of optical tweezers. Comput Phys Commun 175:572–573
47. Osterman N (2010) TweezPal – optical tweezers analysis and calibration software. Comput Phys Commun 181:1911–1916
48. Lee WM, Reece PJ, Marchington RF et al (2007) Construction and calibration of an optical trap on a fluorescence optical microscope. Nat Protoc 2:3226–3238
49. Selvin PR, Lougheed T, Hoffman MT et al. (2007) Equipment setup for fluorescence imaging with one-nanometer accuracy (FIONA) Cold Spring Harb Protoc 2007, pdb.ip45
50. Van Mameren J, Wuite GJL, Heller I (2011) Introduction to optical tweezers: background, system designs, and commercial solutions. Methods Mol Biol 783:1–20
51. Bornhorst JA, Falke JJ (2000) Purification of proteins using polyhistidine affinity tags. Methods Enzymol 326:245–254
52. Stock MF, Hackney DD (2001) Expression of kinesin in *Escherichia coli*. Methods Mol Biol 164:43–48
53. Gennerich A, Reck-Peterson SL (2011) Probing the force generation and stepping behavior of cytoplasmic Dynein. Methods Mol Biol 783:63–80
54. Hermanson GT (2008) Bioconjugate techniques, 2nd edn. Academic, New York
55. Abramoff MD, Magalhães PJ, Ram SJ (2004) Image processing with ImageJ. Biophotonics International 11:36–42
56. Schneider CA, Rasband WS, Eliceiri KW (2012) NIH Image to ImageJ: 25 years of image analysis. Nat Methods 9:671–675
57. Visscher K, Gross SP, Block SM (1996) Construction of multiple-beam optical traps with nanometer-resolution position sensing. IEEE J Sel Top Quantum Electron 2: 1066–1076
58. Allersma MW, Gittes F, deCastro MJ et al (1998) Two-dimensional tracking of ncd motility by back focal plane interferometry. Biophys J 74:1074–1085
59. Gittes F, Schmidt CF (1998) Interference model for back-focal-plane displacement detection in optical tweezers. Opt Lett 23:7–9
60. Pralle A, Prummer M, Florin EL et al (1999) Three-dimensional high-resolution particle tracking for optical tweezers by forward scattered light. Microsc Res Tech 44:378–386
61. Rohrbach A, Kress H, Stelzer EHK (2003) Three-dimensional tracking of small spheres in focused laser beams: influence of the detection angular aperture. Opt Lett 28:411–413
62. Neuman KC, Abbondanzieri EA, Block SM (2005) Measurement of the effective focal shift in an optical trap. Opt Lett 30:1318–1320
63. Schäffer E, Nørrelykke SF, Howard J (2007) Surface forces and drag coefficients of microspheres near a plane surface measured with optical tweezers. Langmuir 23: 3654–3665
64. Vermeulen KC, van Mameren J, Stienen GJ et al (2006) Calibrating bead displacements in optical tweezers using acousto-optic deflectors. Rev Sci Instrum 77:013704–013706
65. Florin EL, Pralle A, Stelzer EHK et al (1998) Photonic force microscope calibration by thermal noise analysis. Appl Phys A 66:75–78
66. Gittes F, Schmidt CF (1997) Signals and noise in micromechanical measurements. Methods Cell Biol 55:129–156
67. Svoboda K, Block SM (1994) Biological applications of optical forces. Annu Rev Biophys Biomol Struct 23:247–285
68. Appleyard DC, Vandermeulen KY, Lee H et al (2007) Optical trapping for undergraduates. Am J Phys 75:5

69. Tolić-Nørrelykke SF, Schäffer E, Howard J et al (2006) Calibration of optical tweezers with positional detection in the back focal plane. Rev Sci Instrum 77:103101–103111
70. Guzmán C, Flyvbjerg H, Köszali R et al (2008) In situ viscometry by optical trapping interferometry. Appl Phys Lett 93:184102–184103
71. Svoboda K, Block SM (1994) Force and velocity measured for single kinesin molecules. Cell 77:773–784
72. Wright WH, Sonek GJ, Berns MW (1993) Radiation trapping forces on microspheres with optical tweezers. Appl Phys Lett 63: 715–717
73. Nieminen TA, Knöner G, Heckenberg NR et al (2007) Physics of optical tweezers. Methods Cell Biol 82:207–236
74. Roichman Y, Waldron A, Gardel E et al (2006) Optical traps with geometric aberrations. Appl Opt 45:3425–3429
75. Dutra RS, Viana NB, Maia Neto PA et al (2012) Absolute calibration of optical tweezers including aberrations. Appl Phys Lett 100:131115
76. Viana NB, Rocha MS, Mesquita ON et al (2007) Towards absolute calibration of optical tweezers. Phys Rev E Stat Nonlin Soft Matter Phys 75:021914
77. Böhm K, Steinmetzer P, Daniel A (1997) Kinesin-driven microtubule motility in the presence of alkaline–earth metal ions: indication for a calcium ion-dependent motility. Cell Motil Cytoskeleton 37:226–231
78. Swan IDA (1972) The inhibition of hen egg-white lysozyme by imidazole and indole derivatives. J Mol Biol 65:59–62
79. Grabski AC (2009) Advances in preparation of biological extracts for protein purification. Methods Enzymol 463:285–303
80. Schweitzer C, Schmidt R (2003) Physical mechanisms of generation and deactivation of singlet oxygen. Chem Rev 103: 1685–1758
81. Davies MJ (2004) Reactive species formed on proteins exposed to singlet oxygen. Photochem Photobiol Sci 3:17–25
82. Nilsson R, Merkel PB, Kearns DR (1972) Unambiguous evidence for the participation of singlet oxygen (1δ_) in photodynamic oxidation of amino acids. Photochem Photobiol 16:117–124
83. Vigers GP, Coue M, McIntosh JR (1988) Fluorescent microtubules break up under illumination. J Cell Biol 107:1011–1024
84. Guo H, Xu C, Liu C et al (2006) Mechanism and dynamics of breakage of fluorescent microtubules. Biophys J 90:2093–2098
85. Redmond RW, Gamlin JN (1999) A compilation of singlet oxygen yields from biologically relevant molecules. Photochem Photobiol 70:391–475
86. Landry MP, McCall PM, Qi Z et al (2009) Characterization of photoactivated singlet oxygen damage in single-molecule optical trap experiments. Biophys J 97:2128–2136
87. Yildiz A, Forkey JN, McKinney SA et al (2003) Myosin V walks hand-over-hand: single fluorophore imaging with 1.5-nm localization. Science 300:2061–2065
88. Joo C, McKinney SA, Nakamura M et al (2006) Real-time observation of RecA filament dynamics with single monomer resolution. Cell 126:515–527
89. Blanchard SC, Kim HD, Gonzalez RL et al (2004) tRNA dynamics on the ribosome during translation. Proc Natl Acad Sci U S A 101:12893–12898
90. Dempsey GT, Wang W, Zhuang X (2009) Fluorescence imaging at sub-diffraction-limit resolution with stochastic optical reconstruction microscopy. In: Hinterdorfer P, Oijen A (eds) Handbook of single-molecule biophysics, pp. 95–127. Springer, US
91. Rasnik I, McKinney SA, Ha T (2006) Nonblinking and long-lasting single-molecule fluorescence imaging. Nat Methods 3: 891–893
92. Sambongi Y, Iko Y, Tanabe M et al (1999) Mechanical rotation of the c subunit oligomer in ATP synthase (F0F1): direct observation. Science 286:1722–1724
93. Adachi K, Yasuda R, Noji H et al (2000) Stepping rotation of F1-ATPase visualized through angle-resolved single-fluorophore imaging. Proc Natl Acad Sci U S A 97: 7243–7247
94. Harada Y, Sakurada K, Aoki T et al (1990) Mechanochemical coupling in actomyosin energy transduction studied by in vitro movement assay. J Mol Biol 216:49–68
95. Guydosh NR, Block SM (2009) Direct observation of the binding state of the kinesin head to the microtubule. Nature 461:125–128
96. Spudich JA, Rice SE, Rock RS et al (2011) The optical trapping dumbbell assay for non-processive motors or motors that turn around filaments. Cold Spring Harb Protoc 2011:1372–1374
97. Arai Y, Yasuda R, Akashi K et al (1999) Tying a molecular knot with optical tweezers. Nature 399:446–448
98. Batters C, Veigel C (2011) Using optical tweezers to study the fine details of myosin ATPase mechanochemical cycle. In: Mashanov

GI, Batters C (eds) Single molecule enzymology, pp. 97–109. Humana Press, New York

99. Neuman KC, Chadd EH, Liou GF et al (1999) Characterization of photodamage to *Escherichia coli* in optical traps. Biophys J 77:2856–2863
100. Perkins TT, Li H-W, Dalal RV et al (2004) Forward and reverse motion of single RecBCD molecules on DNA. Biophys J 86: 1640–1648
101. Keilin D, Hartree EF (1948) Properties of glucose oxidase (notatin). Biochem J 42: 221–229
102. Wong CM, Wong KH, Chen XD (2008) Glucose oxidase: natural occurrence, function, properties and industrial applications. Appl Microbiol Biotechnol 78:927–938
103. Bankar SB, Bule MV, Singhal RS et al (2009) Glucose oxidase—an overview. Biotechnol Adv 27:489–501
104. Aitken C, Marshall R, Puglisi J (2007) An oxygen scavenging system for improvement of dye stability in single-molecule fluorescence experiments. Biophys J 94:1826–1835
105. Patil PV, Ballou DP (2000) The use of protocatechuate dioxygenase for maintaining anaerobic conditions in biochemical experiments. Anal Biochem 286:187–192
106. Shi X, Lim J, Ha T (2010) Acidification of the oxygen scavenging system in single-molecule fluorescence studies: in situ sensing with a ratiometric dual-emission probe. Anal Chem 82:6132–6138
107. Eigel WN, Butler JE, Ernstrom CA et al (1984) Nomenclature of proteins of cow's milk: fifth revision. J Dairy Sci 67:1599–1631
108. Hofland GW, van Es M, van der Wielen LAM et al (1999) Isoelectric precipitation of casein using high-pressure CO_2. Ind Eng Chem Res 38:4919–4927
109. Plumeré N, Henig J, Campbell WH (2012) Enzyme-catalyzed O2 removal system for electrochemical analysis under ambient air: application in an amperometric nitrate biosensor. Anal Chem 84:2141–2146
110. Giffhorn F (2000) Fungal pyranose oxidases: occurrence, properties and biotechnical applications in carbohydrate chemistry. Appl Microbiol Biotechnol 54:727–740
111. Pazarlioglu NK, Akkaya A, Tahsinsoy D (2009) Pyranose 2-oxidase (P2O): production from trametes versicolor in stirred tank reactor and its partial characterization. Prep Biochem Biotechnol 39:32–45
112. Artolozaga MJ, Kubátová E, Volc J et al (1997) Pyranose 2-oxidase from *Phanerochaete chrysosporium*– further biochemical characterisation. Appl Microbiol Biotechnol 47:508–514
113. Leitner C, Volc J, Haltrich D (2001) Purification and characterization of pyranose oxidase from the white rot fungus trametes multicolor. Appl Environ Microbiol 67:3636–3644
114. van Dijk MA, Kapitein LC, van Mameren J et al (2004) Combining optical trapping and single-molecule fluorescence spectroscopy: enhanced photobleaching of fluorophores. J Phys Chem B 108:6479–6484
115. Berg-Sørensen K, Oddershede L, Florin E-L et al (2003) Unintended filtering in a typical photodiode detection system for optical tweezers. J Appl Phys 93:3167
116. Peterman EJG, van Dijk MA, Kapitein LC et al (2003) Extending the bandwidth of optical-tweezers interferometry. Rev Sci Instrum 74:3246–3249
117. Madadi E, Samadi A, Cheraghian M et al (2012) Polarization-induced stiffness asymmetry of optical tweezers. Opt Lett 37: 3519–3521
118. Dutra RS, Viana NB, Neto PAM et al (2007) Polarization effects in optical tweezers. J Opt A Pure Appl Opt 9:S221–S227
119. Ashkin A (1992) Forces of a single-beam gradient laser trap on a dielectric sphere in the ray optics regime. Biophys J 61:569–582
120. Hecht E (2001) Optics, 4th edn. Addison-Wesley, Boston
121. Brasselet S, Aït-Belkacem D, Gasecka A et al (2010) Influence of birefringence on polarization resolved nonlinear microscopy and collagen SHG structural imaging. Opt Express 18:14859–14870
122. Schön P, Munhoz F, Gasecka A et al (2008) Polarization distortion effects in polarimetric two-photon microscopy. Opt Express 16:20891–20901
123. Brideau C, Stys PK (2012) Automated control of optical polarization for nonlinear microscopy. Proc SPIE. doi:10.1117/12.908995
124. Axelrod D (1989) Fluorescence polarization microscopy. Methods Cell Biol 30:333–352
125. Axelrod D (1979) Carbocyanine dye orientation in red cell membrane studied by microscopic fluorescence polarization. Biophys J 26:557–573
126. Chou CK, Chen WL, Fwu PT et al (2008) Polarization ellipticity compensation in polarization second-harmonic generation microscopy without specimen rotation. J Biomed Opt 13:014005–014005

127. Abbondanzieri EA, Greenleaf WJ, Shaevitz JW et al (2005) Direct observation of base-pair stepping by RNA polymerase. Nature 438:460–465
128. Carter AR, King GM, Ulrich TA et al (2007) Stabilization of an optical microscope to 0.1 nm in three dimensions. Appl Opt 46:421–427
129. Nugent-Glandorf L, Perkins TT (2004) Measuring 0.1-nm motion in 1 ms in an optical microscope with differential back-focal-plane detection. Opt Lett 29:2611–2613
130. Mahamdeh M, Schäffer E (2009) Optical tweezers with millikelvin precision of temperature-controlled objectives and base-pair resolution. Opt Express 17:17190–17199
131. Valentine MT, Guydosh NR, Gutiérrez-Medina B et al (2008) Precision steering of an optical trap by electro-optic deflection. Opt Lett 33:599–601
132. Tsien RY (1998) The green fluorescent protein. Annu Rev Biochem 67:509–544
133. Johnson BH, Hecht MH (1994) Recombinant proteins can be isolated from *E. coli* cells by repeated cycles of freezing and thawing. Biotech 12:1357–1360
134. James GT (1978) Inactivation of the protease inhibitor phenylmethylsulfonyl fluoride in buffers. Anal Biochem 86:574–579
135. Walker JM (ed) (1996) The protein protocols handbook. Humana Press, Totowa, NJ
136. Robinson J, Engelborghs Y (1982) Tubulin polymerization in dimethyl sulfoxide. J Biol Chem 257:5367–5371
137. Brouhard GJ (2010) Quality control in single-molecule studies of kinesins and microtubule-associated proteins. Methods Cell Biol 97:497–506
138. Novotny L, Grober RD, Karrai K (2001) Reflected image of a strongly focused spot. Opt Lett 26:789–791
139. Perrone S, Volpe G, Petrov D (2008) 10-fold detection range increase in quadrant-photodiode position sensing for photonic force microscope. Rev Sci Instrum 79:106101–106101
140. Martínez IA, Petrov D (2012) Back-focal-plane position detection with extended linear range for photonic force microscopy. Appl Opt 51:5973–5977
141. Lang MJ, Asbury CL, Shaevitz JW et al (2002) An automated two-dimensional optical force clamp for single molecule studies. Biophys J 83:491–501
142. Dreyer JK, Dreyer JK, Berg-Sorensen K, Oddershede L (2004) Improved axial position detection in optical tweezers measurements. Appl Opt 43:1991–1995
143. Deufel C, Wang MD (2006) Detection of forces and displacements along the axial direction in an optical trap. Biophys J 90:657–667
144. Reif F (2008) Fundamentals of statistical and thermal physics. Waveland Press Inc, Long Grove, IL
145. Turner LE (1976) Generalized classical equipartition theorem. Am J Phys 44:104
146. Richardson AC, Reihani SNS, Oddershede LB (2008) Non-harmonic potential of a single beam optical trap. Opt Express 16:15709–15717
147. Jahnel M, Behrndt M, Jannasch A et al (2011) Measuring the complete force field of an optical trap. Opt Lett 36:1260–1262
148. Godazgar T, Shokri R, Reihani SNS (2011) Potential mapping of optical tweezers. Opt Lett 36:3284–3286
149. Martínez IA, Petrov D (2012) Force mapping of an optical trap using an acousto-optical deflector in a time-sharing regime. Appl Opt 51:5522–5526
150. Farré A, Marsà F, Montes-Usategui M (2012) Optimized back-focal-plane interferometry directly measures forces of optically trapped particles. Opt Express 20:12270–12291
151. Smith SB, Cui Y, Bustamante C (2003) Optical-trap force transducer that operates by direct measurement of light momentum. Methods Enzymol 361:134–162
152. Wong WP, Halvorsen K (2006) The effect of integration time on fluctuation measurements: calibrating an optical trap in the presence of motion blur. Opt Express 14: 12517–12531
153. Lukić B, Jeney S, Tischer C et al (2005) Direct observation of nondiffusive motion of a Brownian particle. Phys Rev Lett 95:160601–160604
154. Pátek J, Hrubý J, Klomfar J et al (2009) Reference correlations for thermophysical properties of liquid water at 0.1 MPa. J Phys Chem Ref Data 38:21–29
155. Colas B, Gobin C, Lorient D (1988) Viscosity and voluminosity of caseins chemically modified by reductive alkylation with reducing sugars. J Dairy Res 55:539–546
156. Berg-Sørensen K, Flyvbjerg H (2004) Power spectrum analysis for optical tweezers. Rev Sci Instrum 75:594
157. Berg-Sørensen K, Peterman EJG, Weber T et al (2006) Power spectrum analysis for optical tweezers. II: laser wavelength dependence of parasitic filtering, and how to achieve high bandwidth. Rev Sci Instrum 77:063106

158. Nørrelykke SF, Flyvbjerg H (2010) Power spectrum analysis with least-squares fitting: amplitude bias and its elimination, with application to optical tweezers and atomic force microscope cantilevers. Rev Sci Instrum 81:075103
159. Mathew AE, Mejillano MR, Nath JP et al (1992) Synthesis and evaluation of some water-soluble prodrugs and derivatives of taxol with antitumor activity. J Med Chem 35:145–151
160. Foss M, Wilcox BWL, Alsop GB et al (2008) Taxol crystals can masquerade as stabilized microtubules. PLoS ONE 3:e1476
161. Castro JS, Deymier PA, Trzaskowski B et al (2010) Heterogeneous and homogeneous nucleation of Taxol crystals in aqueous solutions and gels: effect of tubulin proteins. Colloids Surf B Biointerfaces 76:199–206
162. Vershinin M, Carter BC, Razafsky DS et al (2006) Multiple-motor based transport and its regulation by Tau. Proc Natl Acad Sci U S A 104:87–92
163. Kerssemakers J, Howard J, Hess H et al (2006) The distance that kinesin-1 holds its cargo from the microtubule surface measured by fluorescence interference contrast microscopy. Proc Natl Acad Sci U S A 103:15812–15817
164. Humphrey W, Dalke A, Schulten K (1996) VMD: visual molecular dynamics. J Mol Graph 14(33–38):27–28
165. Shaevitz JW (2004) The biophysics of molecular motors: optical trapping studies of kinesin and RNA polymerase. Stanford University, Stanford